2021

Tibial Strains and Tray-Bone Micromotions After Total Knee Arthroplasty: Computational Studies Evaluating the Tibial Fixation

Huizhou Yang
University of Denver

Tibial Strains and Tray-Bone Micromotions After Total Knee Arthroplasty: Computational Studies Evaluating the Tibial Fixation

Abstract

Cemented and cementless fixation in total knee arthroplasty (TKA) have been successfully used for decades. As the number of younger and more active patients treated with TKA continues to increase, long-term implant survivorship is of increasing importance. One of the most common complications and hence the reason for revision is mechanical loosening (23.1% of all revised TKA). The loosening mechanisms have been proposed for different fixation types. For cemented fixation, bone remodeling after surgery is regulated by the changes in strain energy density (SED). The recruitment of osteoclasts and osteoblasts is controlled by SED-related signals. Insufficient stimuli can promote bone resorption, which causes implant loosening. For cementless fixation, the initial fixation of cementless tibial trays is crucial to bony ingrowth onto the porous surface, as the micromotion magnitudes exceeding 150 μm may inhibit bone formations and cause implant loosening. However, the critical parameters influencing SED distributions and tray-bone micromotion are not fully understood. Finite element models have been commonly used to estimate the SED and micromotion, which typically cannot be measured experimentally. However, the challenge that has limited the use of computational modeling in clinical practice is model validation. Any poorly characterized input would directly influence the accuracy of the resulting outputs and cause validation failure. The purpose of this work is to create an experiment to finite element analysis pipeline for investigating the sensitivities of common TKA factors to the tibial SED and tray-bone micromotion. Specifically, the first study developed an experimental-computational validation framework for predicting tibial micromotion and bone deformation. The validated models were utilized for the subsequent application studies. The second study investigated the influence of five common TKA factors on tibial strain energy density. The third study assessed the impact of seven common TKA factors on the tray-bone interface micromotion. Physiological conditions were considered for both bone models and boundary conditions used in each study. Therefore, the conclusions were more clinically meaningful. There were clear recommendations for optimizing the post-operative SED distribution and minimizing the interface micromotion to improve the tibial fixation. The research framework presented in this dissertation could be used as a benchmark for investigating critical parameters influencing implant fixation stability. The computational models presented in this dissertation could be used for pre-clinical assessment and further implant development.

Document Type

Dissertation

Degree Name

Ph.D.

Department

Mechanical Engineering

First Advisor

Paul J. Rullkoetter

Second Advisor

Peter J. Laz

Third Advisor

Chadd Clary

Keywords

Finite element, Implant fixation, Micromotion, Strain energy density, Total knee arthroplasty, Validation

Subject Categories

Biological Engineering | Biomechanical Engineering | Biomechanics | Biomedical Engineering and Bioengineering | Engineering | Kinesiology | Mechanical Engineering

Tibial strains and tray-bone micromotions after total knee arthroplasty: Computational studies evaluating the tibial fixation

_____

A Dissertation

Presented to

the Faculty of the Daniel Felix Ritchie School of Engineering and Computer Science

University of Denver

_____

In Partial Fulfillment

of the Requirements for the Degree

Doctor of Philosophy

_____

by

Huizhou Yang

November 2021

Advisor: Paul J. Rullkoetter

Author: Huizhou Yang
Title: Tibial strains and tray-bone micromotions after total knee arthroplasty: Computational studies evaluating the tibial fixation
Advisor: Paul J. Rullkoetter
Degree Date: November 2021

ABSTRACT

Cemented and cementless fixation in total knee arthroplasty (TKA) have been successfully used for decades. As the number of younger and more active patients treated with TKA continues to increase, long-term implant survivorship is of increasing importance. One of the most common complications and hence the reason for revision is mechanical loosening (23.1% of all revised TKA). The loosening mechanisms have been proposed for different fixation types. For cemented fixation, bone remodeling after surgery is regulated by the changes in strain energy density (SED). The recruitment of osteoclasts and osteoblasts is controlled by SED-related signals. Insufficient stimuli can promote bone resorption, which causes implant loosening. For cementless fixation, the initial fixation of cementless tibial trays is crucial to bony ingrowth onto the porous surface, as the micromotion magnitudes exceeding 150 μm may inhibit bone formations and cause implant loosening. However, the critical parameters influencing SED distributions and tray-bone micromotion are not fully understood. Finite element models have been commonly used to estimate the SED and micromotion, which typically cannot be measured experimentally. However, the challenge that has limited the use of computational modeling in clinical practice is model validation. Any poorly characterized input would directly influence the accuracy of the resulting outputs and cause validation failure. The purpose of this work is to create an experiment to finite element analysis pipeline for investigating the

sensitivities of common TKA factors to the tibial SED and tray-bone micromotion. Specifically, the first study developed an experimental-computational validation framework for predicting tibial micromotion and bone deformation. The validated models were utilized for the subsequent application studies. The second study investigated the influence of five common TKA factors on tibial strain energy density. The third study assessed the impact of seven common TKA factors on the tray-bone interface micromotion. Physiological conditions were considered for both bone models and boundary conditions used in each study. Therefore, the conclusions were more clinically meaningful. There were clear recommendations for optimizing the post-operative SED distribution and minimizing the interface micromotion to improve the tibial fixation. The research framework presented in this dissertation could be used as a benchmark for investigating critical parameters influencing implant fixation stability. The computational models presented in this dissertation could be used for pre-clinical assessment and further implant development.

ACKNOWLEDGEMENTS

I would like to thank a number of people that significantly contributed to my personal growth and accomplishments throughout my Ph.D. First, my most sincere thank goes to my advisor, Dr. Paul Rullkoetter, for his consistent guidance and mentorship. His excellent characters have deeply inspired me. He's demonstrated to me what it means to be a good mentor. It was a great privilege and honor to work under his guidance. Dr. Chadd Clary also needs a special thanks for sharing his knowledge and experience over the years. I would also like to thank Dr. Peter Laz for his enthusiastic support and encouragement. Dr. Kevin Shelburne has also been an important presence. I always appreciated his help when I first came to this Lab.

I also want to thank Dr. Mei Yin for serving as the chair of my defense committee.

I would like to thank my parents for their overwhelming support, without which I cannot fully concentrate on my work without any burden. In particular, I would like to thank my wife, Yan, for always being next to me and supporting my effort.

I would also like to thank DePuy Synthes for their sponsorship of this study.

Finally, I would like to thank some of my colleagues for their help. Especially, I need to thank Alessandro Navacchia and Azhar Ali for teaching me the modeling skills necessary in biomechanics. I also need to thank the post-doctorates, Donald Hume and Casey Myers, for always being there when I needed them. I would also like to thank Yashar Behnam and Mohsen Sharifi Renani for their assistance on the experimental part of my study. In the end, I am grateful to all friends and colleagues for their encouraging words and memorable moment during my time at the DU.

TABLE OF CONTENTS

LIST OF FIGURES

LIST OF TABLES

CHAPTER 1. INTRODUCTION

1.1 Total knee arthroplasty

Total knee arthroplasty (TKA) is a common orthopaedic surgery that replaces the articular knee joint with a man-made artificial joint (Figure 1.1). If the knee is severely damaged by arthritis or injury and nonsurgical treatments are no longer helpful, knee replacement surgery is a safe and effective procedure to relieve pain, correct leg deformity, and resume normal activities (Justine & Ibrahim, 2019). Recently released research showed that there were over 900,000 knee replacements performed in the United States in 2017 (Research, 2018). The future demand in knee arthroplasty is predicted to grow to 1.26 million procedures by 2030 (Sloan et al., 2018). The increasing acceptance of invasive treatment and the observed improvement in function are both expected to contribute to the trend of the greatly increasing implementation of TKA (Kuperman et al., 2016).

Different types of knee replacement systems are designed for patients with individual demands and different knee conditions, each of which has exhibited different advantages and disadvantages. The typical existing knee replacement systems include modular and non-modular, fixed-bearing and rotating-platform, and cruciate-retaining and posterior stabilized (Kurtz, 2009).

The modular total knee replacement system has been the most widely used type (Kurtz, 2009). It includes a femoral component, tibial insert, tibial tray, and a patella component

which may be used when needed. The modularity enables surgeons to select the tibial polyethylene thickness and make intraoperative modifications after final tibial tray placement. It is also easy for implant replacement as removing the tibial insert at the beginning helps improve soft tissue exposure and allows for better visibility (Makhdom & Parvizi, 2017). The drawback of the modular tibial components is the backside wear, the fretting wear that occurs between the interface of the insert and tibial tray (Makhdom & Parvizi, 2017). The cumulative wear debris of ultra-high-molecular-weight polyethylene could lead to osteolysis (Naudie et al., 2007). Non-modular total knee replacement integrates the insert and tibial tray as a single component, which eliminates the backside wear but sacrifices the intraoperative versatility.

The rotating platform knee replacement concept was developed as an alternative to fixed-bearing implants in order to reduce wear and improve range of motion (specifically in internal-external rotation) (Capella et al., 2016). Although studies have shown significantly less wear and improved axial rotation with rotating-platform knees (Berry et al., 2012; White et al., 2015), there are no clinically relevant advantages of rotating platforms with respect to outcomes and survivorship (Cheng et al., 2013; Kim et al., 2010; Moskal & Capps, 2014).

Designs that preserve the posterior cruciate ligament are referred to as cruciate-retaining implants. It offers a series of advantages: less bone sacrifice, better knee joint kinematics and proprioception, increased femoral rollback in flexion, and more excellent implant stabilization (D'Anchise et al., 2013). However, if the posterior cruciate ligament is deficient (especially in older populations), cruciate-retaining knee replacement may cause ligament tearing and increasing laxity. Posterior stabilized implants attempt to

replace the role of the posterior cruciate ligament with an insert post and femoral cam that interact to prevent anterior translation of the femur on the tibia while allowing femoral rollback during flexion (Kolisek et al., 2009). It offers a more stable component interface and increased range of motion (Bercik et al., 2013; Fantozzi et al., 2006; Maruyama et al., 2004).

There also exist some other knee replacement systems, such as hinged knee replacement and partial knee replacement. A hinged joint utilizes a hinge to provide the tibiofemoral flexion-extension motion, which is used for the treatment of global instability or severe bone loss around the knee (Pour et al., 2007). Partial knee replacement replaces only one part of a damaged knee. However, less than 8% of the knee replacement surgeries were partial knees because most patients experience damage to more than one area of the knee (Riddle et al., 2008).

Traditionally, implants are fixed to the bone using polymethylmethacrylate (PMMA), which is commonly known as bone cement. A layer of quick-drying bone cement will be applied between the patient's natural bone and the prosthetic component to bond them together (Figure 1.2). Cemented knee implants have been used for decades, and the effectiveness in the long term was already known (Kim et al., 2014; Meftah et al., 2016). It's a good option for old and less active patients who have a poor-quality bone. For these patients, bone growth may be insufficient to hold the implant in place. However, as the number of younger and more active patients treated with TKA continues to increase (Aggarwal et al., 2014; Aujla & Esler, 2017), implants are required to carry potentially more intensive dynamic activity cycles while maintaining long-term durability (Kim et al., 2016). Recent research has highlighted that cemented knee replacements in younger

patients may not last as long as those in older patients due to the increased activities and demands (Hofmann et al., 2002; Newman et al., 2019). Cementless knee implants, also called press-fit implants, have a rough surface or porous coating that encourages the natural bone to grow into the spaces in the implant, holding it in place without the need for cement (Figure 1.2). Compared with cemented implants, current innovations in cementless tibial trays may offer a more long-lasting biological fixation (Dalury, 2016; Meneghini & Hanssen, 2008). Cementless knee replacement eliminates the worry about potential complications from cement breakdown. However, cementless implants are not suitable for patients who have poor bone quality because strong and healthy bones are needed to hold the implants in place.

Each of the knee replacement systems and fixation types has advantages and disadvantages. The type of the components used depends on the patient's age, physiology, and demands.

1.2 Mechanical loosening

As the number of primary TKA being performed dramatically increased, the projected demand in revisions is expected to grow by 601% by 2030 (Kurtz et al., 2007). Common causes of failure in TKA are infection, mechanical loosening, instability, stiffness, and polyethylene wear (Bozic et al., 2010; Callaghan et al., 2004; Fehring et al., 2001; Gioe et al., 2004; Le et al., 2014; Pitta et al., 2018; Sharkey et al., 2002). The proportion of each cause of TKA failure is constantly changing with the improvement of TKA techniques. Historically, polyethylene wear and its sequelae were among the leading causes for revision TKA. In 2002, Sharkey et al. reported that 25% of revisions were wear-related, with 44%

of late failures attributable to wear (Sharkey et al., 2002). With the development of polyethylene manufacturing (highly cross-linked polyethylene), the ratio of wear-related revisions dropped to 2% for early revisions and 9% for late revisions (Le et al., 2014). However, mechanical loosening continues to remain one of the most common causes of TKA failure in the last decade (account for about 29.8% of the revised cases) (Bozic et al., 2010; Dalury et al., 2013; Hossain et al., 2010; Kasahara et al., 2013; Pitta et al., 2018; Schroer et al., 2013; Sharkey et al., 2014; Thiele et al., 2015).

Mechanical loosening, also referred to as aseptic loosening, is defined as the loosening of a prosthesis from the bone in the absence of infection or trauma (Figure 1.3) (Drees et al., 2007). It was initially considered to be a 'cement disease.' It is now understood that aseptic loosening can occur due to inadequate fixation at the initial surgery, mechanical loss of fixation over time, or biological loss of fixation due to any type of particulate debris (Abu-Amer et al., 2007; Jones & Buckle, 2020). When the prosthesis becomes loose, the patient may experience pain, change in alignment, or instability.

1.2.1 Loosening mechanism

Aseptic loosening is a complex and multifactorial event (Sundfeldt et al., 2006). In the beginning, studies found a correlation between loosening of prostheses and the amount of wear produced from bone cement (Harris et al., 1976; Willert & Semlitsch, 1977). They believed that the fibrous tissue between the bone and cement induced the initial osteolysis. Later, researchers started to find that the polyethylene and metal particles were also responsible for aseptic loosening (August et al., 1986; Dowd et al., 2000; Howie et al., 1988; Malony & Smith, 1995; A. Shanbhag et al., 1994; A. S. Shanbhag et al., 2000). The

mechanism of aseptic loosening induced by wear particles has been concluded. In an aseptic loosening process, the bond of the implant to the bone is destroyed by the body's attempt to digest the wear particles. During this process, normal, healthy bone is also digested (osteolysis), which can weaken or even fracture the bone (Catelas et al., 2011; Ingham & Fisher, 2000). The cellular response to wear debris may vary with size, shape, composition, charge, and concentration of particles (González et al., 1996; Johanson et al., 2012; Sabokbar et al., 2003).

Stress shielding, which refers to the reduction in bone density as a result of removal of typical stress from the bone by an implant, has been considered as another reason causing aseptic loosening (Chong et al., 2011a; Ibrahim et al., 2017; Wikipedia contributors, 2021b; Zhang et al., 2016a). This is because by Wolff's law, that the bone in a healthy person will adapt to the loads under which it is placed (Wolff, 1893). If the loading on a bone increases, the bone will remodel itself over time to become stronger to resist that sort of loading. if the loading on a bone decreases, the bone will become less dense and weaker due to the lack of the stimulus (Frost, 1992; Wikipedia contributors, 2021a). The bone remodeling in response to the external loading is regulated by the changes in strain energy density (SED) (Figure 1.4) (Huiskes et al., 1987; Jang et al., 2008; Ruimerman et al., 2005), which is defined by the scalar-product of stress (σ) and strain (ε) tensors,

$$SED = \int_0^{\varepsilon} \sigma \, d\varepsilon \tag{1}$$

representing the strain energy accumulated per unit volume in an object. The recruitment of bone-resorbing osteoclasts and bone-forming osteoblasts is controlled by the SED-related signals sent through the osteocytic-canalicular network (Burger & Klein-Nulend, 1999). When a prosthesis is implanted into the knee, most of the load will be transferred

through the prosthesis rather than the bone, while the bone areas around the prosthesis will subject to less load and thus produce less strain. The decreased strain signals the osteoclasts to resorb the bone until the strains are normalized, which leads to bone loss over time and eventually causes aseptic loosening.

Comparing with cemented fixation that lacks remodeling capacity, cementless fixations may provide greater longevity through osseointegration and retention of bone remodeling capacity (Behery et al., 2017). However, cemented knee replacements usually have good initial fixations due to the use of bone cement, whereas cementless implants resulted in more frequent early tibial loosening than cemented components (Behery et al., 2017; Berger et al., 2001; Duffy et al., 1998). The initial fixation of cementless knee replacement is crucial to bony ingrowth onto the porous surface of the implants (Bragdon et al., 1996). It takes time for new bone growth, thus not providing immediate fixation. Micromotion magnitude exceeding 150 μm may inhibit bone formations (Engh et al., 1992; Pilliar et al., 1986). Early migration potentially leading to subsequent aseptic loosening has been demonstrated in radio-stereometric analysis studies (Carlsson et al., 2005; Nilsson et al., 2006).

In conclusion, aseptic loosening in TKA results from multifactorial causes. Except for the wear particle factor, bone loss due to bone remodeling after surgery is the main cause of implant loosening for cemented knee replacement. For cementless knee replacement, insufficient bone growth due to the large implant-bone micromotion after the settling period is the primary reason for tibial loosening. Therefore, understanding the critical parameters influencing post-operative SED distribution and implant-bone micromotions is very important to improve tibial fixation.

1.2.2 Challenge in measurements and predictions

Experimentally measuring SED inside the tibia requires advanced hardware and protocols (Grassi & Isaksson, 2015; Shifani et al., 2017). Strain gauges are often considered the gold standard for strain measurements on the bone (Completo et al., 2007; Hillam et al., 2015; Hoshaw et al., 1997; Lanyon et al., 1975; Milgrom, 2000; P. F. Yang et al., 2011). However, this measurement is limited to a few distinct points where gauges are placed. The number of gauges that can be applied over a sample is also limited. Finally, it cannot measure the strain inside the bone. Digital image correlation (DIC) is a non-contact method for bone strain measurements (A. M. Ali et al., 2017; Väänänen et al., 2013). It compares sets of images of the specimen surface under different loading states and calculates the deformations. It allows full-field surface strain measurement with good accuracy. However, DIC investigation is still limited to assessing surface strains (only the cortical bone can be assessed). The internal bone (trabecular bone) deformation cannot be achieved. Digital volume correlation (DVC) is the extension of 2D-DIC to the third spatial dimension, which has been used recently to measure bone strains (Boulanaache et al., 2020; Gillard et al., 2014). It handles sets of micro-CT scans of the specimen to obtain complete 3D strain distributions. However, the obtained data is sensitive to the noise levels in micro-CT scans. Moreover, due to the restriction of the test and measurement device, the tested loadings and motions were very limited.

Similarly, measuring implant-bone interface micromotion is difficult. Previous studies investigated tray-bone micromotion by measuring the relative displacement between the markers placed on the exposed surfaces of the implant and bone (Bhimji & Meneghini, 2012, 2014; Crook et al., 2017; Kraemer et al., 1995). These measurements were limited

to a few distinct points where markers were placed, which may not reflect the actual interface micromotion. Han et al. (2021) measured the full-field tray-bone relative displacements by using a DIC system. However, this still may not represent the actual interface micromotion because the deformation of the cancellous bone underlying the tray was also counted into the change in distance, which would cause underestimations of the tray tilting at the anterior aspect. Full-field interface micromotion can be investigated using the DVC system (Malfroy Camine et al., 2016; Sukjamsri et al., 2015). But same as in measuring bone strains, this measurement is limited to the simple tested loadings and motions. Heilemann et al. (2016) measured the acetabular bone-implant interface micromotion by utilizing a set of pin and sleeve sensors. However, this method destroyed the bone structure and cannot be reproduced in the knee joint due to different anatomy.

Finite element methods have been commonly used to estimate the SED and implant-bone interface micromotion. It addresses all the aforementioned measurement limitations in experimental tests. It allows full-field investigations of bone strains and implant-bone interface micromotions, which typically cannot be measured experimentally. However, the experimental validation of computational models remains challenging. Finite element modeling is limited by the necessary input and assumptions (Sukjamsri et al., 2015). Many input parameters, such as interface contact, bone material properties, and soft tissue mechanical properties, are complex and variable in the modeling. Any poorly characterized input would directly influence the accuracy of the resulting output. The struggle in the validation of computational models restrains the extensive uses of these models in clinical practice.

1.3 Objectives

The overall objective of this dissertation was to create an experiment to finite element analysis pipeline for investigating the sensitivities of common TKA factors to the tibial strain energy density distributions and the tray-bone interface micromotion and assessing the implant stability of TKA designs. Three specific objectives were proposed to accomplish this goal. The first specific objective was to develop an experimental-computational validation framework for predicting the tibial micromotion and bone deformation. The validated models were utilized in the subsequent studies. The second specific objective was to investigate the influence of a variety of factors on tibial SED distributions after cemented TKA. The third specific objective was to investigate the impact of a variety of factors on cementless tray-bone interface micromotions.

1.4 Dissertation overview

Chapter 2 provides an overview of the published literature, which primarily focused on the applications of computational modeling for investigating tibial strains and tray-bone micromotion in TKA. The investigations through traditional experimental methods were also reviewed. The limitations in previous studies and so the opportunities were concluded in the last section of this chapter.

Chapter 3 presents *Validation and sensitivity of model-predicted proximal tibial displacement and tray micromotion in cementless total knee arthroplasty under physiological loading conditions* whose objective was to present a validated experimental-computational framework for predicting tibial micromotion and bone deformation during

activities of daily living. This study has been published in the *Journal of the Mechanical Behavior of Biomedical Materials* (H. Yang et al., 2020).

Chapter 4 presents *Impact of surgical alignment, tray material, PCL condition, and patient anatomy on tibial strains after TKA* whose objective was to investigate the influence of surgical alignment, tray material properties, posterior cruciate ligament (PCL) balance, tray posterior slope, and patient anatomy on proximal tibial strain energy density while considering physiological femoral-insert contact conditions and patellar and PCL ligament forces. This study has been published in *Medical Engineering and Physics* (H. Yang et al., 2021).

Chapter 5 presents *Impact of patient, surgical, and implant design factors on predicted tray-bone interface micromotions in cementless total knee arthroplasty* whose objective was to investigate the influence of surgical (tray alignment, tibial coverage, resection surface preparation), patient (bone properties), and implant design (tray features, surface friction, tibiofemoral kinematics) factors on the tray-bone interface micromotions during a series of activities of daily living. This study has been submitted to the *Journal of Orthopaedic Research*.

Chapter 6 summarizes the contributions of the studies presented in this dissertation and suggests directions for future work in this field.

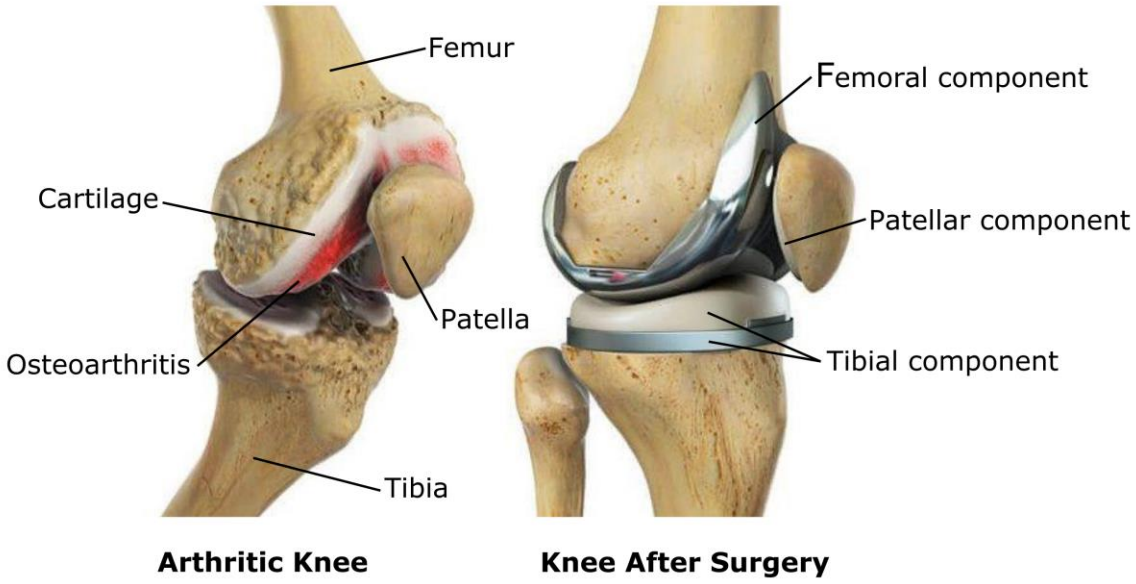

Figure 1.1: Total knee arthroplasty.

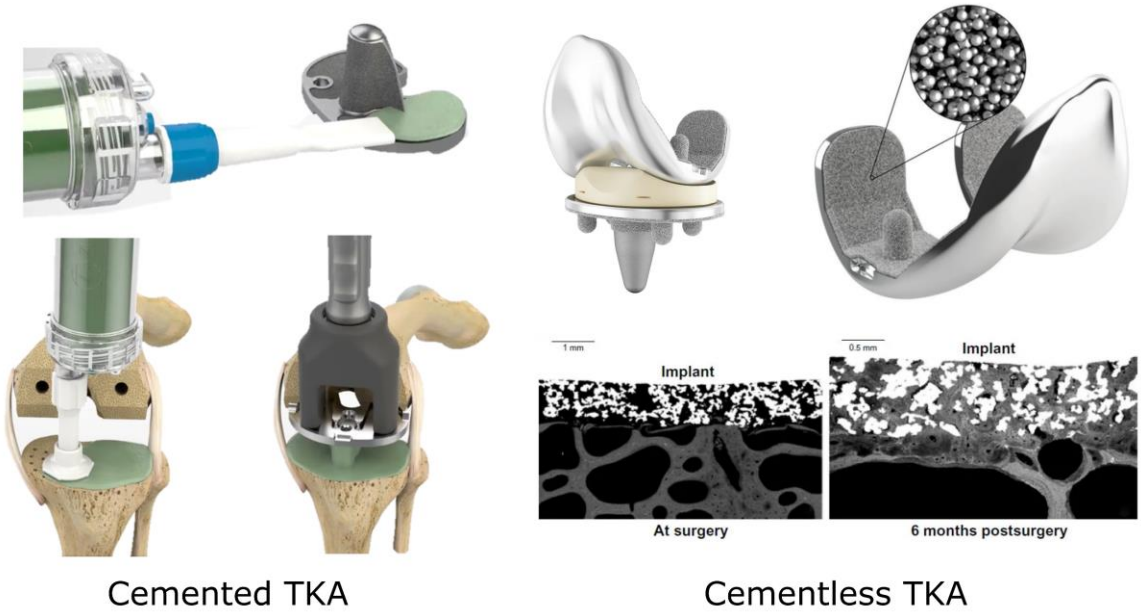

Figure 1.2: Cemented total knee arthroplasty (left); Cementless total knee arthroplasty (right) and bone ingrowth into the porous coating (right-bottom; *porous coating – white; bone – gray; marrow cellular components – black*).

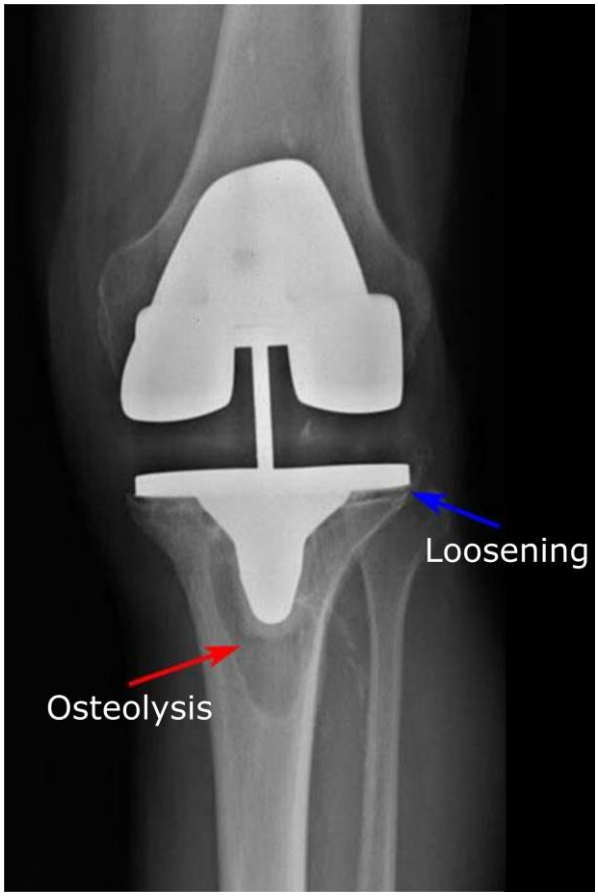

Figure 1.3: Mechanical loosening (aseptic loosening) in TKA. Osteolysis (red arrow) has occurred around the tibial component, causing it to become loosened from the bone (blue arrow).

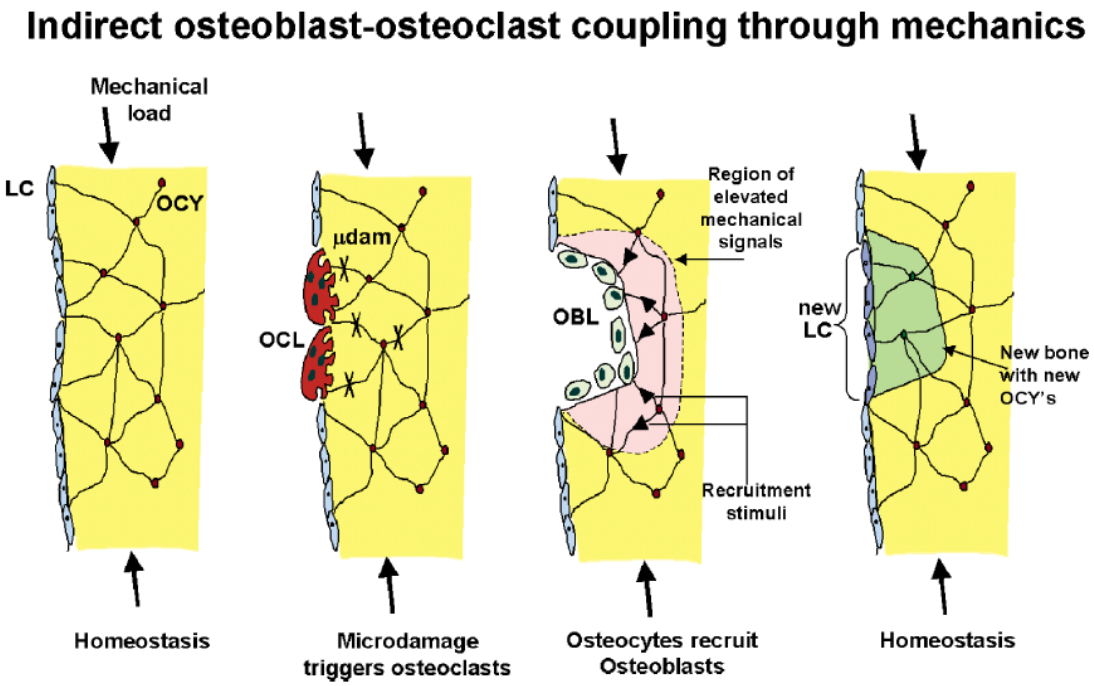

Figure 1.4: The theory described the coupling between formation and resorption as an effect of mechanical stress transfer (*Figure source:* Ruimerman et al., 2005, reprinted with permission).

CHAPTER 2. BACKGROUND AND LITERATURE REVIEW

2.1 Techniques for evaluation of knee biomechanics in TKA

2.1.1 *In-vivo* experimental analysis

In-vivo is Latin for "within the living." It refers to research that is performed with or within an entire living organism. For evaluating the knee biomechanics in TKA, the ideal investigation is to perform experiments on living human subjects to understand the changes in knee joint behavior after implantation. *In-vivo* investigations are typically used to measure knee joint kinematics, bone and soft tissue geometries, body loadings, and knee-related muscle activities by utilizing motion capture devices (fluoroscopy, marker-based camera system), imaging systems (CT - computed tomography, MRI - magnetic resonance), force plates, and electromyography electrodes, respectively. However, *in-vivo* investigations present some limitations that restrain the scope. Many internal variables, such as contact forces, ligament forces, bone strains, and micromotions, cannot be quantified using non-invasive methods in a living subject. Telemetry is an experimental approach that places biocompatible transponders into implants for recording real-time joint loads and moments (Morris et al., 2001; S. Taylor et al., 1998). However, the cost of telemetric implants is expensive, and the device could malfunction after implantation, which only shows moderate success (Komistek et al., 2005). For the research purpose of

this dissertation, telemetric implants cannot measure bone strains and bone-implant micromotions.

2.1.2 *In-vitro* experimental analysis

In-vitro is Latin for "within the glass." It refers to work that's performed outside of a living organism. *In-vitro* investigations use cadaveric specimens to perform tests that are not possible or not allowed during *in-vivo* experiments. Since there is no restriction on invasive experiments, many internal variables that are not accessible *in-vivo* can be measured during *in-vitro* studies (Abrahams, 1967; Markolf et al., 1990). Though informative, extrapolating the results from cadaveric studies back to living beings may be challenging as *in-vivo* conditions are hard to be captured by *in-vitro* testing. For evaluating knee biomechanics in TKA, experimental knee simulators have been developed to reproduce the physiological loading and motion conditions during different daily activities (Colwell et al., 2011; DesJardins et al., 2000; Godest et al., 2000; Halloran et al., 2010; Maletsky & Hillberry, 2005; Varadarajan et al., 2009). These simulators have restrictions in degrees of freedom (DoF) and lack direct measurement of the joint load (Fitzpatrick et al., 2016). An advanced instrument for accurate joint motion simulation is the AMTI VIVO^{TM} simulator (AMTI, Watertown, MA), which provides the closest possible approach to in-vivo conditions (Figure 2.1). The test station is equipped with six servo-hydraulic actuators which can operate in force or motion control in each axis and any combination in all six DoFs. The station also has a six-axis force sensor that can measure the contact forces and moments. Force disturbances caused by actuator nonlinearities or imperfections are corrected by the control system according to the feedback from the force sensor (*VIVO*

Knee Simulator, n.d.). The VIVO also allows users to submit profiles for target joint loadings and kinematics in the Grood and Suntay Coordinate System, a joint system widely adopted in joint biomechanical studies (Grood & Suntay, 1983). Besides, external modules for applying ligament forces, and wear tests using serum are also supported. When simulating knee joint activities, the femoral and tibial components are rigidly fixed to the upper and lower stages of the VIVO machine, respectively. Flexion-extension and varus-valgus rotations or torques can be applied to the upper stage, while the forces and motions along the other four directions can be applied to the lower stage. DIC devices are commonly used together during the tests to measure the target variables. DIC target markers are usually attached to the exposed surfaces of the tray and bone to measure implant-bone migrations. For measuring the bone deformation, a speckled paint is required to be applied to the bone surface.

Cadaveric specimens have been used extensively in *in-vitro* experiments due to their realistic behavior. They provide the bone variability that is encountered in clinical practice (Olson et al., 2012). It is essential to evaluate the performance of a TKA implant in a large population with different bone geometries, qualities, sizes, and material properties. However, this variability can also be bad for some testing. For example, compare the characteristics between two different implants, or investigate the impact of different implant alignments. Cadaveric specimens cannot be repeatedly implanted with different implants or disassembled for realignments. Only testing on several specimens will cause high deviations in the results due to the variability of the cadaveric specimens. Increasing the sample size for a confident evaluation can be costly and time-intensive. For these mechanical testing that focus on the implant, the specimens are desired as generic and

consistent as possible. Synthetic bone, also referred to as artificial bone, is an alternative to the cadaveric bone, commonly used for comparative studies due to its low cost and consistent material properties. They can be made the same with small deviations in mechanical and geometric properties, which addresses the limitation of using cadaveric bones in such testing. However, synthetic bones are limited to their non-realistic properties thus cannot produce clinical outcomes associated with bone anatomy and characteristics.

In general, *in-vitro* studies have an undeniable value for evaluating knee biomechanics in TKA, although associated with the above limitations. However, for the research purpose of this dissertation, the strain inside the bone and the tray-bone interface micromotion still cannot be directly measured *in-vitro*. Experimentally measuring these variables requires advanced devices and protocols (Figure 2.2d) (described in section 1.2.2) (Grassi & Isaksson, 2015; Shifani et al., 2017). However, the loadings and motions that can be applied using such devices are very limited. Computational modeling provides an alternative method for investigating bone strains and tray-bone interface micromotions.

2.1.3 *In-silico* computational analysis

Finite element method has been successfully used for decades in the field of engineering design and scientific research. It has become an effective way to solve complex engineering problems in various areas such as machinery manufacturing, material processing, aerospace, automobiles, civil engineering, and electronic appliances (Keane & Nair, 2005; Paulo Davim, 2012; Pietrzyk et al., 2016; Samui et al., 2016). Finite element analysis replaces complex problems with simple numerical problems. It regards the solution domain as composed of many small interconnected subdomains (called finite

elements), assumes a suitable approximate solution for each element, and then derives the solution to this domain to satisfy the boundary conditions. Finite element method not only has high calculation accuracy but also can adapt to various complex geometries. In the field of biomechanics, because most of the mechanical testing cannot be directly performed *in-vivo*, finite element method has shown its significant superiority and has been widely used. 3D models of human bones, muscles, blood vessels, and other organs can be established realistically and given biomechanical properties by utilizing the powerful modeling function of finite element software and its interface tools. These computational models have been used to solve the mechanical problems of the cardiovascular system, investigate the orthopaedic biomechanics, improve the mechanical performance of medical devices, and optimize the device design (De et al., 2010; Ertan Taskin et al., 2012; Guccione et al., 2010; Kung et al., 2019).

Computational simulations can replicate a specific experiment and the related boundary conditions. Once the model is validated, it can be used as a predictive tool (M. Taylor & Prendergast, 2015). In the field of knee arthroplasty, the experiments during the development and testing of new implants can be extremely expensive and time-consuming due to the requirement of advanced testing devices and a large number of testing samples. Computational modeling provides a very cost-effective platform for the evaluation of design features under different boundary conditions. The objective of computational modeling in knee arthroplasty has been to better understand the post-operative changes in the knee joint (such as mechanics, range of motion, strain distributions, and ligament forces), the interaction between the implant and knee (such as fracture, bone resorption, implant-bone migration, and impingement), and the implant performance (such as wear

and dislocation). Thereby improving TKA techniques to restore knee biomechanics as close as possible to the natural knee, meanwhile, reduce TKA complications. Validated models can be used for quick testing of implant designs without manufacturing physical prototypes as well as for patient-specific pre-operative planning (Abdul-Kadir et al., 2008; Bah et al., 2015; Pettersen et al., 2009; Reggiani et al., 2007). They also provide insight into measurements not easily obtained experimentally (Rullkoetter et al., 2017), such as bone strains, bone-implant micromotions, and contact mechanics.

Another distinct advantage of computational modeling is that it allows repeatable tests on the same model. The same model can be tested under different boundary conditions, meanwhile provides the relative changes of any interested parameters. In the field of TKA evaluation, a tibial model can be virtually implanted with two or more different prostheses and tested under the same loading conditions to compare the performance between different designs. Similarly, the same tibial model can be implanted by using different alignment parameters to investigate the impact on strain distribution in any tibial region. Such kinds of tests cannot be performed by *in-vivo* or *in-vitro* experiments. In addition, the real bone model combines the advantages of artificial bone and natural bone. It can be repeatedly used in comparative studies meanwhile possesses real anatomical structure and biomechanical properties.

Computational models have been extensively used in the field of knee arthroplasty for a range of purposes, such as wear prediction, soft tissue balancing, and stability evaluation, design comparison (Amiri & Wilson, 2012; Ardestani et al., 2015, 2019; Pal et al., 2008). However, the outcomes from computational simulations are not yet widely accepted and trusted in clinical practice. The most fundamental reason is the lack of experimental

validation. Indeed, the comparative studies using computational models could be helpful in filtering out better design features at the early implant design phase. However, whether the design outcomes meet the clinical criteria is unreliable and unconvincing in the absence of experimental verification. The second reason is the lack of realistic representations during the validation procedure. For example, a validated knee model using synthetic bone can only be used for very limited research in clinical settings due to the absence of realistic bone properties. Similarly, validating models under simple loading conditions is insufficient to provide comprehensive clinical suggestions due to the lack of physiological loading representations. Therefore, computational modeling will not be trusted in clinical practice unless a thorough validation of models under physiological conditions is performed. Validating computational models involving human tissues is challenging. Any poorly characterized input would directly influence the accuracy of the resulting outputs and cause validation failure.

This chapter will review the previous works investigating bone strains and tray-bone micromotions in TKA, mainly focusing on the applications of computational modeling though model validations are mostly lacking. Experimental investigations will also be reviewed.

2.2 Investigation of bone strains in TKA

2.2.1 Experimental investigations

Bone remodeling after total knee arthroplasty is regulated by the changes in strain energy density (Huiskes et al., 1987; Jang et al., 2008; Ruimerman et al., 2005). Experimentally measuring bone strains *in-vivo* is best ideal for understanding how TKA

factors influence the bone strain distributions. However, the existing techniques cannot quantify bone strains inside the human body by non-invasive methods. Although bone strains are unquantifiable *in-vivo*, researchers could measure bone loss to infer and compare the impact of each factor on bone remodeling. The typical way to quantify bone loss is to establish a baseline bone mineral density based on the CT scans taken immediately after surgery. Then compare with the follow-up CT scans conducted several years later to calculate the bone loss. Munro et al. followed 46 patients (54 knees) receiving either fixed-bearing or rotating-platform TKA. Obvious bone density loss (up to 12.6% for cancellous bone and 3.6% for cortical bone) was found in proximal tibial regions, but no differences in bone loss between these two cohorts (Munro et al., 2010). The result suggests that the strain distributions in the tibiae are very close between these implant designs. Soininvaara et al. (2004) investigated the femoral bone loss after TKA using the same method. *In-vivo* investigation of bone loss provides the most meaningful outcomes in clinical practice due to the real biomechanical environment but also presents some drawbacks. Firstly, collecting data is extremely time-consuming as it usually takes several years to follow up with the patients. Secondly, because many individual factors could contribute to bone loss and cannot be isolated, a large number of patients is required to obtain confident comparative results. Additionally, the application of this *in-vivo* investigation is limited in the implant design phase because the initial designs cannot be used in clinical without the approval from Food and Drug Administration (FDA).

Since the mechanism of the bone remodeling after TKA was already known, sufficient stimuli will promote bone growth, and insufficient strains will cause bone resorption. Therefore, bone remodeling patterns could be directly derived by comparing the bone

strains. *In-vitro* experiments allow direct measurement of bone surface strains, which are thus utilized to study the impact of different factors on bone strains. Synthetic bones were usually preferred by the researchers to perform comparative studies due to their consistent shape and properties, so as to isolate the impact of bone anatomy on bone strains. During the experiment, synthetic bones will be implanted with different prostheses and alignment parameters according to the study objectives. The implanted bones and an intact bone (as the baseline reference) will then be loaded via experimental devices to simulate *in-vivo* loading conditions. The surface bone strains will be measured and compared to estimate the potential bone remodeling pattern. There are many methods to measure the surface bone strains: (1) Strain gauge, an electrical sensor that allows strain measurement along all three axes. But the measurement is limited to a few distinct where gauges are placed (Figure 2.2a). (2) DIC system, an optical method that could measure the strain on the entire bone surface placed (Figure 2.2b). (3) Photoelastic coating analysis is another optical method that could visualize the strain very smoothly placed (Figure 2.2c). Briefly, this method bonds a photoelastic coating to the bone and measures the coating by a reflection polariscope. Changes in the index of refraction of the coating material create color bands when viewed under polarized light. The isochromatic fringe patterns are relative to the underlying strains and readily quantifiable (Glisson et al., 2000). Studies using synthetic bones and these measurement techniques have been performed to investigate the impact of stem features, implant malalignments, resection levels, cementation methods, implant materials, and implant types on the surface bone strains (Berend et al., 2010; Cawley et al., 2012; Completo et al., 2008a, 2008b, 2010; Rankin et al., 2016; Small et al., 2010). Instead of using synthetic bone, Green et al. performed a similar study using cadaveric tibiae to

compare the impacts of neutral and varus alignment on bone strains (Green et al., 2002), which is one more step closer to *in-vivo* conditions. But as discussed previously, experiments involving real bones require more specimens to draw confident results due to the individual differences.

In-vitro experiments address the limitations of *in-vivo* investigations. *In-vitro* methods enable a quick estimation of the potential bone remodeling pattern by comparing the strain changes without the need for years follow-ups. They also allow testing on design prototypes that have not been approved by FDA. Testing using synthetic bones can standardize boundary conditions and evaluate the effect of the implant alone. However, *in-vitro* investigations on bone strains are not without limitations. The first is the lack of a biomechanical environment. The tested loading in previous studies was simple compressive loads simulating body weight or single activity without considering additional soft tissue loading on the target bone. Another limitation is the inability to measure the strains inside the bone (cancellous bone strains). Even for the cortical bone, the measurements were only limited to the surface layer. Using only surface strain variations to represent the overall strain differences lacks experimental evidence. These limitations may explain why the *in-vivo* study reported no difference in bone loss between fixed-bearing and rotating-platform designs, while an *in-vitro* study speculated that rotating-platform designs would cause more bone loss due to the lower cortical strains measured on the bone surface (Malinzak et al., 2014; Munro et al., 2010). Scott et al. used acoustic emission to evaluate the internal bone strains (Scott et al., 2013). Acoustic emission is a technique for measuring structural damage. The damage of the bone structure in response to stress creates elastic sound waves, which can be detected at the surface by piezoelectric

sensors. However, acoustic emission only provided an overall comparison which cannot be localized into specific regions. Srinivasan et al. measured the cancellous bone strains by loading a small piece of cancellous (Srinivasan et al., 2016). This method lacks biomechanical characteristics and can only be used for very limited research purposes.

2.2.2 Computational predictions

Finite element models have been commonly used to predict the bone strain parameters, even though accurate results may not be obtained due to the lack of biological data to feed models (Figure 2.4) (Prendergast, 1997). Computational simulations enable investigations of the bone strain at the regions which cannot be accessed experimentally, such as the implant-bone interface and the region under the stem. These predictions provide a more comprehensive understanding of the impact of TKA factors on bone remodeling.

Because the shape and material properties of the synthetic bone are known, the synthetic bone model is straightforward to model with high accuracy. Many computational studies used synthetic bone models to further their studies that cannot be performed *in-vitro* (Au et al., 2007; Completo et al., 2008c, 2009; Innocenti et al., 2009). Researchers simulated their *in-vitro* experiments by virtually implanting the prosthesis into the synthetic bone model and applying the same loads used in the experimental tests. Completo et al. (2007) experimentally loaded an implanted synthetic bone and validated their computational model by comparing measured and predicted surface bone strains. The model was subsequently utilized to investigate the bone strains near the stem-bone interface, and the effects of different stem types and lengths on the stress shielding were compared (Completo et al., 2008c, 2009). Similar methods were used to study the impact

of implant material properties and implant medial-lateral positionings (Au et al., 2007; de Ruiter et al., 2021; Innocenti et al., 2009).

While synthetic bone models are preferred for easy modeling and accuracy, human bones have natural and heterogeneous material property distributions. Simulations using real bone models can provide more physiological investigations on bone strains. Modeling the human bone is relatively complicated. First, the bone geometry needs to be segmented from CT scans. Then assign each meshed bone element the material properties (density, elastic modulus, Poisson's ratio) according to the Hounsfield Unit (HU). The bone mineral density is related to the HU thus can be obtained directly from the known relationship. Experimentally measured density-elasticity relationships are used for calculating the elastic modulus for individual elements. Because CT scans may have errors due to the scanning environment, bone mineral density phantom can be used to calibrate the HU-density relationship. The established real bone model can be implanted and repeatedly tested with different prostheses and alignment parameters, which cannot be performed experimentally. Studies using real bone models have been conducted to investigate the impact of implant materials, stem lengths, cementation types, and implantation parameters on bone remodeling (Chong et al., 2011b; Eidel et al., 2020; Jia et al., 2017; Zhang et al., 2016b). Due to the large variations of human bone in terms of shape, size, and density, the outcomes from the simulations using a single real bone model may not be representative in a large population. Anjis et al. (2020) investigated the population-based effect of TKA alignment on simulated tibial bone remodeling. In the study, 47 real bone models were assessed. The result indicated that the mechanical alignment induced more bone loss in the medial-proximal region. However, the bone loss has large differences between individuals,

ranges from 15~30% in the medial region for mechanical alignment. These observed differences were mainly due to the difference in bone density distributions, which illustrate the benefit of population-based computational analyses over single model studies.

Some of the studies used simple axial compressive loads for the simulated loading conditions, which were divided into medial and lateral portions according to specific ratios and uniformly applied on the insert surfaces to simulate standing or other activities (Completo et al., 2007; Eidel et al., 2020; Innocenti et al., 2009). Perillo-Marcone and Tylor (2006) showed that the stresses generated at the implant-bone interface were dependent on the kinematics of the joint (such as contact location), which are affected by the TKA design, surgical alignment, and the balance of the soft tissue. Many later studies started considering the femoral-insert contact conditions (such as contact locations and directions) (Anijs et al., 2020; Chong et al., 2011b; Nakamura et al., 2017; Simpson et al., 2009). Nakamura et al. (2017) derived physiological loading conditions by utilizing a validated dynamic musculoskeletal model and applied it to the bone strain analysis model to investigate the impact of surgical alignments on bone remodeling. Duda et al. (1998) unveiled a large influence of the muscle loading on the strain distributions, which led to some subsequent studies starting to consider soft tissue forces. A recent computational study considered almost all relevant soft tissue forces when investigating the impact of implant materials on tibial stress shielding (Au et al., 2007). These soft tissues included the cruciate ligament, medial collateral ligament, semimembranosus, semitendinosus, patellar tendon, and other minor soft tissues. However, most of these soft tissue forces were less than 10N and thus negligible. Concluding the existing literature, the primary soft tissues that affect the bone

strain distributions after TKA are the patellar tendon, the semimembranosus, and the cruciate ligament (only suitable when retained).

Computational simulations were also utilized to directly predict bone remodeling patterns using the strain-parameter-related remodeling equations (Anijs et al., 2020; Cawley et al., 2012; Chong et al., 2011b; Jia et al., 2017; Quilez et al., 2017). Different mechanical variables are used to define the reference stimulus, such as effective stress (Beaupré et al., 1990; Doblaré & García, 2002), strain (Fernandes et al., 1999; Frost, 1990), or strain energy density (Huiskes et al., 1987; Kaczmarczyk & Pearce, 2011). During these simulations, the implanted bone models were loaded with physiological loads, and the related strain parameters were predicted for each bone element. Bone remodeling thresholds were set according to different remodeling equations. When the predicted bone strain parameter was out of the critical range, the bone density of the corresponding element would be adjusted accordingly based on how much the strain parameter was out of the range. After the density of all elements were adjusted, the second simulation would be performed on this updated bone model under the same loading conditions. The iteration process was repeated until the pre-defined timeline was reached (e.g., two years) or the strain parameters of all elements were within the critical range (no density change). The bone loss was then quantified by comparing the bone density of the initial and final bone models. Comparing with the computational simulations that output the bone strain differences, these bone remodeling predictions may be more preferred by surgeons and implant developers because the quantified bone loss provides a direct evaluation of the risk of potential aseptic loosening. However, these predictions are hard to be validated. Different remodeling equations (with different coefficients, reference stimuli, and

remodeling thresholds) could result in distinct predictions. Thus, which outcome is more reliable is unknown. It has been demonstrated that the stress does not have a strong meaning correlated to bone density (Linde et al., 1990). Fenech and Keaveny (1999) have demonstrated that the von Mises criterion is inaccurate in assessing trabecular bone performance. In general, SED is the most widely accepted mechanical stimulus for bone remodeling in biomechanics (Mirulla et al., 2021).

In addition to the applications mentioned above, the computational models were also used to investigate the inhibiting effect of bisphosphonate on bone loss and the impact of bon trabecular bone structure on stress shielding (Nyman et al., 2006; Srinivasan et al., 2017).

2.2.3 Tibial strain sensitivities to common TKA factors

Many TKA factors influence the tibial strain distributions after knee arthroplasty. Scott and Biant reviewed the impact of several design factors of the tibial components on the strain and stress shielding (Scott & Biant, 2012). This section will present a more comprehensive review of the literature investigating the impact of TKA factors on bone stress, bone strain, stress shielding, and bone remodeling. The reviewed factors include surgery, patient, and implant design.

2.2.3.1 The material of the tibial component

The material properties of the tibial prostheses influence how the stress transmits from femoral-insert contact to the tibial bone under the tray plate and the stem (Scott & Biant, 2012). The commonly used materials for tibial components are cobalt-chrome (CoCr),

titanium (Ti), and polyethylene (PE). The effect of stress shielding depends on the difference in elastic modulus (*E*) between the implant material and surrounding bone. A stiffer implant will take and shield more loads from going to the bone. A cobalt-chrome tray (*E* = 210GPa) with a 40 mm-length stem transmits 73% of the loads through the stem, whereas an all-polyethylene tibial component (*E* = 1.2GPa) conveys only 36% of the loads through the stem (Eidel et al., 2020). Studies have reported that a cobalt-chrome tray resulted in much greater stress shielding than an all-polyethylene one (stiffness mismatch ratio is 175:1 for CoCr *versus* PE) (Au et al., 2007; Eidel et al., 2020; Jia et al., 2017; Small et al., 2010; Zhang et al., 2016b). The bone resorption in the proximal tibial was predicted as high as 50% for metal-backed components but less than 10% for all-polyethylene components (Zhang et al., 2016b). However, almost no difference in stress shielding was found between components made of titanium (*E* = 110GPa) and cobalt-chrome (stiffness mismatch ratio is roughly 2:1 for CoCr *versus* Ti) (Eidel et al., 2020).

2.2.3.2 The length of tray stem

The length of the tray stem influences how distal the stress is transmitted through the stem to the tibia. Meanwhile, a longer stem also transmits more loads through the stem than a shorter one. For metal-backed components, the plate-stem force transmission ratio was up to 17:83 for a 75-mm length stem and 27:73 for a 40-mm length stem (Eidel et al., 2020). This change of load transmission due to different stem lengths does not occur with all-polyethylene stems due to the significantly reduced stiffness of the construct. Many studies have reported that the long stem produced more serious stress shielding than the short stem (Completo et al., 2009; Eidel et al., 2020; Jia et al., 2017; Rawlinson et al.,

2005). A computational study predicted that a 110 mm stem would result in about 10% more bone loss in the proximal tibia comparing with a 30 mm stem (Jia et al., 2017). However, long stems could provide better mechanical stability due to the less shear stress produced in the tibia.

2.2.3.3 Stem type and geometry

One computational study compared the effect of five types of stem design: straight stem, offset stem with supplements, offset stem without supplements, sleeve with stem, and sleeve without stem (Quilez et al., 2017). The highest bone resorption was predicted for the offset prosthesis without the supplement, and the highest bone formation was computed for the straight stem. Other authors reported that the use of stems could reduce the strains in proximal tibia by 30~50%, and thus suggested that the stem may be needless in tibiae of sufficient stiffness (Rawlinson et al., 2005).

2.2.3.4 Tibial fixation techniques

Tibial fixation techniques include full cementation, surface cementation, and cementless. Full cementation involves cementing both the tibial tray and stem (Abu-Rajab et al., 2006; Lonner et al., 2001). Surface cementation, also called hybrid cementing, indicates that the cement is applied underneath the tibial tray but leaving the stem uncemented (Adalberth et al., 2001; Schai et al., 1998). Cementless implies that the fixation relies on bony ingrowth (Whiteside, 2001). Strain gauge experiments reported that lower surface strains were measured for full cementation compared to surface cementation, which indicated more bone resorption might occur in the proximal tibia with full cementation

(Cawley et al., 2012; Completo et al., 2008c). This finding has been verified by bone remodeling simulations where more extensive bone resorption under the baseplate was predicted for full cementation (43%) than for surface cementation (29%) (Cawley et al., 2012; Chong et al., 2011b). The force shielded from going to the bone with full cementation was predicted 7~15% more than surface cementation cases according to the length of the stem (Eidel et al., 2020).

2.2.3.5 Implant alignment parameters

Mechanical alignment is a technique that aims to position both femoral and tibial components perpendicular to the mechanical axis of each bone despite any preoperative deformities (Sappey-Marinier et al., 2020). Kinematic alignment, also referred to as anatomic alignment, aims to restore pre-arthritic alignment and maintain the native joint line position (Howell et al., 2013; Waterson et al., 2016). Both experimental and computational studies have reported considerable strain increases in the medial-proximal tibia due to changes in femoral-insert contact conditions (Anijs et al., 2020; Green et al., 2002; Nakamura et al., 2017; Perillo-Marcone & Taylor, 2006; Zhang et al., 2016b). A bone remodeling simulation predicted more bone loss in the medial region for mechanically aligned tibia compared to the kinematically aligned model (24.8% *versus* 7%) at a simulated time point of two years after TKA (Anjis et al., 2020).

2.2.3.6 Fixed-bearing vs. rotating-platform design

An *in-vivo* study followed 54 knees for two years and found no evidence of differences in bone loss between fixed-bearing and rotating-platform designs (Munro et al., 2010).

While an *in-vitro* study comparing those two designs in synthetic tibiae reported that fixed-bearing knee replacement exhibited higher cortical strains (Malinzak et al., 2014). The disagreement from the *in-vitro* experiment is supposed due to the lack of physiological representations in both bone and loading conditions.

2.2.3.7 Tibial resection level

The resection surface area at the tibial plateau decreases with the increasing resection depth, which leads to the implantation of smaller tibial components with less underlying bony support. A synthetic bone experiment reported that the strains increased up to 281% in the proximal and peripheral regions of the tibia with 15 mm of tibial resection compared with 5 mm resection (Berend et al., 2010). However, it should be noted that this significantly increased strain could cause cancellous damage.

2.2.3.8 Femoral component

A computational study investigated the influence of the femoral stem extensions (press-fit or cemented) and the constrain types (posterior-stabilized and varus-valgus constrained) on proximal tibia strain distributions. The results indicated the strain behavior of cancellous bone under the tibial tray is not completely immune to the use of femoral stems. However, the level of the change is small compared with the strain magnitudes (Completo et al., 2010).

2.3 Investigation of tray-bone micromotion in cementless TKA

2.3.1 Experimental investigations

The initial fixation of cementless tibial trays after total knee arthroplasty is crucial to bony ingrowth onto the porous surface of the implants, as micromotion magnitudes exceeding 150 μm may inhibit bone formations and limit fixation (Engh et al., 1992; Pilliar et al., 1986). Because the tray-bone interface typically cannot be measured experimentally, previous *in-vitro* studies evaluated the cementless fixation performance by measuring and comparing the subsidence or liftoff of the baseplate with the critical micromotion magnitude for bone ingrowth (Bhimji & Meneghini, 2012, 2014; Crook et al., 2017; Kraemer et al., 1995; Yildirim et al., 2016).

LVDTs (linear variable differential transformers) were widely used to measure the relative displacement between the exposed surfaces of the tray and tibia (Figure 2.3a) (Alipit et al., 2021; Bhimji & Meneghini, 2012; Crook et al., 2017; Meneghini et al., 2011; Yoshii et al., 1992). An LVDT is an electromechanical sensor that converts a linear displacement into an electrical signal containing the information of direction and amplitude (Wikipedia contributors, 2021c). When measuring the tray-bone relative displacement, LVDTs are usually mounted on a rigid frame attached to the tibia and let the LVDT plungers contact the surface of the markers (usually cubes or spheres) that are fixed to the tray baseplate. After applying the loads to the construct, the tray-bone relative displacement along the plunger axis at those measurement points will be calculated from the electrical signal produced by the motion of the plungers. Since LVDTs can only measure the displacement in one direction, simultaneously measuring the displacement in multi-directions requires more sensors. However, the number of LVDTs can be used in a single

test is limited due to the testing space restriction (no more than six according to the literature). Therefore, the measurement of tray-bone relative displacement is limited to a few distinct points and directions, which cannot reflect the actual micromotion distributions around the baseplate.

The digital image correlation system allows a full-field surface displacement measurement (Figure 2.3b). It has been used in previous studies to measure the tray-bone relative displacements, although a small portion of the tray-bone surface cannot be measured due to the obstacle of the testing devices (Han et al., 2021; Noble et al., 2017; Small et al., 2016, 2019; Yildirim et al., 2016). In preparation for DIC measurement, a speckle pattern is required to be applied to the outer surface of the tibia and the cementless prosthesis. During the tests, the displacement of each spot will be recorded by the DIC camera, and the relative displacement between the tray and bone can be thus calculated. DIC measurements are in three dimensions, and the accuracy can be within 5 μm. However, limitations are still associated with LVDT and DIC measurements. The main drawback is that these measured tray-bone relative displacements may not represent the actual tray-bone interface micromotion. The measured change in distance is a combination of the deformation of cancellous bone underlying the tray and the motion of the tray relative to the bone. However, the surface bone (where markers were attached) is usually unstressed and thus has no deformation. Therefore, the deformation of the cancellous bone underlying the tray is also counted into the measurement, which would cause the underestimation of the tray liftoff.

Moreover, in the subsidence motion, the bone under the baseplate subsides together with the tray, where there are no gaps between the tray and bone. The actual interface

micromotion in the superior-inferior direction should almost be zero. Han et al. calculated the tray-bone interface micromotion by averaging the surface displacement data and reported that the maximum interface micromotion occurred at the posterior zones (where subsidence displacements were observed) during stair descent activity (Han et al., 2021). Such investigations using the measured subsidence displacement to represent the actual interface micromotion would cause serious misjudgment on the implant fixation stability.

Early experimental studies mostly applied simple compressive loads or the combination of compressive and shear loads when investigating the tray-bone micromotion (Kraemer et al., 1995; Meneghini et al., 2011; Yoshii et al., 1992). One study reported that the physiological loading could generate larger micromotions and better detect differences between devices than the simplified loading (Bhimji & Meneghini, 2012). Many subsequent investigations started considering physiological loads (Bhimji & Meneghini, 2014; Han et al., 2021; Noble et al., 2017). Due to the restriction of the testing devices, some studies were not able to apply full-cycle loads but used the peak loading of physiological activities instead (Crook et al., 2017; Han et al., 2021). However, one study testing different tray designs under five full-cycle physiological loads revealed that the peak micromotion did not necessarily occur at the peak loads (M. Taylor et al., 2012). These findings highlighted the need to apply physiological loads and examine the whole cycle when investigating the tray-bone micromotion.

Previous studies investigating tray-bone micromotions mainly focused on comparing the influence of different fixation features on fixation stability. Synthetic bones were mostly used for their excellent comparative performance and easy research setting (Alipit et al., 2021; Bhimji & Meneghini, 2012; Crook et al., 2017; Small et al., 2016). However,

the use of natural bone in assessing TKA component stability offers a realistic representation of the *in-vivo* situation. Small et al. performed the same tests on synthetic and cadaveric tibiae to study the impact of different fixation designs on the primary stability (Small et al., 2019). Similar conclusions were drawn for synthetic and natural bones, but the micromotion values were found different. This confirms that testing within native tibial specimens is necessitated. However, because the micromotion tests usually involve hundreds of loading cycles for implant bedding-in and different activities, the cadaveric specimens have a high risk of fracture during the tests. Therefore, the applied loads were sometimes scaled to minimize the risk of specimen failure, which may limit the use of cadaveric bone in investigating the tray-bone micromotion (Han et al., 2021).

2.3.2 Computational predictions

Computational models have been commonly used to predict the tray-bone interface micromotion (Figure 2.4) (Chong et al., 2010; Glenday et al., 2021; Hashemi & Shirazi-adl, 2000; Rahimizadeh et al., 2018; Totoribe et al., 2018). As described previously, the experimentally measured tray-bone relative displacement cannot represent the actual interface micromotion. Therefore, the computational predictions of the interface micromotion provide more reasonable and accurate evaluations of the cementless fixation. The tray-bone interface micromotion is defined at the relative motions between the tray and the tibia contact surface. In computational models, the changes in the relative distance (total of the three translational components) between the nodes at the tray bottom surface and the nearest nodes at the tibia implantation surface were used to represent the tray-bone interface micromotion.

Realistically modeling the contact between the bone and cementless tibial component is challenging. Firstly, both the human trabecular bone and the porous surface of the cementless component have complex structures. Previous computational studies usually modeled the porous-bone contact surfaces with Coulomb friction, ranging from 0.6 to 1.1 (Chong et al., 2016; Glenday et al., 2021; M. Taylor et al., 2012). Secondly, the values of the interference fit are highly dependent on the surgical operations. The achieved interference fit is probably much lower as removing the reamer and inserting a rough-coated implant is likely to remove and crush further material (Shirazi-adl et al., 1994). The interference fit could further reduce significantly due to the viscoelasticity of the human bones (Norman et al., 2005). Therefore, previous studies usually assumed the bone-implant interfaces to be line-to-line (no interference fit). A computational study also showed that an interference fit of 0.15 mm only caused 10.6% changes in the predicted micromotion (Navacchia et al., 2018).

The cementless fixation relies on the bone ingrowth into the porous spaces of the tibial component. More contact area with osseointegration indicates a stronger fixation. Therefore, solely investigating and comparing the maximum micromotion values with the critical value for bone ingrowth is not enough to accurately evaluate the implant fixation performance. Chong et al. predicted the tray-bone interface micromotion for three implant designs and found that the design with larger peak micromotion could have a greater extent of osseointegration under all simulated loading conditions (Chong et al., 2016). Therefore, some computational studies predicted the surface area experiencing small micromotions as another indicator for assessing the cementless fixation (Chong et al., 2010; Glenday et al., 2021; M. Taylor et al., 2012). The commonly adopted micromotion threshold for bone

ingrowth is 50 μm, below which the formation of bone tissue has been observed *in-vivo* (Jasty et al., 1997a). In contrast, fibrous tissue formation is known to occur where micromotions exceed 150 μm (Jasty et al., 1997b; Kienapfel et al., 1999; Pilliar et al., 1986). The computationally predicted surface area for bone ingrowth has been used to compare the fixation stability between different designs, loading conditions, and implant alignments (Chong et al., 2010, 2016; Glenday et al., 2021; M. Taylor et al., 2012).

Most of the computational studies used natural tibia models, as the human bone model offers a physiological representation of the in-vivo situation meanwhile without any risk of bone failure. Additionally, human bone models can be repeatedly implanted with different designs and alignment parameters, which isolates the impact of bone anatomy that cannot be avoided in experimental tests. For modeling convenience, some studies applied the loads directly at the central reference node of the tray (Glenday et al., 2021; Totoribe et al., 2018), where the impact of contact locations and mediolateral force distributions on micromotions was neglected. One of our studies has shown that the tray-bone interface micromotion was very sensitive to the anterior-posterior contact location (H. Yang et al., 2020). For a comprehensive investigation on the tray-bone interface micromotion, the simulated loading should be physiological, continuous (full-cycle), and multi-activities (Bhimji & Meneghini, 2012; Noble et al., 2017; M. Taylor et al., 2012).

2.3.3 Tray-bone micromotion sensitivities to common TKA factors

Many TKA factors may influence the tray-bone interface micromotion, such as surgical parameters, implant designs, and patient anatomy. However, since the cementless fixation in knee arthroplasty has become popular most recently (Aprato et al., 2016; Asokan et al.,

2021), there is not much research investigating the cementless micromotion sensitivities to TKA factors. This section is dedicated to list the TKA factors studied in previous literature and outline their corresponding impact on the tray-bone interface micromotion.

2.3.3.1 Fixation features

Many fixation features exist, such as cone, stem, keel, pegs, and screws, with different sizes, shapes, and incline angles. Chong et al. computationally compared the tray-bone interface micromotions between mini-keel tibial components and a standard stemmed design (Chong et al., 2016). The prosthesis surface area amenable for bone ingrowth for the mini-keel design was predicted to be at least 67% larger than the stemmed implant, thereby reducing the risk of long-term aseptic loosening.

The screw fixation was used in early TKA but less adopted in recent years as it can cause increasing osteolysis around the screws (Ersan et al., 2017). Both experimental and computational studies have reported that screw fixation could reduce the micromotion and liftoff comparing with the peg fixation (Hashemi & Shirazi-adl, 2000; Kraemer et al., 1995; Tissakht et al., 1995).

Several studies compared the fixation stability between the keel and pegs in terms of the tray-bone micromotion, and all found that the keel provided more stability than the pegs (Bhimji & Meneghini, 2012; Meneghini et al., 2011). The most significant differences in micromotion were reported between the dual-hex peg implant and the keel with pegs design during the stair descent activity (644 μm *versus* 144 μm, respectively) (Bhimji & Meneghini, 2012).

2.3.3.2 The length of tray stem

It has been reviewed in *Section 2.3.2.2* that a longer stem could provide better mechanical stability due to the less shear stress produced in the tibia. Therefore, a longer stem also resulted in less tray-bone micromotion due to the increased stability (Chong et al., 2016; Yoshii et al., 1992). It has been found that long stems minimized the rocking motion (subsidence and liftoff) of the prosthesis, but no significant difference between short stem and stemless designs (Yoshii et al., 1992). A computational study also predicted up to 32% reduction in the peak micromotion with a stem extension of 45 mm (Chong et al., 2016).

2.3.3.3 Implant alignment parameters

The mechanical alignment provides a relatively balanced joint load transfer (Sappey-Marinier et al., 2020b). While a varus alignment may help improve knee kinematics and ligament balance but increases the load carried by the medial compartment of the knee (Niki et al., 2017; Smith et al., 2016). One study has reported that a 2° of tibial varus alignment could result in 79% increased peak micromotion 59% and 18% reduced surface area for bone ingrowth than a mechanical alignment (Glenday et al., 2021).

2.3.3.4 Cruciate-retaining vs. posterior-stabilized design

A computational study investigating the micromotion of cruciate-retaining (CR) and posterior-stabilized (PS) designs during gait and stair descent activities reported that PS implants had 50% less micromotion than CR components (Muellor et al., 2020). The

predicted peak tray-bone micromotion occurred at walking for the CR design while at stair descent for the PS implant.

2.4 Gaps and opportunities

Understanding the critical parameters influencing post-operative SED distribution and implant-bone micromotions is essential to improve TKA fixation. However, these variables typically cannot be measured experimentally. Computational models have been commonly used to predict the tibial strain and micromotion and investigate corresponding influencing factors. Although many related studies have been performed previously, there are still important limitations that need to be addressed to cement their findings in clinical practice.

2.4.1 Model validation

Validation is the process of determining how well the model accurately represents the real world through comparison to experimental data (Henninger et al., 2010). A computational model of the human body needs to be validated in order to be trusted. Once the models are validated, they can be further used for analyses that are difficult or impossible to conduct via experimental methods. For instance, a validated intact knee model may be used to simulate soft tissue injury and quantitatively assess the effect of surgical decisions on patellofemoral mechanics and extensor mechanism efficiency (A. A. Ali et al., 2016); A validated wear model allows a more time- and cost-efficient investigation of the polyethylene wear under different conditions than physical testing (Knight et al., 2007); Validated lower limb models could be further used to evaluate TKA designs and surgical techniques (A. A. Ali et al., 2020; Fitzpatrick et al., 2012); The AMTI

VIVO knee simulator has been modeled and validated to simulate the experimental tests without the impact of experimental errors (Figure 2.1) (Fitzpatrick et al., 2016).

However, only a limited number of studies performed model validations when investigating bone strains and tray-bone micromotions. Some studies validated their models by using synthetic bone (Completo et al., 2007; Navacchia et al., 2018). While artificial bones are preferred for the low-cost and easy implantation procedures, human bones have real and heterogeneous material property distributions which reflect the anatomical location and subject-specific factors. Thus, using natural bone models enable more physiological investigation of the bone strains and tray-bone interface micromotions. However, the validation of real bone models is challenging due to the heterogeneous material property. The same bone density could have up to 53% differences in elastic properties between samples due to the different trabecular architectures (Ulrich et al., 1997), which brings vast uncertainty when determining the bone density-elasticity relationship. Moreover, previous studies validated their computational models by solely considering surface strains or the relative displacement around the tray-bone interface (Chong et al., 2010; Completo et al., 2007; Navacchia et al., 2018; Simpson et al., 2009). However, these location-specific comparisons may not reflect the validity of the entire model, particularly for human bones which possess heterogeneous material properties.

Concluding from the above deficiencies, the reliability of the computational validation could be improved by simultaneously considering both bone surface strains and tray-bone interface micromotions. Also, most of the previous validation works considered only the peak loading of a single activity (Chong et al., 2010; Completo et al., 2007; Simpson et al., 2009). As described previously, the simulated loading should be physiological, continuous

(full-cycle), and multi-activities for more comprehensive and accurate investigations (Bhimji & Meneghini, 2012; Noble et al., 2017; M. Taylor et al., 2012).

2.4.2 Model application

Computational models have been used to investigate the impact of various TKA factors on bone strain and micromotion (See section 2.2.3 and 2.3.3), although model validations were mostly lacking.

In previous bone strain studies, testing loads have been typically applied uniformly on the surface of the polyethylene insert or tibial plateau, without additional soft tissue loading on the tibia. However, it has been reported that the joint kinematics and muscle loading had significant impacts on the bone strain distributions (Duda et al., 1998; Perillo-Marcone & Taylor, 2006). To the author's knowledge, none of the previous studies considered both femoral-insert contact (contact locations and force directions) and soft tissue loading conditions (tendon and ligament forces and directions) when investigating bone strains. Additionally, the impact of some common TKA factors on bone strain distributions has not been investigated yet, such as ligament balancing and patient anatomy.

For tray-bone micromotion studies, previous studies have primarily estimated the tray-bone micromotion under different loading conditions (Chong et al., 2010; M. Taylor et al., 2012), although a few also investigated the micromotion sensitivity of key factors such as implant alignment, design features, or individual differences (Hashemi & Shirazi-adl, 2000; Tissakht et al., 1995). However, the loading conditions applied in these studies were typically simple vertical loads which do not account for the more complex physiological loading at the knee joint during daily activities. Additionally, many TKA factors that were

foreseen to affect the tibial fixation have not been studied yet. For example, maximizing tibial coverage is thought to improve fixation due to the more uniform distribution of the forces (Bertin, 2007; S. Martin et al., 2014; Wernecke et al., 2012); The resection errors relative to the TKA cutting guide were likely to influence the fixation stability (Plaskos et al., 2002); Differences in tibial elastic properties between samples were also expected to affect the fixation performance. To our best knowledge, no one has systematically studied the impact of these common TKA factors on the tray-bone micromotion under physiological conditions.

Figure 2.1: The AMTI VIVO^{TM} knee simulator (left) and its validated computational model (right-bottom) (Fitzpatrick et al., 2016). The upper stage can apply flexion-extension and varus-valgus motions/loads, and the lower stage can apply internal-external, superior-inferior, anterior-posterior, and medial-lateral motions/loads.

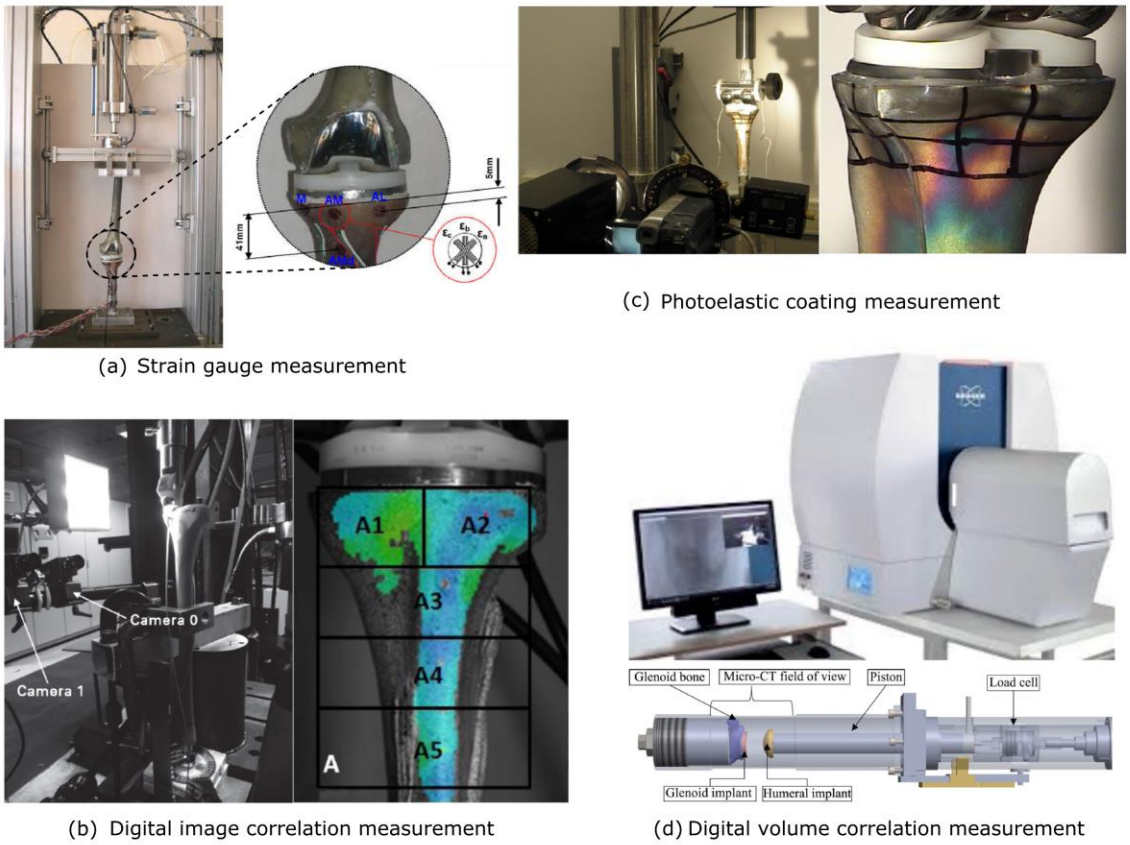

Figure 2.2: Experimental techniques for measuring bone strains. (a) Strain gauge measurement (*Figure source:* Completo et al., 2010, reprinted with permission); (b) Digital image correlation measurement (*Figure source:* Scott et al., 2013; Malinzak et al., 2014, reprinted with permission); (c) Photoelastic coating measurement (*Figure source:* Small et al., 2010, reprinted with permission); (d) Digital volume correlation measurement (*Figure source:* Boulanaache et al., 2020, reprinted with permission).

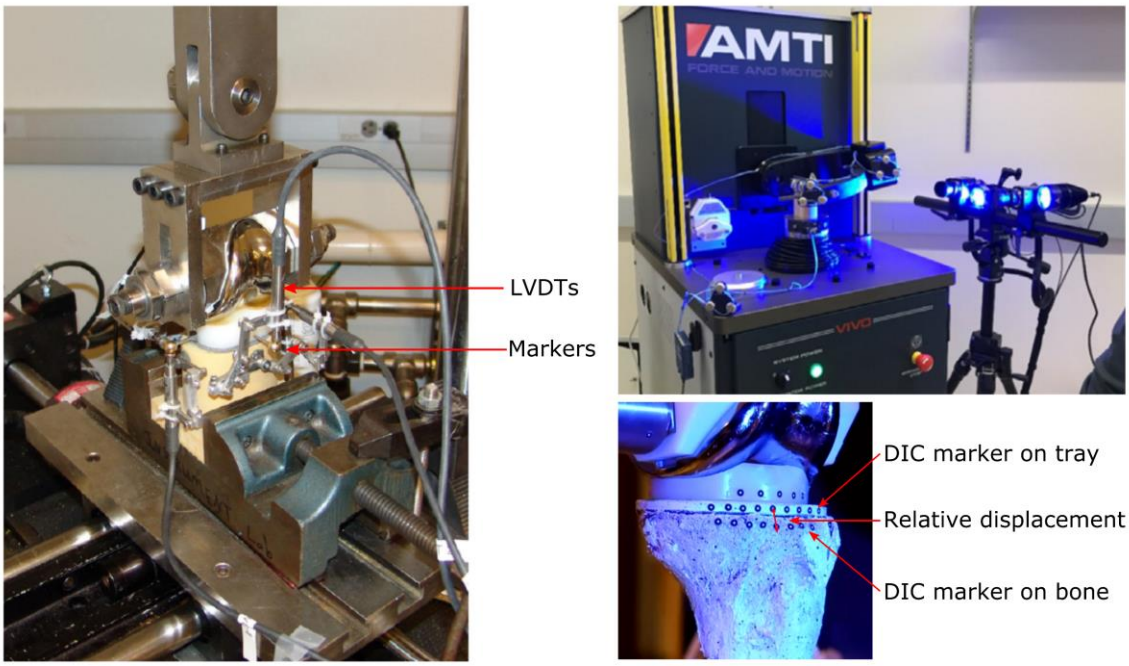

(a) LVDT measurement

(b) DIC measurement

Figure 2.3: Experimental techniques for measuring tray-bone micromotions. (a) LVDT measurement (*Figure source:* Bhimji & Meneghini, 2014, reprinted with permission); (b) Digital image correlation measurement.

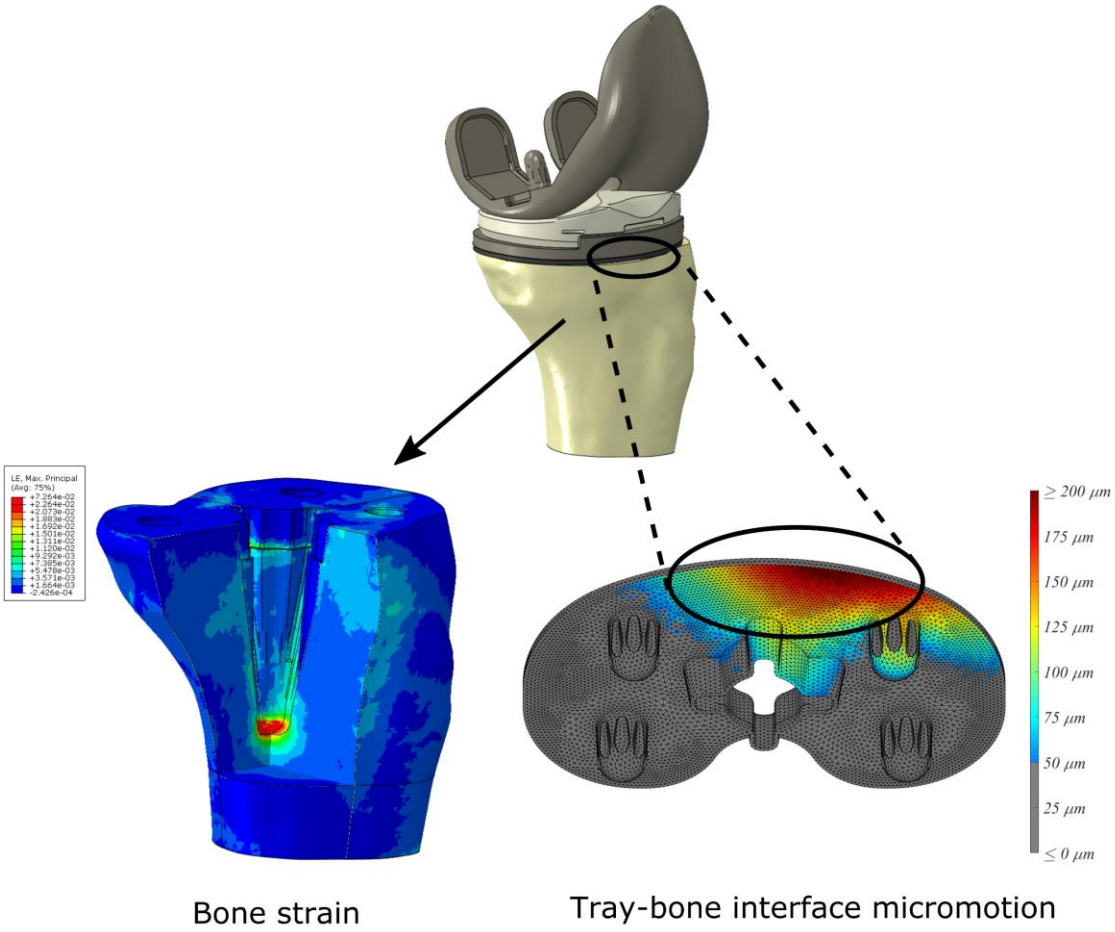

Figure 2.4: Computational predictions of the bone strains (left) and tray-bone interface micromotions (right).

CHAPTER 3. VALIDATION AND SENSITIVITY OF MODEL-PREDICTED PROXIMAL TIBIAL DISPLACEMENT AND TRAY MICROMOTION IN CEMENTLESS TOTAL KNEE ARTHROPLASTY UNDER PHYSIOLOGICAL LOADING CONDITIONS

3.1 Abstract

The initial fixation of cementless tibial trays after total knee arthroplasty is crucial to bony ingrowth onto the porous surface of the implants, as micromotion magnitudes exceeding 150 μm may inhibit bone formations and limit fixation. Experimental measurement of the interface micromotions is still very challenging. Thus, previous studies investigated micromotions at the bone-tray interface via finite element methods, but few performed direct validation via in vitro cadaveric testing under physiological loading conditions. Additionally, previous models were validated by solely considering relative displacements of the marker couples placed around the tray-bone interface. In this study, we present an experimental-computational validation framework for investigating micromotions at the tray-bone interface under physiological conditions. Three cadaveric specimens were implanted with cementless rotating-platform implants and tested under gait, deep knee bending, and stair descent loads. Corresponding subject-specific finite element models were developed and used to predict the marker (tray-bone) relative displacements and tibial surface displacements. Experimental measurements were used to

validate model estimations. Subsequent sensitivity analyses were performed on implantation and friction parameters to represent model uncertainties.

The models appropriately differentiated between locations, activities, and specimens. The average root-mean-square (RMS) differences and correlations between measured marker relative displacements and predictions from the 'best-matching' models were 13.1 μm and 0.86. RMS differences and correlations between measured surface displacements and predictions were 78.9 μm and 0.84. Full-field interface micromotions were investigated and compared with predicted marker relative displacements. The marker relative displacements underestimated the actual interface micromotions. Initial tray-bone alignment in anterior-posterior, flexion-extension, and varus-valgus degrees of freedom have a considerable impact on the interface micromotions. The validated cadaveric models can be further used for pre-clinical assessments of new TKR tray design. The outcomes of the sensitivity analyses provide further insights into reducing interface micromotions via clinical techniques.

3.2 Introduction

Cemented and cementless fixation in total knee arthroplasty (TKA) have been successfully used for decades. As the number of younger and more active patients treated with TKA continues to increase (Kurtz et al., 2009), long-term implant survivorship is of increasing importance. Although there is no significant difference in the performance and longevity between cemented and cementless fixation in TKA (Newman et al., 2018), current innovations in cementless tibial trays offer a more long-lasting biological fixation potential (Dalury, 2016). The primary fixation of cementless tibial trays after TKA is

crucial to bony ingrowth onto the porous surface of the implant (Bragdon et al., 1996) as micromotions exceeding 150 μm may inhibit the bone formation and limit fixation (Pilliar et al., 1986). Therefore, understanding the micromotion at the tray-bone interface is critical for pre-clinical evaluations of new implant designs.

Previous studies investigated *in-vitro* micromotion between tray and bone by comparing the measured subsidence or liftoff of the baseplate (measured using linear variable differential transformers) with the critical micromotion magnitude for bone ingrowth (Bhimji & Meneghini, 2012, 2014; Crook et al., 2017; Kraemer et al., 1995). However, these measurements are limited to a few distinct points at the interface, which may not correspond to actual interface micromotions in terms of magnitude and trend. Also, the micromotion contour map across the interface is not fully known. Experimental measurement of the micromotion at the tray-bone interface requires advanced imaging hardware and protocols (Malfroy Camine et al., 2016). Thus, finite element (FE) models have been commonly used to estimate the interface micromotion. Computational models can complement experiments where data is difficult or impossible to measure. Once the models are validated, they can be further used for detailed analyses. There are a limited number of studies focusing on tray micromotions in cementless TKA which included validated FE models to evaluate the interface micromotion. One study developed and validated FE models from cadaveric tests to evaluate the tray-bone interface micromotion (Chong et al., 2010). However, only peak loads during gait were considered, which cannot fully account for the varying loads throughout the gait cycle. Also, the loading conditions tested in the previous studies mainly included a single vertical load (Crook et al., 2017; Hashemi & Shirazi-adl, 2000; Yoshii et al., 1992) or a single daily activity (Bhimji &

Meneghini, 2014; Yildirim et al., 2016). A recent study presented validated computational models for predicting the cementless TKA micromotions in synthetic foam bones over a range of simulated activities of daily life (Navacchia et al., 2018). While synthetic bones (Crook et al., 2017; Yildirim et al., 2016) are preferred for the low cost and easy implantation procedures, cadaveric bones have real and heterogeneous material property distributions which reflect anatomical location and subject-specific factors. Thus, cadaveric tests provide more realistic biological fixation and enable more physiological investigation of the interface micromotion.

To our knowledge, no study has reported validated interface micromotion data (measured in cadaveric specimens implanted with the cementless trays) by considering physiological loading conditions covering multiple dynamic activities of daily living. Additionally, the majority of the previous investigations did not present detailed validation results (Chong et al., 2010) or evaluated interface micromotions without model validations (M. Taylor et al., 2012). Previous studies validated their FE models by solely considering relative displacements of the marker couples placed around the tray-bone interface. However, these location-specific comparisons may not reflect the validity of the entire model, particularly for cadaveric bones which possess heterogeneous material properties. The validation procedure can be improved by also considering bone surface displacements. Furthermore, previous studies only considered the fixed-bearing design for knee prostheses. Interface micromotions for the rotating platform (RP) design in cementless TKA have not been previously studied.

Hence, the objective of this work was to present a validated experimental-computational framework for predicting tibial micromotion and bone deformation during

activities of daily living. Three cadaveric tibiae were implanted with an RP cementless TKA design and were tested via a six-degree-of-freedom (DoF) knee testing machine under gait (GT), deep knee bending (DKB) and stair descent (SD) loading conditions. Relative motions between the marker couples on tray-bone exposed surfaces and anterior tibial surface displacements were measured and compared with the FE predictions.

3.3 Methods

In this study, three cadaveric tibiae were implanted and experimentally tested under physiological loading conditions. Tray-bone relative displacements and the bone surface displacements were recorded at the anterior aspects of the implanted tibiae. The corresponding computational models were developed with all the boundary conditions (implantation alignment, bone fixation, loading condition, and marker couple location, etc.) reproduced from the experiments. The experimental measurements were compared with the predictions for validating the computational models. After validation, the tray-bone interface micromotions were investigated in detail.

3.3.1. Experimental testing

CT scans of three fresh-frozen healthy cadaveric tibiae were taken prior to the experiments and were manually segmented using ScanIP (Simpleware, Exeter, UK) from the CT scans. (Table 3.1). The scan parameters were set at 130 kVp, 107 mA tube current, 0.6-mm thickness slices, and 0.39-mm pixel spacing with a scan field of 200 mm. Each specimen was implanted using mechanical alignment techniques with a cementless tibial prosthesis (best-fit size, rotation-platform, cruciate-retaining, ATTUNE®, Depuy Synthes,

Warsaw, IN) by an experienced surgeon. The specimen was resected 12.7 cm distal from the implantation plane. Good fixation support and sufficient coverage were noted for all the specimens. After the implantation, specimens were cemented into custom fixtures (Figure 3.1). Nine digital image correlation (DIC) target markers were then placed at the anterior aspects of the tray and the bone, respectively. Three markers were additionally placed on the fixture to generate a local coordinate system. A speckle pattern was applied on the anterior surface of the tibia to enable measuring surface displacements. The tray and tibia surfaces were probed using the OPTOTRAK® system (NDI, Waterloo, Ontario) to reproduce the same tray-bone alignment for the FE models. Subsequently, the specimens were mounted into the 6-DoFs AMTI VIVO™ knee simulator (AMTI, Watertown, MA) and were tested under simulated gait (GT), deep-knee bending (DKB), and stair descent (SD) activities. Experimentally applied load and kinematics profiles were derived from telemetric implant data and ASTM 3141-17 (Navacchia et al., 2018). Flexion/extension and internal/external rotation (IE) degrees of freedom (DoFs) were kinematically-driven while medial/lateral (ML), anterior/posterior (AP), superior/inferior (SI), and varus/valgus (VV) DoFs were load controlled. After bedding-in under cyclic compression for 200 cycles, 40 cycles of each activity were performed at a rate of 0.33 Hz. Relative displacements between the corresponding tray-bone marker couples and tibial surface displacements in the local coordinate system were recorded with the ARAMIS DIC system (GOM mbH, Braunschweig, DE) for the 36^{th}-39^{th} cycles (Figure 3.2). Reference images were captured at the unloaded stage before each tested activity to set the displacements to zero and thus ignore any plastic deformation created previously.

3.3.1.1. Loading and boundary conditions

The desired experimental load and kinematics profiles (Figure 3.3) input to the VIVO were usually slightly different from the actual outputs. Hence, the output load and kinematics profiles were recorded for each actuator in the VIVO device and later applied to the finite element models.

3.3.2 Computational modeling

3.3.2.1 Model set up

The position and orientations of the tray and tibia in the experimental set up were reconstructed by registering measured point clouds to respective stereolithography geometry files (Figure 3.1). For this, the iterative closest point algorithm was used, and the root-mean-square (RMS) error of registration was less than 1 mm for both components. The positions of the DIC marker couples were also reproduced during the registration process.

The prosthesis was virtually implanted, and the portion of the distal tibia confined to the fixture was resected in HyperMesh (Altair Engineering Inc., Troy, Michigan). The tray was modeled with a solid portion and a porous coating (represented also as a solid) according to real dimensions. The femoral component was meshed with 1-mm rigid surface elements. The deformable TKA components were meshed with 0.5 mm, first-order, tetrahedral elements, except the solid portion of the tray which was discretized with 1.0 mm elements. The applied mesh sizes were sufficiently fine for convergence (Halloran et al., 2005). The tibia was meshed with first-order, tetrahedral elements, and the most efficient mesh density was identified from our mesh convergence study (0.75 mm at the

coating-bone interface, 1.5 mm on the surface, 3 mm inside the bone; see section 3.4.1 for the result of this convergence study). All components were modeled as linearly elastic and with different material properties, except the insert which was modeled with an elastic-plastic hardening material property (Table 3.2).

Specimen-specific material properties were calculated from the CT scans and were assigned to each tibias element by using an in-house developed, mapping software. The relation between the Hounsfield unit and bone mineral density was derived using a calibration phantom (QCT Pro, Mindways Software, Inc., Austin TX). Previously established relationships were used for calculating the apparent bone density and elastic modulus for the individual elements (Anderson et al., 1992; Kaneko et al., 2004; Linde et al., 1991). A threshold value of 1 g/cm^3 for apparent bone density was used for discriminating cortical bone from trabecular bone. Approximately 400 material cards (1 card per 4 mg/cm^3 bone apparent density) were used for modeling the tibiae based on our convergence study (see section 3.4.1 for the result of this convergence study). Finite element models of the tested specimens were developed in Abaqus/Standard (SIMULIA, Providence, RI). The interaction between the tibia and the coating was defined with friction ($\mu_d = 1.00$) as measured in a previous study (Navacchia et al., 2018). The coating was tied to the solid portion of the tray. The contacts between the polyethylene and metal components (insert–tray and insert–femoral) were modeled with friction ($\mu_d = 0.04$) (Godest et al., 2002). All the contacts were defined as contact pairs with a smooth surface-to-surface contact. We chose the master surfaces to have higher stiffness and the slave surfaces to have lower stiffness. Also, master surfaces had the same or coarser mesh

compared to the slave surfaces. Interference fit was not considered in the FE simulations. However, the impact of the interference fit was assessed.

The implant-bone construct was virtually mounted into the VIVO simulator model (Fitzpatrick et al., 2016) and loaded via a femoral component with the boundary conditions derived from the VIVO. The distal end of the tibia was rigidly fixed to the fixture to efficiently represent the cemented bone-fixture fixation. Two cycles were simulated for each activity based on our convergence study which identified the minimum number of cycles required to reach a steady state (see section 3.4.1 for the result of this convergence study).

3.3.2.2 Model verification and sensitivity

A number of convergence studies were investigated on key modeling factors to verify the predictions of the computational model. The edge lengths of the tibial elements were analyzed with (0.75 and 1.5) mm (tray-bone interface and remaining surface), (1.0 and 2.0) mm and (2.0 and 4.0) mm. For defining material properties of the tibia, 100, 200, 300, and 400 material cards were considered. Tibial elements were grouped into element sets by elastic modulus and density properties. Since the finite element model was mostly load driven, the kinematics paths could change between each simulated cycle. Therefore, ten cycles were continuously simulated and investigated the model convergence. An interference fit of 2, 5, 10, 25, 50, and 100 μm was applied to the pegs at the bottom of the porous coating. The maximum interference fit of 100 μm was considered according to the reported threshold value which is safe against bone fracture (Abdul-Kadir et al., 2008).

Sensitivities of the computational predictions were also investigated to include the potential errors in geometric representation and contact properties. Investigated parameters were applied to the baseline model (the initial model developed from the experiment) and were as follow:

- Tray-bone alignment: Twelve models were developed by perturbing tray-bone alignment (considering one perturbation at a time): ±0.5 mm in anterior-posterior (AP), ±0.5 mm in medial-lateral (ML), and ±0.25 mm translation in superior-inferior (SI), and ±0.25° in tibial slope, ±0.25° in varus-valgus (VV), and ±1° rotation in internal-external (IE).
- Tibia marker locations: For each marker (re-constructed during the registration step), twelve nearest nodes on the tibia surface were selected. Thus, each tray-bone marker couple had twelve possible configurations. The distances between each possible marker (node) and the initial marker location were less than 1 mm.
- The coefficient of friction: The mean coefficient of friction was defined as 1.00 at the tray-bone interface based on test data from the manufacturer, and the coefficient of friction was perturbed in a range of 0.80-1.20 to represent the experimental variability.

All verification and sensitivity study parameters were firstly investigated on the first specimen for the gait activity. The impact of each sensitivity parameter on the bone-implant relative displacements was identified. Subsequently, upper and lower-bound model

configurations were developed from all the sensitivity parameters. The developed upper and lower bound configurations were later applied to all the specimens to study GT, DKB and SD activities.

3.3.3 Data analysis

3.3.3.1 Marker relative displacements

For each activity of all the specimens, the predicted and measured relative displacements of the medial, central, and lateral marker couples were compared. Thirty-six results (the baseline, upper and lower-bound model configurations with 12 marker pair configurations) characterized the uncertainty bounds for each marker. The average root-mean-square (RMS) differences between measured and predicted marker relative displacements and Pearson's correlations were calculated to evaluate the overall performance of the computational models. The configuration with the lowest RMS difference (considering medial, central, and lateral markers concurrently) was identified as the 'best-matching' model. Similarly, the configuration with the largest RMS difference was identified as the 'worst-case' model. The Pearson's correlations between the predictions of the best matching models and the corresponding experimental measurements *(intra*-activity correlation) were also calculated. In addition, the correlations between the same predictions and the measurements from the other two activities (*inter*-activity correlations) were calculated to assess if the models might distinguish between activities.

3.3.3.2 Tibial surface displacement

For each activity, the anterior surface displacement of the tibiae captured by the DIC system was re-constructed in the computational model. The average differences between predicted and measured tibial surface displacements were calculated. The surface displacements at 30%, 50% and 70% of the activity cycle were graphically compared. The anterior surface of the tibia was divided into five regions, and the average displacement within each region was calculated for every 1% of the activity cycle (Figure 3.2). The Correlation between the predicted and measured surface displacements for these regions was calculated and visualized graphically by creating a scatter plot and applying linear regression. Similar to relative marker displacements, the *inter*- and *intra*-activity correlations were also calculated. We defined the tibial regions illustrated in Figure 3.2 as follows. The captured tibia surface was firstly divided into superior (regions 1–3) and inferior (regions 4–5) parts having the same height. The regions in the superior (three regions) and inferior (two regions) parts were then constructed to have approximately equal areas in the corresponding parts.

3.3.3.3 Tray-bone interface micromotions

In this study, we defined the tray-bone interface micromotion as the relative motions between the tray and the tibia contact surface. In computational models, the changes in the relative distance (total of the three translational components) between the nodes at the tray bottom surface and the nearest nodes at the tibia implantation surface were used to represent the tray-bone interface micromotion. For each activity, the micromotion at the tray-bone interface was predicted. The micromotion contour map for the frame having the

peak micromotion was also presented. The maximum values of the interface micromotions through the entire activity cycle were compared to the predicted marker relative displacements to assess if the marker relative displacements can represent actual interface micromotions. The Pearson correlations and maximum differences between these two features were also calculated. The maximum values of the interface micromotion predictions from the baseline, upper and lower-bound models were also compared.

3.4 Results

In this section, the findings from the convergence and sensitivity studies are presented first as these dictated some model parameters. We then compared experimentally measured marker relative and bone surface displacements to computational predictions for validating the developed models. Subsequently, interface micromotions predicted by the validated computer models are reported.

3.4.1 Model setup and sensitivity

3.4.1.1 Mesh convergence study

The RMS differences between the predicted maker relative displacements when using 0.75 and 1.0 mm mesh sizes were 1.39, 2.57, and 1.15 μm (medial, central, and lateral). These differences were on average 0.8% of the relative displacement ranges. The maximum difference between the tibial surface displacements with the two mesh sizes was 19.4 μm (2.2% of the maximum displacement). Based on these mesh evaluations, 1.0 mm was considered acceptable for further analyses.

3.4.1.2 Number of materials to represent tibial bone

The average RMS difference between the marker relative displacements estimated with 100 and 400 material cards were 1.15, 1.09, and 0.86 μm (medial, central, and lateral), which were on average 0.5% of the relative displacement ranges. The maximum difference between the tibial surface displacements was 11.5 μm (1.3%).

3.4.1.3 Number of activity loading cycles represented

The maximum marker relative displacement and maximum surface displacement predicted from the first simulated cycle were 141.6 μm (68.8%) and 235.0 μm (26.6%) smaller than the predictions from the 2nd cycle. The maximum differences between the marker relative displacements predicted from the 2nd cycle and any subsequent cycle were 1.23, 1.50, and 1.90 μm (medial, central, and lateral), which were on average 0.7% of the relative displacement ranges. The maximum difference between the tibial surface displacements was 29.2 μm (3.3%).

3.4.1.4 Line-to-line vs. interference fit for tray in bone

The maximum interface micromotion predicted by applying 100 μm interference fit was 33.0 μm (15.9%) reduced comparing with the prediction without interference fit (Figure 3.4). The maximum difference between the tibial surface displacements was 43.3 μm (4.9%).

3.4.1.5 Impact of tray alignment

The results of the sensitivity analyses are shown in Figure 3.5. Perturbations of the tray alignment in AP and tibial slope directions resulted in 8.78% and 5.05% changes in marker relative displacement ranges. Average changes caused by perturbations along ML (3.22%), SI (3.76%), VV (1.94%), and IE (0.77%) directions and in friction coefficient (1.04%) were much smaller. Percent differences in tibial surface displacements were always less than 5% (for all perturbed parameters).

3.4.2 Marker relative displacements

Measured and predicted marker relative displacements for the three specimens were compared in Figure 3.6 and Table 3.3. The RMS differences and Pearson's correlations between the measured and predicted values were shown. The RMS differences between the measurements and predictions (from the 'best-matching' models) were (16.4, 5.7, 13.0) μm (GT, DKB, and SD), (15.9, 7.7, 22.3) μm, and (12.3, 8.7, 6.6) μm for specimens 1, 2, and 3, respectively. The corresponding correlations were (0.94, 0.88, 0.96), (0.96, 0.95, 0.88), and (0.91, 0.84, 0.93) on average. The *intra*-activity correlations were consistently higher than *inter*-activity correlations for all three specimens (Table 3.4). The RMS differences between the measurements and the predictions from the 'worst-case' models were (33.7, 13.6, 47.5) μm (GT, DKB, and SD), (35.5, 35.2, 48.7) μm, and (21.9, 17.1, 23.2) μm for specimens 1, 2, and 3, respectively. The average difference between the 'best-matching' and the 'worst-case' models was 25.8 μm.

3.4.3 Tibial surface displacements

Since the predictions of tibial surface displacements were not as sensitive to perturbed parameters, only the results from the baseline models were presented in this section. Measured and predicted full-field surface displacements at 30%, 50%, and 70% of the activity cycles are shown in Figure 3.7. The average differences between predicted and measured surface displacements over the entire activities were (13.07%, 10.90%, 6.87%) (GT, DKB, and SD), (10.05%, 8.09%, 5.68%), and (8.34%, 13.44%, 4.76%) for specimens 1, 2, and 3, respectively. The correlations and average RMS differences between predictions and measurements are shown in Figure 3.8. The *intra*-activity correlations were consistently higher than *inter*-activity correlations, except for the second specimen in DKB (Table 3.5).

3.4.4 Tray-bone interface micromotions

The micromotion contour maps at the frames having the peak micromotions were predicted by using the baseline models (Figure 3.9). Peak micromotions were observed at the anterior tray-bone interfaces for all the specimens in each activity, except for the third specimen in DKB, for which almost no micromotion was found at the anterior side. This finding was in agreement with the experimental data (Figure 3.6, specimen 3, DKB) which showed non-positive relative displacements at the anterior side. The correlations between maximum values of the interface micromotions and the marker relative displacements through entire activity cycles were (0.94, 0.22, 0.89) (GT, DKB, and SD), (0.99, 0.93, 0.98), and (0.85, 0.47, 0.89) for specimens 1, 2, and 3, respectively. The maximum values of the predicted interface micromotions were consistently higher than the maximum marker

relative displacements (Figure 3.10). The maximum differences between these two features were (17.8, 28.3, 26.7) µm (GT, DKB, and SD), (6.3, 24.5, 11.7) µm, and (6.3, 25.7, 10.4) µm for specimens 1, 2, and 3, respectively. The maximum values of the interface micromotions predicted from the upper-bound models were consistently higher than those from the baseline models for all specimens in each activity (Table 3.6). On the contrary, the lower-bound models presented consistently lower interface micromotions than the baseline models. Also, interface micromotion and predicted marker couple relative displacements were the highest in gait followed by stair descent, and deep knee bending activities.

3.5 Discussion

A fundamental step in the design of cementless TKR prostheses is to assess their performance under physiological loading conditions. Cadaveric tests are essential since real bone has heterogeneous material property distributions which reproduce real contact conditions. Current in-vitro experimental platforms enable applying physiological loadings in 6-DoFs and measuring micro-level displacements. However, it is usually not feasible to fully measure the micromotion at the implant-bone interface, which is a critical parameter for evaluating the primary fixation. Also, cadaveric specimens are unique and non-reusable after testing. The test conditions applied to one specimen cannot be perfectly replicated when testing other specimens. When studying the impact of a specific factor, the experimental method usually requires a large number of specimens to obtain statistically significant differences, which will highly increase the costs. Validated computational models can address these limitations and enable investigating implant-bone interface

micromotion in detail and more robustly. Desired loading conditions can be tested with the validated models for further studies, even if those loading conditions cannot be tested experimentally. Validated models can be further used to isolate and study the impact of different surgical and patient factors, which are difficult or impossible by only using experimental setups. Consequently, the validation of computational models is crucial to further understand cementless fixation via computational methods.

This study presented a detailed computational-experimental validation framework for investigating implant-bone interface micromotions. In this study, three cadaveric specimens were implanted with cementless, rotating-platform TKR components and were tested under physiological loading conditions. Subject-specific finite element models were developed and used to predict marker relative and tibial surface displacements. Experimental measurements were performed and used to validate model predictions. For all the specimens, different ranges of medial, central, and lateral marker relative displacements were correctly predicted (Figure 3.6), which indicated that developed models distinguished between different locations. Presented significantly higher *intra*-activity correlations (than the *inter*-activity correlations, Table 3.4) demonstrates that the models were able to distinguish between different activities. For each specimen, different trends and ranges of marker relative displacements were measured and captured by the predictions, which pointed out that the models also differentiated between the specimens. The models also computed characteristic tibial surface displacements. Predicted tibial surface displacements successfully captured magnitudes and the trends of the measurements for all the specimens in each activity (Figure 3.7 & 3.8). The differences between *intra* and *inter*-correlations (Table 3.5) also verified the predictions did not share

similarities between different activities. The reliability of the computational validation was improved by accurate predictions of both marker relative and bone surface displacements. Model uncertainties were considered by including the results from upper-bound and lower-bound models. Average RMS differences (for all the specimens) and correlations between the measurements and all the probabilistic results were 19.8 μm and 0.83, while those values were 12.1 μm and 0.92 for the 'best-matching' models. Overall, the models were successful is predicting both trend and magnitude of both marker and surface displacements using the complementary experimental-computational framework. Additionally, experimental measurements showed significant differences in trends and ranges not only between different activities but also among different specimens. Although the first and the third specimens were implanted with the same tray size, measured marker relative displacements were very distinct. These findings confirm the necessity to test real bone geometries under different loading conditions and to consider populations when assessing implant primary stability.

Previous studies either lacked different continuous physiological loading conditions (Chong et al., 2010) or human bone representatives (Navacchia et al., 2018). The loading conditions obtained from AMTI VITO^{TM} knee simulator were always applied to the femoral component (Navacchia et al., 2018), which was inconsistent with the actual operational mechanism of the simulator (two DoFs were applied by upper stage, four by lower stage). To our knowledge, this study is the first to validate cadaveric models for predicting interface micromotions under different physiological loading conditions. The complexity of the validations was further increased by the rotating-platform implant design and including the mechanisms of the knee simulator. Studies validated finite element

models by solely considering regional relative displacements, but the validity of the entire models remains uncertain. This study makes the first attempt to improve the validation process by considering both tibial surface and marker relative displacements.

This study addressed the concern that if marker relative displacements could accurately represent actual tray-bone interface micromotions, as marker displacements were directly used to assess interface micromotions in some previous studies. We found that marker relative displacements well captured the trend of actual interface micromotions but were usually smaller in magnitudes (Figure 3.10). This was mainly due to the fact that peak interface micromotions usually occurred in between the positioned marker couples (Figure 3.9). These underestimations can be partially eliminated by using more markers. For example, for the third specimen in stair descent, the predicted maximum marker relative displacement increased from 116.6 μm (8.2% lower than predicted interface micromotion) to 126.3 μm (3.0% lower) if all nine marker couples (Figure 3.1) were considered.

We also found that uncertainties in modeling parameters had considerable effects on interface micromotions (Table 3.6). The interface micromotions predicted from the upper-bound models were on average (53.2, 21.9, 70.4) μm (GT, DKB, and SD) larger than those predictions from the lower-bound models. This was likely due to the changes in implantation surface modulus, bone coverage, or location of tibial-bone load transfer, which were all altered after perturbations. This suggests that the interface micromotions could be partially minimized by optimizing the alignment of the tray with respect to the bone within a safe range, and that AP and tibial slope are most impactful.

The convergence study indicated that using 100 material cards for modeling the tibia material distributions was sufficient. This was in good agreement with a previous study

(Zannoni et al., 1998). We chose to use around 400 material cards since this parameter did not increase the computational time and is empirically more realistic. In addition, the marker relative and surface displacements predicted from the first simulated cycle were considerably lower than the predictions from the subsequent cycles. This was in contradiction with an earlier study which found that the relative interface motion was larger in the first cycle when including the friction at the bone-implant interface (Verdonschot & Huiskes, 1996). The reason was that the femoral-insert contact locations were not consistent at the beginning and the end for the first cycle since our models were mostly load-controlled, whereas the steady contact paths were observed in subsequent cycles. Therefore, the results from the first cycles were excluded from this study. Although the impact of interference fit on micromotion predictions was considerable (Figure 3.4), the pre-stresses caused by the interference fit would reduce significantly over time due to the viscoelasticity of the human bones (Norman et al., 2005). A previous study estimated the relaxation was approximately 50% (Shultz et al., 2005). In this case, the impact of interference fit would be less than 10.0% in the presented models.

Limitations of this study should be noted. Firstly, rigid bone-fixture fixation was assumed in the computational models. The cement medium inside the fixture was not modeled directly. Non-zero displacements measured at the distal fixation end for the first specimen in all activities (Figure 3.7) indicated that the cement was deformed or not leveled at the fixation level. We believe including a deformable cement component would improve predictions of the surface displacements. Only one density-elasticity relationship was considered for the tibiae specimens. A previous study discussed that each bone specimen could have a characteristic density-elasticity relationship (Eberle et al., 2013). Lastly, the

sensitivity parameters making the upper and lower-bound configurations were developed only from the gait activity. These upper and lower-bound configurations were then directly applied in deep knee bending and stair descent activities. Nevertheless, marker relative displacements (Figure 3.6) and interface micromotions (Table 3.6) indicated that this was a reasonable approach for studying both activities.

In conclusion, this study presented a validated experimental-computational framework (based on cadaveric tests under physiological loading conditions) for investigating micromotions at the cementless tray-bone interface. The reliability of the validations was improved by both considering marker relative displacements and surface displacements. The models differentiated between different locations, activities, and specimens. Initial tray-bone alignment in anterior-posterior, posterior slope, and varus-valgus degrees of freedom have a considerable impact on the interface micromotions. We suggest that some caution should be taken when using marker relative displacements between exposed surfaces to assess actual interface micromotions. The validated cadaveric models presented in this study could be used for further pre-clinical assessment of new TKR designs.

Table 3.1: Specimen information and implantation sizes.

Specimen	Age	Gender	Height (cm)	Left/Right	Implanted tray size
1	53	F	160	Left	5
2	75	F	157.5	Right	4
3	70	F	157.5	Right	5

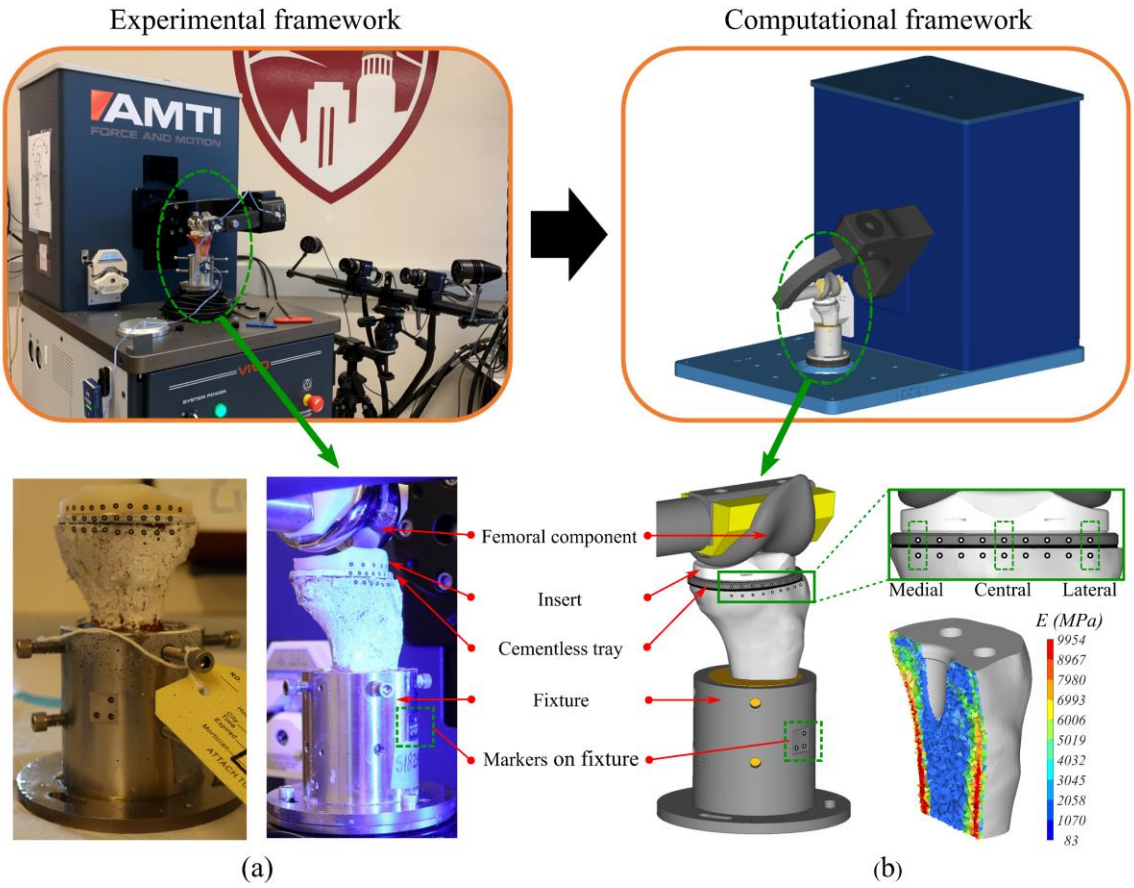

Figure 3.1: (a) Experimental set up with one of the specimens (left knee). (b) The corresponding finite element representation. Highlighted three marker couples (medial, central, and lateral) were used to measure and predict the relative displacement between the tray and tibia. A section view of the tibia with Young's modulus assigned from the CT scans.

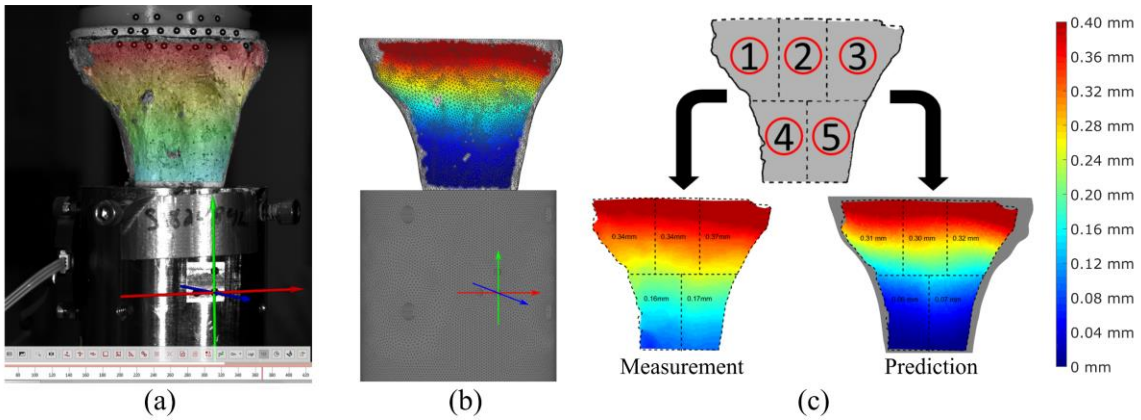

Figure 3.2: (a) Illustration of the anterior tibial surface displacement for one of the specimens (left knee). The fixture-local coordinate system definition is also shown. (b) The corresponding finite element representation. The experimentally captured surface was isolated from the model. (c) Tibial surface was divided into five regions for comparing measured and predicted displacements. Average displacements were calculated within the regions.

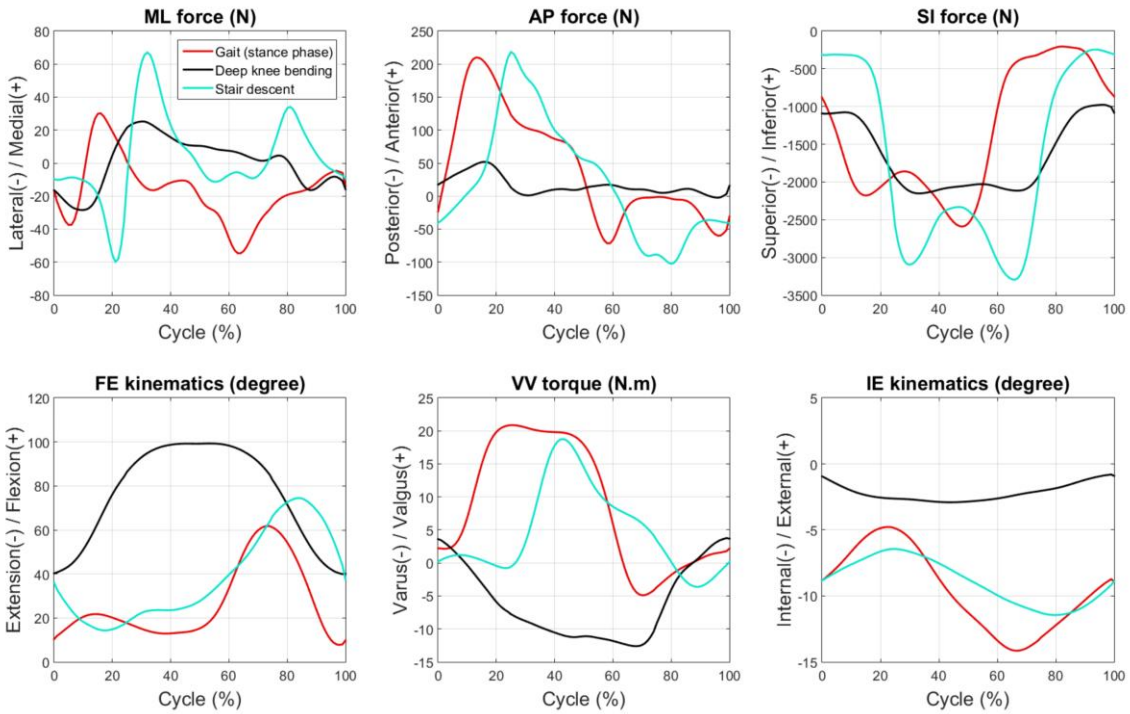

Figure 3.3: The load and kinematics profiles applied to VIVO actuators for a left knee. The flexion/extension kinematics and varus/valgus torque were applied to the femoral component via the upper stage of the VIVO device. The medial/lateral, anterior/posterior, superior/inferior forces, and internal/external kinematics were applied to the implanted tibia via the lower stage.

Table 3.2: Material properties used in the computational models. Transversely isotropic material properties were defined for the porous coating according to internal experimental data. Z- direction is perpendicular to the porous surface.

Material	Density (g/cm^3)	Elastic moduli (MPa)			Yield stress (MPa)	Poisson's ratios		
		E_x	E_y	E_z		ν_{xy}	ν_{yz}	ν_{xz}
Insert - UHMWPE	0.94	571.6			8.1	0.45		
Tray solid - CoCrMo	8.50	220,000			-	0.3		
Tray porous - CoCrMo	0.05	700	700	2200	-	0.083	0.083	0.083
Cortical bone	≥1	≤9954			-	0.3		
Trabecular bone	≤1	≥79.6			-	0.3		

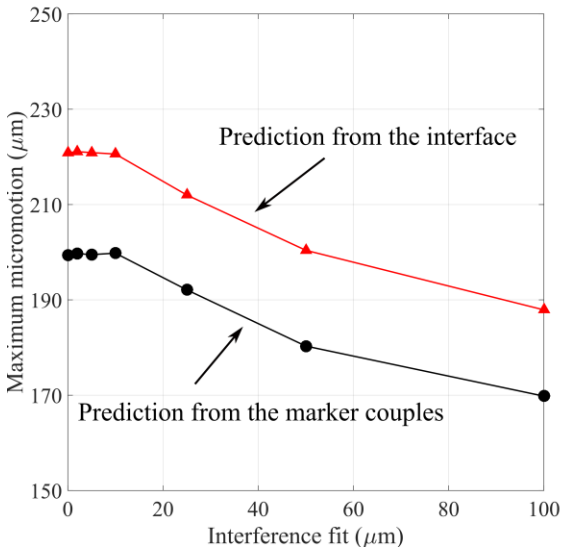

Figure 3.4: The impact of the interference fit on tray-bone micromotion predictions.

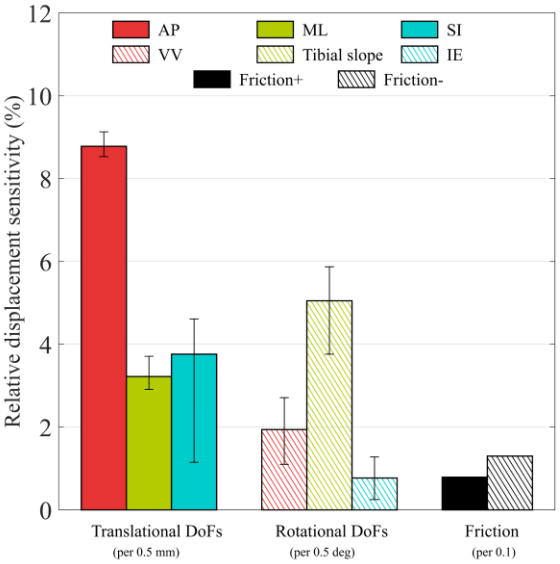

Figure 3.5: The percent changes in marker relative displacement ranges due to perturbed sensitivity parameters. (Friction ±indicates an increase or decrease from the nominal coefficient of friction, μ = 1.00)

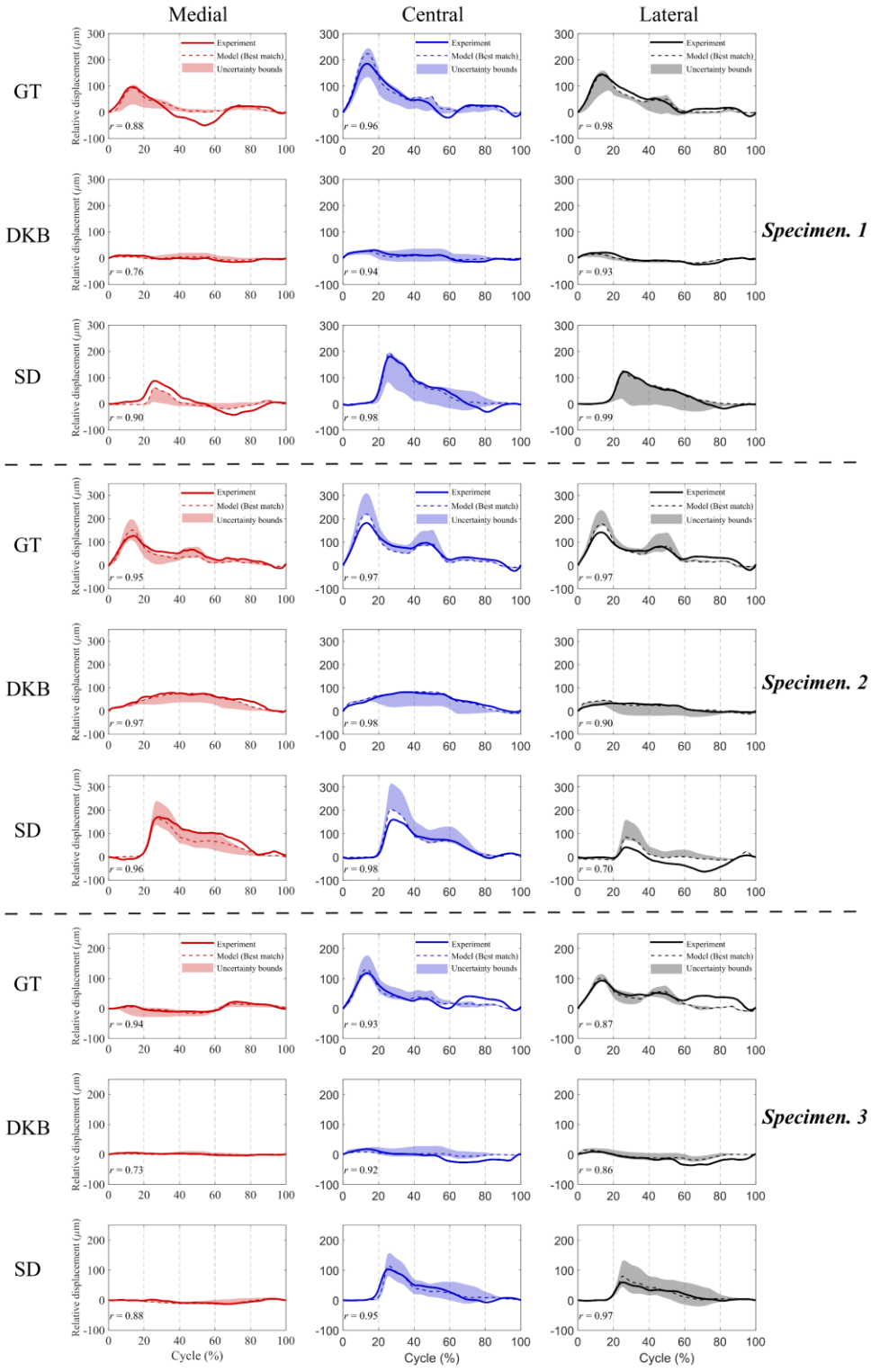

Figure 3.6: Comparison between measured (solid lines) marker relative displacements and the predictions from the 'best-matching' models (dashed lines). Uncertainty bounds (shaded areas) were generated by perturbing implantation parameters and friction coefficients.

Table 3.3: RMS differences (left) and correlations (right) between the measured and predicted marker relative displacements from 36 probabilistic results and the 'best-matching' model (indicated as bold).

Specimen 1

	RMS differences (μm)							Pearson's Correlations					
	Medial		Central		Lateral			Medial		Central		Lateral	
	Best match	Average	***Best match***	Average	***Best match***	Average		***Best match***	Average	***Best match***	Average	***Best match***	Average
GT	**21.81**	26.67	**17.17**	18.17	**10.27**	20.20	GT	**0.88**	0.82	**0.96**	0.96	**0.98**	0.97
DKB	**5.42**	8.37	**5.85**	10.27	**5.94**	7.84	DKB	**0.76**	0.53	**0.94**	0.81	**0.93**	0.86
SD	**19.01**	27.48	**12.40**	31.92	**7.62**	30.86	SD	**0.90**	0.74	**0.98**	0.94	**0.99**	0.82

Specimen 2

GT	**16.19**	19.17	**15.97**	27.57	**15.48**	25.29	GT	**0.95**	0.93	**0.97**	0.97	**0.97**	0.96
DKB	**8.60**	19.61	**6.78**	21.42	**7.71**	19.60	DKB	**0.97**	0.92	**0.98**	0.84	**0.90**	0.55
SD	**23.79**	29.25	**14.18**	33.37	**28.83**	41.35	SD	**0.96**	0.93	**0.98**	0.98	**0.70**	0.62

Specimen 3

GT	**3.89**	7.42	**13.21**	16.48	**19.77**	20.96	GT	**0.94**	0.91	**0.93**	0.91	**0.87**	0.85
DKB	**2.09**	3.17	**12.54**	15.14	**11.58**	13.50	DKB	**0.73**	0.44	**0.92**	0.80	**0.86**	0.86
SD	**3.06**	4.12	**10.06**	17.95	**6.75**	16.80	SD	**0.88**	0.68	**0.95**	0.93	**0.97**	0.95

Table 3.4: *Intra* (highlighted in bold) and *inter*-activity (values outside the diagonal) correlations between the measured marker relative displacements and predictions from the 'best-matching' models.

	Specimen 1			***Specimen 2***			***Specimen 3***		
	Exp. GT	Exp. DKB	Exp. SD	Exp. GT	Exp. DKB	Exp. SD	Exp. GT	Exp. DKB	Exp. SD
Model GT *r*	**0.94**	0.40	0.23	**0.96**	0.63	0.08	**0.91**	0.08	0.17
Model DKB *r*	0.71	**0.88**	0.14	0.42	**0.95**	0.65	0.30	**0.84**	0.14
Model SD *r*	0.24	0.04	**0.96**	0.01	0.64	**0.88**	0.19	-0.02	**0.93**

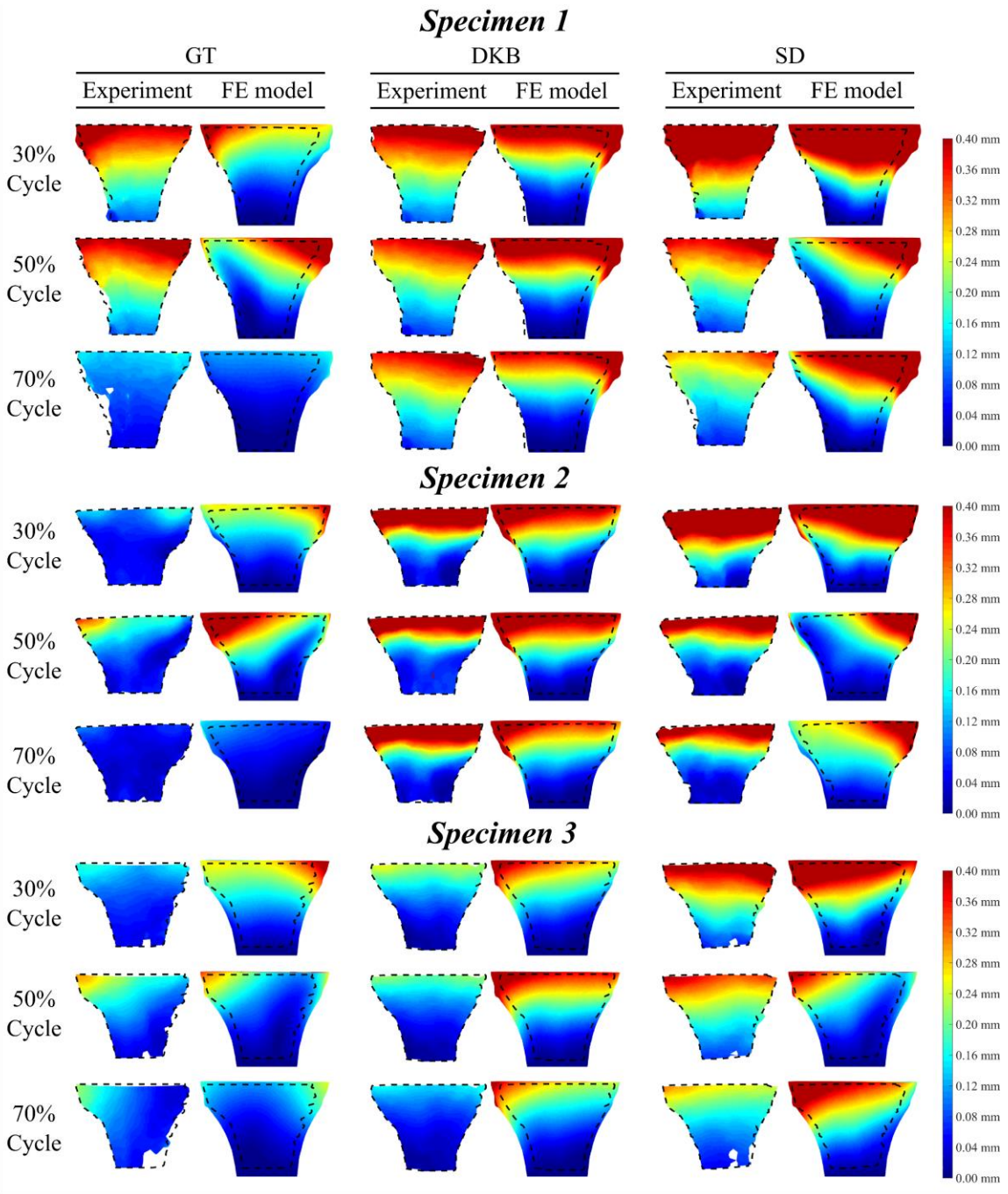

Figure 3.7: Full-field measured and predicted surface displacements were compared at 30%, 50%, and 70% of the activity cycles.

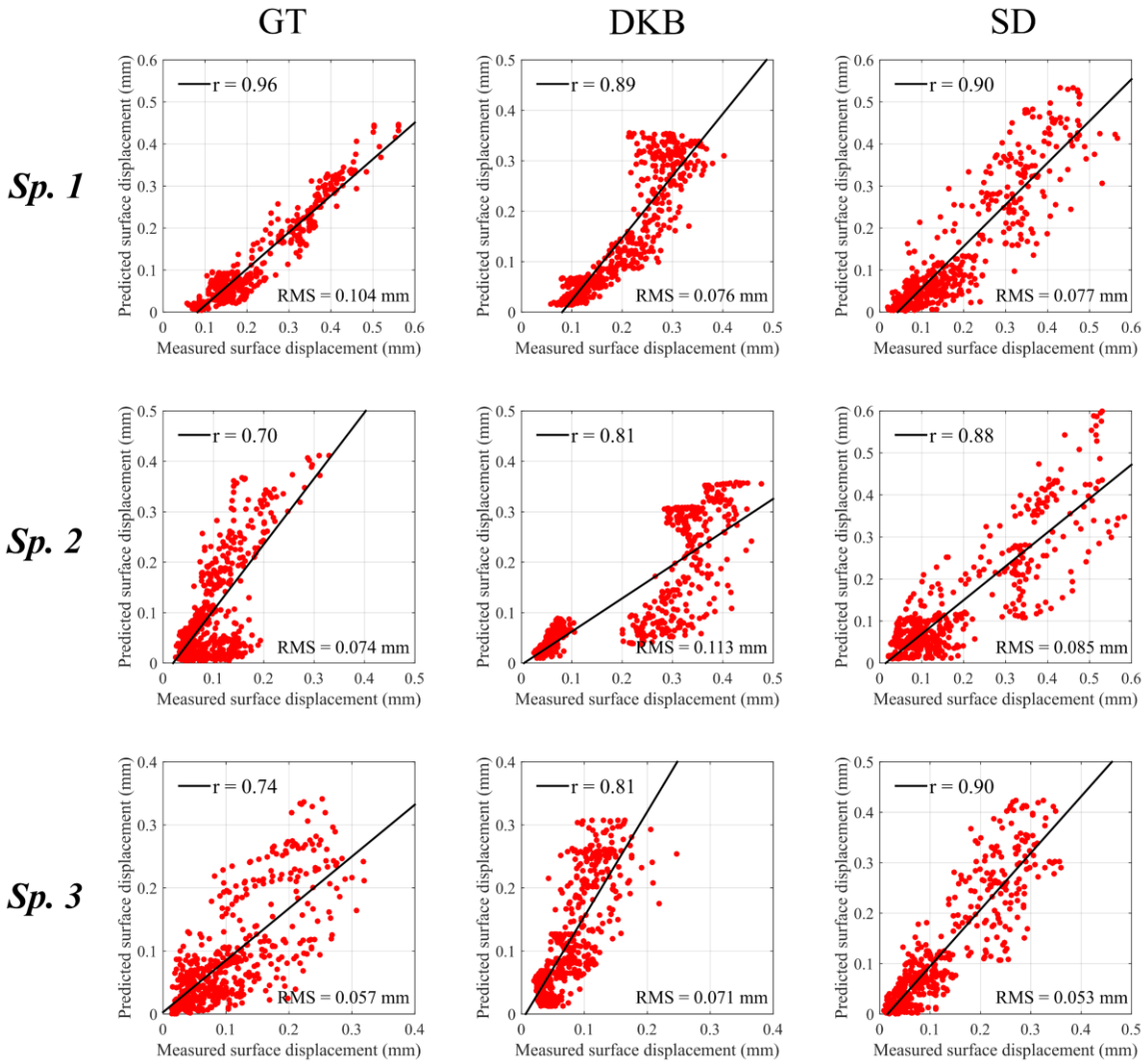

Figure 3.8: Pearson's correlations and average RMS differences between measured and predicted surface displacements from five sub-regions are shown.

Table 3.5: *Intra* (bold) and *inter*-activity correlations between the measured surface displacements and predictions from the baseline models.

	Specimen 1			***Specimen 2***			***Specimen 3***		
	Exp. GT	Exp. DKB	Exp. SD	Exp. GT	Exp. DKB	Exp. SD	Exp. GT	Exp. DKB	Exp. SD
Model GT *r*	**0.96**	0.62	-0.06	**0.70**	0.51	0.38	**0.74**	0.61	0.25
Model DKB *r*	0.56	**0.89**	0.85	0.15	**0.81**	0.88	0.63	**0.81**	0.80
Model SD *r*	0.35	0.79	**0.90**	-0.05	0.58	**0.88**	0.42	0.65	**0.90**

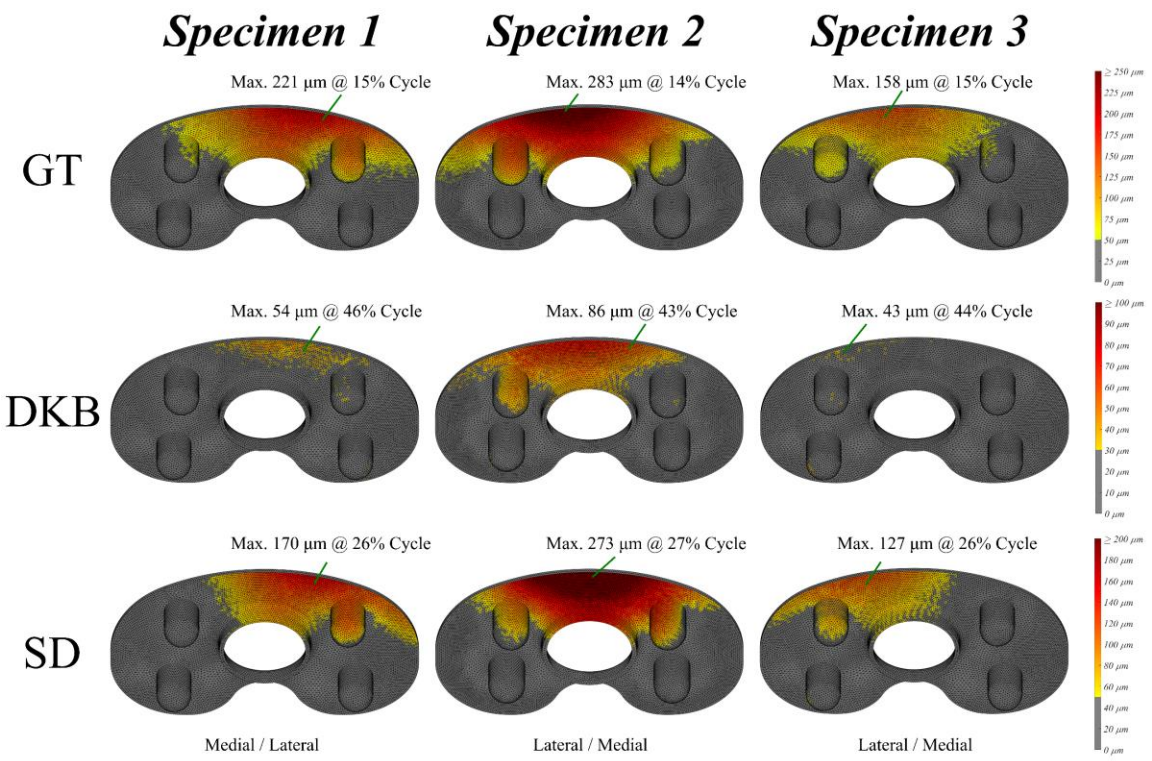

Figure 3.9: Predicted interface micromotions at the frames having peak micromotion magnitudes. The color bar ranges were: gait activity (0~250 μm); deep knee bending activity (0~100 μm); stair descent activity (0~200 μm).

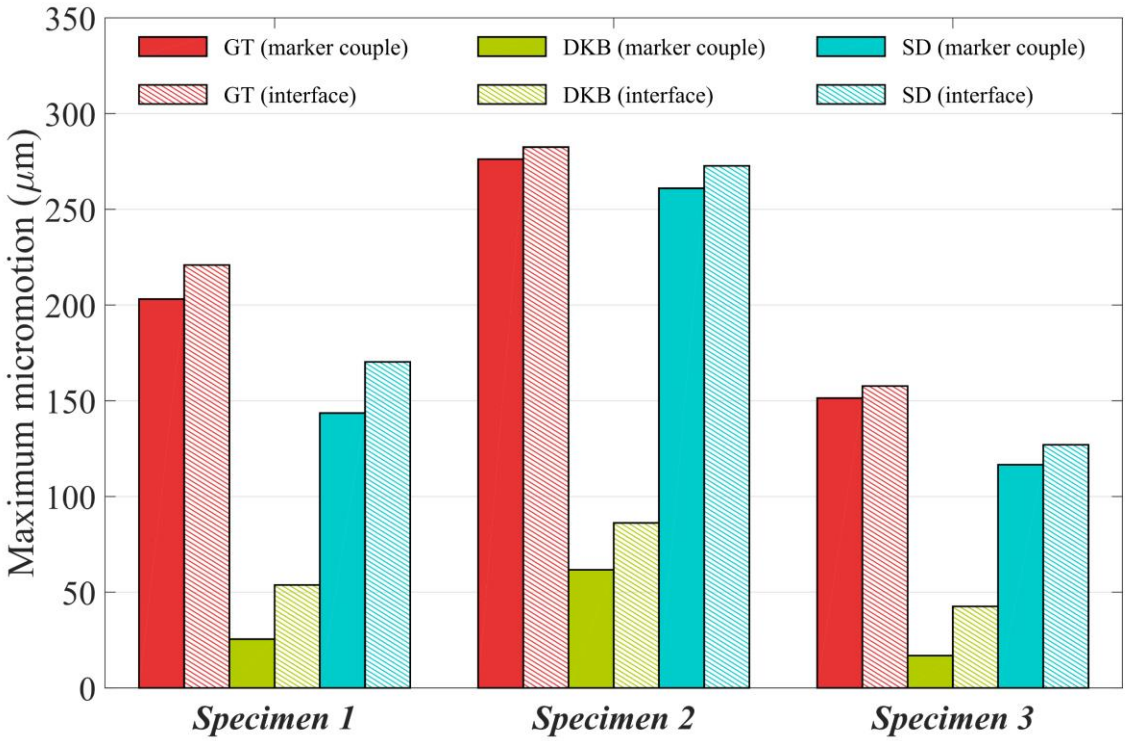

Figure 3.10: Comparisons between maximum marker relative displacements and the maximum interface micromotions.

Table 3.2: The maximum values of the interface micromotions (in μm) predicted from the baseline, upper-bound, and lower-bound models.

	Specimen 1			***Specimen 2***			***Specimen 3***		
	GT	DKB	SD	GT	DKB	SD	GT	DKB	SD
Baseline model	220.9	53.8	170.3	282.5	86.2	272.7	157.7	42.6	127.0
Upper-bound model	258.4	65.2	213.9	316.0	98.8	323.2	183.2	53.0	159.6
Lower-bound model	194.9	37.0	140.8	256.5	75.4	237.2	146.6	39.0	107.6

CHAPTER 4. IMPACT OF SURGICAL ALIGNMENT, TRAY MATERIAL, PCL CONDITION, AND PATIENT ANATOMY ON TIBIAL STRAINS AFTER TKA

4.1 Abstract

Bone remodeling after total knee arthroplasty is regulated by the changes in strain energy density (SED), however, the critical parameters influencing post-operative SED distributions are not fully understood. This study aimed to investigate the impact of surgical alignment, tray material properties, posterior cruciate ligament (PCL) balance, tray posterior slope, and patient anatomy on SED distributions in the proximal tibia. Finite element models of two tibiae (different anatomy) with configurations of two implant materials, two surgical alignments, two posterior slopes, and two PCL conditions were developed. The models were tested under the peak loading conditions during gait, deep knee bending, and stair descent. For each configuration, the contact forces and locations and soft-tissue loads of interest were taken into consideration. SED in the proximal tibia was predicted and the changes in strain distributions were compared for each of the factors studied. Tibial anatomy had the most impact on the proximal bone SED distributions, followed by PCL balancing, surgical alignment, and posterior slope. In addition, the thickness of the remaining cortical wall after implantation was also a significant consideration when evaluating tibial anatomy. The resulting SED changes for alignment, posterior slope, and PCL factors were mainly due to the differences in joint and soft-tissue

loading conditions. A lower modulus tray material did result in changes in the post-operative strain state, however, these were almost negligible compared to that seen for the other factors.

4.2 Introduction

Total knee arthroplasty (TKA) relieves pain and restores function in patients with advanced knee osteoarthritis (Leichtenberg et al., 2018) , and the future demand in knee arthroplasty is predicted to grow by 85%, to 1.26 million procedures by 2030 (Sloan et al., 2018). One of the most common complications and hence reason for revision is mechanical loosening (23.1% of all revised TKA) (Dalury et al., 2013). It is known that bone remodels in response to applied loads by changing its architecture (Wolff, 1893; Frost, 1992), and this bone remodeling process after TKA is regulated by the changes in strain energy density (SED) (Ruimerman et al., 2005). The recruitment of osteoclasts and osteoblasts is controlled by the SED-related signals sent through the osteocytic-canalicular network (Burger & Klein-Nulend, 1999). Insufficient stimuli as a result of stress shielding can promote bone resorption and potential for aseptic loosing of the implant. Hence, it is essential to identify the critical parameters influencing post-operative SED distributions.

In general, the strain state inside the tibia cannot be measured experimentally. Finite element methods have been previously used to evaluate factors affecting post-operative tibial strain states (Scott & Biant, 2012). Studies have investigated the impact of stem length, implant material and alignment, fixation method (cemented & cementless), and tray-bone fit with cadaveric or synthetic tibial models under pure body weight, single activity, or multi-activity static loading conditions (Completo et al., 2007; Innocenti et al.,

2009; Jia et al., 2017; Simpson et al., 2009; Zhang et al., 2016b). Testing loads have been typically applied uniformly on the surface of the polyethylene insert or tibial plateau, without additional soft-tissue loading on the tibia. Perillo-Marcone et al. (2007) showed that the stresses generated within the implanted tibia were dependent on the kinematics of the joint (e.g., contact locations), which are affected by the TKR design, surgical alignment, and the balance of the soft tissue. Also, a larger influence of the muscle loading on the strain distribution was unveiled by Duda et al. (1998), which was rarely considered in previous studies.

To our knowledge, none of the previous studies considered both femoral-insert contact (contact locations and force directions) and soft tissue loading conditions (tendon and ligament forces and directions) when investigating bone strains. The objective of the current study is to investigate the influence of surgical alignment, tray material properties, posterior cruciate ligament (PCL) balance, tray posterior slope, and patient anatomy on proximal tibial strain energy density while considering physiological femoral-insert contact conditions and patellar and PCL ligament forces. We virtually implanted two distinct tibiae using different alignment methods, tray posterior slopes, and tray materials. Computational models were tested under peak compressive stance phase gait (GT), deep knee bending (DKB), and stair descent (SD) loading conditions which were individually determined for each model configuration. A nominal and a tight PCL condition were also taken into consideration. The strain energy density in the proximal tibia was predicted for those models and compared for each of the factors studied, with a focus on the change in strain distribution for each factor.

4.3 Methods

4.3.1 Finite element models of the tibia

Three-dimensional geometries of two intact left tibiae, one typical and one with larger posterior overhang (subsequently indicated as 'shelf' tibia) (Figure 4.1b) were manually segmented using ScanIP (Simpleware, Exeter, UK) from computed tomography (CT) scans. The images were in DICOM format with a 0.6-mm slice thickness and a maximum 0.87-mm pixel spacing. The studied tibiae were similar in size to ensure the same tray size fit. However, the shelf tibia selected had the most extreme posterior overhang variation out of a database of 170 specimens. The cortical wall thickness of the normal tibia was slightly larger than the shelf tibia with varying magnitude along its length (less than 1 mm with differences increasing inferiorly). Each tibial geometry was constructed into a solid model and was virtually implanted with a cemented prosthesis (size 5, fixed-bearing, cruciate-retaining, Attune®, DePuy Synthes, Warsaw, IN) using mechanical and anatomic alignment techniques with both 0 and 5-degree posterior slopes in HyperMesh (Altair Engineering Inc., Troy, Michigan) (Figure 4.1c). However, it should be understood by the reader that, according to the manufacturer's surgical technique, a posterior slope of 0° is outside the range of 5~7° recommended for the cruciate retaining version of Attune to provide proper PCL tension. It should be noted that a size 5 tray was always the best-fit or suitable in each resection scenario with regard to the surgical approach. The surgical alignment techniques used in this study were: 3° femoral external rotation, 0° varus slope, and 0° hip-knee-ankle (HKA) angle for mechanical alignment; 0° femoral external rotation, 5° varus slope, and 3° HKA angle for anatomic alignment. The technique for placement of the tray (determining the anterior/posterior location and internal/external rotation relative

to the tibia) was done using a virtual implantation algorithm and unchanged across all resection scenarios. A 2-mm-thick cement layer was created between the tibial tray and bone (Ko et al., 2017). The proximal 150-mm tibial geometry was represented in the finite element simulations. The polyethylene insert, tibial tray, cement layer, and the bone were meshed with 1-mm, linear tetrahedral elements, which were identified from a mesh convergence study. All components were modeled as linearly elastic and with different material properties (Table 4.1). Two common metal materials for the tibia tray, cobalt-chrome (CoCrMo) and titanium alloy (Ti6Al4V) were considered. Heterogeneous material properties of the tibiae were calculated from the CT Hounsfield units and were assigned to each tibia element using an in-house mapping software. Previously established relationships were used for calculating the apparent bone density and elastic modulus for the individual elements (Anderson et al., 1992; Kaneko et al., 2004). Around 400 material properties (1 property per 4 mg/cm^3 bone apparent density) were used for modeling the tibiae based on a prior convergence study. The bone-cement and cement-tray interfaces were assumed to be fully bonded. The interface between the polyethylene insert and metal tray was modeled as a contact pair with a friction coefficient of 0.04. The distal ends of the tibial models were fully fixed.

The effect of the PCL forces on the tibial strain state was assessed. Patellar and PCL ligaments were divided into sub-bundles and modeled as connector elements, using three bundles to represent the patella tendon (lateral, central, and medial bundles) and two for the PCL (anterolateral and posteromedial bundles). The attachment sites of these ligament bundles on the tibia were recon- structed based on the anatomy of each tibia (Figure 4.1d).

Additional models were built for the shelf tibia (initially has lower mean material properties) with material properties matched to the normal tibia to best isolate the impact of tibial geometry on bone strains. This was achieved by modifying the apparent density range of the shelf tibia to be the same as the normal tibia and recalculating Young's moduli based on the new bone apparent density for each element.

4.3.2 External boundary conditions

The loading and boundary conditions applied to the models were determined using a previously developed finite element lower limb model (Figure 4.1a) (Fitzpatrick et al., 2012). The function of this simulation was to assess implant mechanics during simulated activities under multi-factorial sources of variability, including soft tissue, surgical technique, and alignment variability. The lower limb model includes a vertical load applied at the hip, quadriceps and hamstring loading, M-L load at the ankle, an I-E torque about the long axis of the tibia, and A-P motion of the pelvis. In the simulation, proportional-integral-derivative (PID) control is used with the quadriceps actuator to achieve a desired flexion profile. The external loading conditions were developed using data from the orthoload telemetric joint loading measurements (Kutzner et al., 2010). Using the geometry of the telemetric implant, the external loading conditions were derived to best reproduce the average measured, six-degrees-of-freedom joint loading. Subsequently, implant design and alignments have been studied with these consistent external boundary conditions (see reference 217 for complete description).

The implant design used in this study was incorporated into the lower limb model to simulate GT, DKB, and SD activities in Abaqus/Explicit (SIMULIA, Providence, RI). The

initial strains of the PCL bundles (nominal PCL condition) were calibrated by matching the elongations and tensions of the PCL bundles, and medial and lateral femoral-insert AP translations with literature (Escamilla et al., 2012; Hensler et al., 2012; Pfitzner et al., 2017). A tight PCL condition was then defined by increasing the initial strain of each bundle by 5%, which made the resulting PCL tension and femoral-insert AP translation still within reported ranges but approaching the boundary. Subsequently, eight unique configurations (two surgical alignments, two tray posterior slopes, and two PCL conditions) were incorporated into the lower limb model to simulate the aforementioned activities. Peak femoral-insert contact forces and locations and corresponding ligament force and directions were extracted from the lower limb model and applied to the models for bone strain analysis. The variables of tray material and tibial anatomy were not included in the lower limb model since these variables had negligible impact on the target outputs (contact forces and locations; ligament forces and directions). It should be noted that for each activity, the peak loads always occurred at the same frame no matter which alignment, tray posterior slope, and PCL conditions were used.

4.3.3 Analysis

In total, 144 finite element simulations (two tibiae, two tray materials, two surgical alignments, two posterior slopes, two PCL conditions, three activities, and additional models for the shelf tibia) were run in Abaqus/Standard.

The SED in the proximal 50-mm of the tibia was predicted for each model configuration. The proximal tibia was subdivided into four regions-of-interest (ROI): medial-proximal (MP), lateral- proximal (LP), medial-distal (MD), and lateral-distal (LD)

(Figure 4.3) (Navacchia, Sintini, et al., 2018). For each activity, the changes in SED distributions were compared for each of the factors studied. For example, when studying the impact of alignment technique during DKB activity, all the models with mechanical alignment (24 models) were compared with their counterparts with anatomic alignment (24 models) while all other factors were the same. The total strain energy in each ROI was calculated and normalized with respect to tibial regional volumes (which were slightly different due to the variations of the resection plane when introducing different surgical alignments and tray posterior slopes), then compared between those comparative models. The impact of a factor was then calculated by averaging the percent changes in the strain states of the comparison pairs (Figure 4.4). The relationship between the factors studied and the SED response was evaluated by using the multi-factor ANOVA (analysis of variance) statistical method. The P-value and contribution of each factor were reported in Table 4.3. The contribution was calculated as the percentage that each source contributes to the total sequential sums of squares (Seq SS). In this study, Seq SS quantifies the amount of variation in SED response that is explained by each term. Thus, the contribution can be used as an indicator which evaluates the weight of the impact on SED variations for each factor. It should be noted that the sequential SS and the adjusted SS were the same since the design matrix in this study is orthogonal. Thus, the order of the factors entered into the regression model has no impact on the ANOVA results.

In addition to the absolute strain predictions, comparison plots of the SED difference were created to better understand the changes in distributions inside the proximal tibia. For each factor studied, the SED of each tibial element was compared with the closest element in the counterpart model. Nine tibial sections parallel to the frontal plane, from anterior to

posterior, were made to visualize the SED changes inside the tibia (Figure 4.5). To best understand the impact of tibial geometry, representative plots of the absolute SED distributions inside the bone were made for the normal and shelf tibia (Figure 4.6).

4.4 Results

4.4.1 Convergence study

For mesh convergence, tibial elements were analyzed with 1.5, 1.0, and 0.75-mm element edge lengths. For defining material properties of the tibiae, 100, 200, 300, and 400 material properties were evaluated. The differences between the predicted SED in the proximal tibia when using 1.0 and 0.75-mm mesh sizes were less than 5%, and hence 1.0 mm meshes were used for the analyses presented. The SED differences between using 10 0 and 400 material cards were less than 1.5%.

4.4.2 Lower limb simulations

The inputs (femoral-insert and ligament forces and locations) to individual bone strain models were derived from the lower limb models and shown in Figure 4.2 & Table 4.2. For GT and SD activities, the PCL remained slack at the peak loading frame even if the PCL was pre-tightened. Thus, the two PCL conditions used in this study will not affect bone strain for these activities.

4.4.3 Relative changes in strain distribution

The sensitivity of SED in each tibial region to each of the five factors was determined (Figure 4.4). The average changes in SED (1.1%, 2.6%, 1.1%) (GT, DKB, and SD,

respectively) over all the regions associated with the change in tray material were much smaller than that seen with the changes in PCL balance (N/A, 25.0%, N/A) (GT, DKB, and SD), surgical alignment (23.0%, 15.3%, 24.4%), posterior slope (11.3%, 18.7%, 8.7%), and tibial anatomy (24.0%, 18.0%, 22.1%). PCL balance did not have an impact for GT and SD cases since the PCL bundles were slack at the peak tibiofemoral compressive loading frames for those two activities. Tibial anatomy had the largest impact on proximal bone SED distributions, followed by PCL balancing, surgical alignment, tray posterior slope, and material (Table 4.3). Representative contour maps of the SED changes within the tibia are shown in Figure 4.5. The contoured, comparative SED results reveal where the strain differences occur with change in each factor.

The tibial geometry had the largest impact on the strain states although the bone volume and material differences between tibiae were considered (by comparing normal tibia with shelf tibia models which have the same mean material properties). When comparing the shelf tibia with the normal tibia, SED decreased mostly at the distal regions (-34.2% for GT; -26.8% for DKB; -29.3% for SD), whereas the changes in proximal regions were relatively smaller (13.8% for GT; 9.1% for DKB; 14.8% for SD) (Figure 4.4).

The initial PCL tension influenced the strain distributions in the proximal tibia significantly during DKB activity, a 5% tightened PCL resulted in increased SED distributions over all the regions (+20.1% in MP; +32.9% in LP; +32.7% in MD; +14.1% in LD) (Figure 4.5b).

Surgical alignment (indicated frontal plane alignment and HKA angle here) of the tray had a considerable effect on the strain states. For GT and SD activities, less SED was calculated in the medial regions (both MP and MD) (-26.0% for GT; -24.5% for SD) for

the mechanical alignment case compared anatomic alignment case, whereas more SED was observed in the lateral regions (+14.9% for GT; +21.3% for SD) (Figure 4.4 and 4.5c). For DKB activity, the SED de- creased over all regions (-17.5% in MP; -10.9% in LP; -12.2% in MD; -10.8% in LD) (Figure 4.4 and 4.5d).

In all the activities, we found that the SED increased posteriorly and decreased anteriorly when introducing a tray posterior slope (Figure 4.5e). For DKB activity specifically, the SED decreased over all the regions when introducing a 5°* posterior slope (-13.9% in MP; -27.5% in LP; -23.2% in MD; -10.1% in LD) (Figure 4.4).

The tray material composition had a much smaller influence compared to the other factors (Figure 4.4). The SED slightly increased in the proximal regions (+1.4% for GT; +3.4% for DKB; +1.2% for SD) under the baseplate and decreased under the stem when using Ti6Al4V instead of CoCrMo (Figure 4.5f).

4.4.4 Absolute SED distributions (Normal vs. shelf tibia)

Substantial differences in SED distributions were seen posteriorly (Figure 4.6, highlighted by black circles) between the normal and shelf tibia. For the normal tibia, the SED was continuously distributed along the bony wall posterior to the tray stem (Figure 4.6d) (minimum wall thickness was 4.7-mm, excluding cement layer), whereas the SED had interruption at the same region for the shelf tibia (Figure 4.6e) (minimum wall thickness was 2.2-mm). The SED interruption was improved when introducing a 5°* tibial posterior slope to the shelf tibia (Figure 4.6f) (minimum wall thickness 3.6-mm).

**NOTE: A posterior slope of 5~7° is recommended in the manufacturer's surgical technique for the cruciate retaining version of Attune to provide proper PCL tension.*

4.5 Discussion

Bone remodeling after total knee arthroplasty is regulated by the changes in strain energy density (Ruimerman et al., 2005). In this study, we investigated post-operative bone strains during gait, stair descent, and deep knee bending activities. Specifically, we assessed the impact of surgical alignment, tray material properties, posterior cruciate ligament balance, tray posterior slope, and patient anatomy (tibial posterior overhang) on strain energy density distributions in the proximal tibia. The variations in femoral-insert contact locations and contact force directions due to surgical alignment, tray posterior slope, and PCL balancing were considered. We also included patellar tendon and PCL forces when calculating SED distributions.

The impact of tibial geometry on SED was substantial. To enable better comparisons, these two tibiae were selected due to their similar size and were implanted with the same-size prosthesis. The SED changes in distal regions were larger than those changes in proximal regions. The small differences proximally were mainly due to the changes in ligament force locations (different ligament attachment sites for each tibia). In the distal ROIs, the shelf tibia had less remaining bone stock posteriorly, which modified load transfer and minimized SED compared to the normal tibia. In addition, the shelf tibia showed interrupted SED distribution with no posterior slope (Figure 4.6e) whereas the normal tibia had continuous SED distribution, indicative of potential bone loss in that region. Introducing a 5° posterior slope increases the posterior wall thickness (Figure 4.6f) with this anatomy/implant combination and should be chosen to maximize fixation, as well as staying within the manufacturer's recommended surgical technique.

It is useful to examine the mechanisms that create changes in SED for PCL balance, surgical alignment, and posterior slope factors. A five percent increase in PCL tightness increased PCL forces by 84% during DKB activity, which also restricted the femur sliding anteriorly with respect to the tibia (Figure 4.2c). The total peak joint loads were increased by an average of 168N (7.9%). The increase in SED in all the regions during DKB activity was mainly caused by these increased femoral-insert contact forces. Alignment changed the medial and lateral contact force distribution significantly, but the total joint contact forces were fairly consistent. During GT and SD, peak medial contact forces decreased by 11.4%, and peak lateral contact forces increased by 11.8% when selecting mechanical instead of anatomic alignment. This led to the SED decrease in the medial and increase in the lateral ROIs. When a 5° posterior slope was introduced in GT and SD activities, the total joint contact forces (<2.0%) and the medial-lateral distributions (<1.5%) were nearly unchanged. However, the medial-lateral contact locations shifted about 2.2 mm posteriorly (Figure 4.2b). The change in SED (increased posteriorly and decreased anteriorly) was mostly due to the changes in the joint contact locations and force directions. For the DKB activity, the total femoral-insert contact forces decreased by an average of 5.5% (144N), which resulted in decreased SED over all regions. The resulting strain changes for these three factors were mainly due to these changes in the joint contact and soft tissue loads. It should also be noted that ranking of the most influential factors is clearly dependent on the variability chosen for each.

It can be concluded that the SED in the proximal tibia would increase only when the joint contact load increased (in this study, only achieved from a tighter PCL). According to the manufacturer, a tight PCL should be avoided to enable proper implant kinematics,

however, minimizing the reduction in SED may be achieved through other surgical parameters. Previous studies demonstrated that medial tibial bone loss is most common (J. R. Martin et al., 2017; Yoon et al., 2018). A recent publication also reported that the medial region generally showed a larger decrease in SED relative to the lateral region after TKA (Anjis et al., 2020), which indicated that the bone loss would most likely occur at the proximal-medial tibia under the baseplate. Thus, an anatomic alignment may be preferred, as it would result in considerably increased SED in the medial region compared with mechanical alignment. The tray posterior slope influences the SED anterior-posterior distribution only moderately, however, this is a key factor that determines the minimum thickness of the remaining posterior wall after TKA. These findings have clinical implications. When deciding the best approach for a specific patient, we recommend choosing the tray alignment configuration based on a patient-specific evaluation of geometry and bone quality. For example, an anatomic alignment in the frontal plane is likely preferred to minimize stress shielding and the change in strain from the native state on the medial side. We also recommend introducing a tray posterior slope according to the patient's tibial anatomy to keep the posterior wall thickness, avoid stem-cortex contact, and best mimic tibial strain. A slightly tighter PCL might be desired if the overall bone quality is poor, as this would increase the compressive contact loading, which results in increased SED across the proximal tibia.

It has been previously discussed that the tray material composition causes stress shielding of periprosthetic bones (J. R. Martin et al., 2017). In this study, we found that the impact of tray material properties on post-operative SED distribution was negligible, especially when compared with changes found for typical patient and surgical variables.

An average of 1.6% SED difference was found in the proximal tibia when comparing using CoCrMo and Ti6Al4V as the tray material. This finding is in line with a previous study that showed no differences in stress shielding when using titanium and cobalt-chrome tibial prostheses (Completo et al., 2009).

This study has limitations to note. Although we addressed the impact of anatomy of two tibial types, only two tibiae were included in this study. Matching the material properties of the two tibiae helped to understand the relative impact of material and geometry, but future studies should focus on a more comprehensive distribution of patient anatomy. It is clear that not only the tibial posterior overhang and densities vary between subjects, but also the bone geometry and material distribution, patient weight, and other knee-related anatomical features (such as Q-angle, ligament attachment sites, and hip-knee-ankle angle) are different. The complex combination of these anatomical factors would alter the ligament forces, contact conditions, tibial moments, etc., and finally SED distributions. However, we believe that the primary im- pacts and trends of the factors on SED distributions will be still valid under those situations (for example, a tighter PCL would increase the overall SED, and an anatomic alignment would result in more SED in the medial region comparing with a mechanical alignment, etc.). The cemented implant was assumed here to be perfectly bonded at the tray-bone interface, which is a simplification of the variation likely seen in vivo. Only one implant design (cemented, fixed-bearing, cruciate-retaining) was tested in this work. The loading patterns and strain distributions may be different for other implants, especially with different tray designs. Finally, the bone strain analysis performed in this study cannot be reproduced and examined experimentally. However, in the study immediately preceding the current,

prediction of tibial surface displacement was validated experimentally with digital image correlation and a known, physiological loading condition for several tibial specimens (H. Yang et al., 2020). Models were developed using the same process for representing bony mechanics. In that study, three cadaveric tibial specimens were physically tested under GT, DKB, and SD loads, while digital image correlation (DIC) was used to measure tibial surface displacement. Corresponding computational models were developed using the same methods shown here. The Root-Mean-Square differences and Pearson's correlations between experimentally measured surface displacements and predictions were 78.9 μm and 0.84 specimens (H. Yang et al., 2020).

In summary, the potential differences in post-operative proximal tibial SED distributions for five typical TKA parameters were evaluated. Tibial anatomy was found to have the largest impact on post-operative bone strains. The impact of PCL balancing, surgical alignment, and tray posterior slope were considerable. The SED changes for these three factors were mainly due to the changes in loading conditions. Among those, PCL balancing affects the overall strain energy magnitude, whereas the alignment and posterior slope primarily influence the medial-lateral and anterior-posterior SED distributions, respectively. The impact of tray material modification was much smaller than the aforementioned factors. The results indicated that maximizing post-operative fixation is possible using optimized surgical parameters in the frontal plane as well as posterior slope to address patient anatomy.

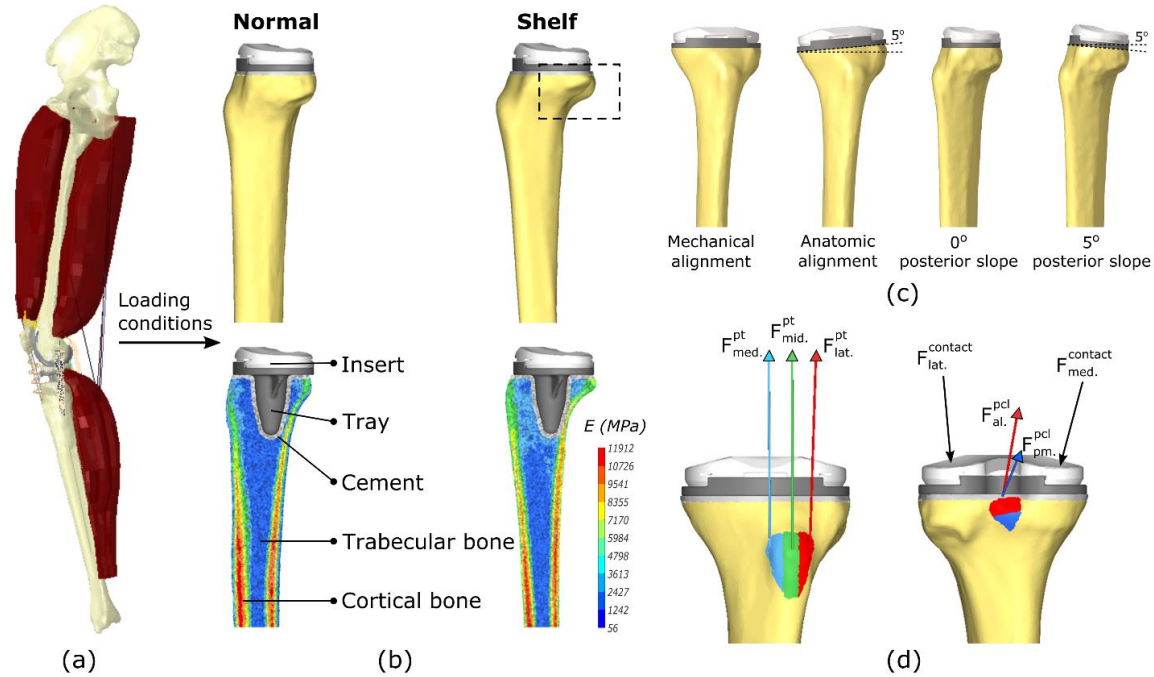

Figure 4.11: Model set up. (a) Lower limb finite element model for estimation of joint and soft tissue loads applied to deformable tibial models. (b) Young's modulus distributions in the cortical and trabecular tibia bone for the normal and shelf tibiae. (c) The tibial models with different alignment and tray posterior slopes. (d) Patellar tendon, PCL sub-bundles, and their attachment sites. External boundary conditions, including joint contact forces and ligament forces. (F_{med}^{pt}= medial patellar tendon bundle force; $F_{al.}^{pcl}$= anterolateral PCL bundle force; $F_{med}^{contact}$= medial femoral-insert contact force; similar for the rest).

Table 4.1: Material properties used in the computational models.

Component/Material	Density (g/cm^3)	Elastic moduli (MPa)	Poisson's ratio
Insert - UHMWPE	0.94	691	0.45
Tray - CoCrMo	8.50	210,000	0.30
Tray - Ti6Al4V	4.50	105,000	0.27
Cement - PMMA	2.00	2551	0.40
Cortical bone	$1 \leq \rho \leq 1.9$*	$3290 \leq E \leq 11912$	0.30
Trabecular bone	$0.1 \leq \rho < 1$	$56 \leq E < 3290$	0.30

*1.9g/cm3 was the maximum density of the tibiae used in this study. The corresponding elastic modulus was 11912 MPa. The values were in range with the human tibial density and elastic properties reported in literature (Rho et al., 1996).

Table 4.2: External boundary conditions derived and applied to the computational models (al. bundle = anterolateral bundle; pm. bundle = posteromedial bundle).

Peak loading conditions during gait stance phase (N)

Component	0º posterior slope Mechanical alignment	0º posterior slope Anatomic alignment	5º posterior slope Mechanical alignment	5º posterior slope Anatomic alignment
Med. Contact	1334.9	1603.6	1284.5	1566.8
Lat. Contact	1084.5	797.5	1086.2	793.4
Patellar tendon lat.	628.4	662.7	598.2	626.1
Patellar tendon mid.	745.1	758.6	786.2	799.1
Patellar tendon med.	495.0	435.1	434.1	379.2
PCL al. bundle	slack	slack	slack	slack
PCL pm. bundle	slack	slack	slack	slack

Peak loading conditions during deep knee bending (N)

Component	0º posterior slope Mechanical alignment (Tight/Nominal PCL)	0º posterior slope Anatomic alignment (Tight/nominal PCL)	5º posterior slope Mechanical alignment (Tight/Nominal PCL)	5º posterior slope Anatomic alignment (Tight/Nominal PCL)
Med. Contact	461.6/394.5	112.8/161.2	442.7/425.0	242.5/297.0
Lat. Contact	1904.7/1796.7	2274.4/2055.0	1774.7/1632.4	2005.6/1782.5
Patellar tendon lat.	slack/slack	98.12/80.8	slack/slack	81.7/65.5
Patellar tendon mid.	1162.6/1142.8	1219.7/1203.7	1167.0/1146.3	1234.4/1224.6
Patellar tendon med.	581.2/654.1	333.0/422.1	558.5/632.4	338.9/414.6
PCL al. bundle	540.2/326.2	596.0/376.6	390.3/166.3	439.3/196.1
PCL pm. bundle	slack/slack	slack/slack	slack/slack	slack/slack

Peak loading conditions during stair descent (N)

Component	0º posterior slope Mechanical alignment	0º posterior slope Anatomic alignment	5º posterior slope Mechanical alignment	5º posterior slope Anatomic alignment
Med. Contact	1584.2	1962.0	1575.4	1955.6
Lat. Contact	1591.9	1212.4	1543.1	1162.1
Patellar tendon lat.	709.1	760.7	672.3	717.7
Patellar tendon mid.	915.7	944.3	948.5	973.3
Patellar tendon med.	741.1	649.0	680.4	600.0
PCL al. bundle	slack	slack	slack	slack
PCL pm. bundle	slack	slack	slack	slack

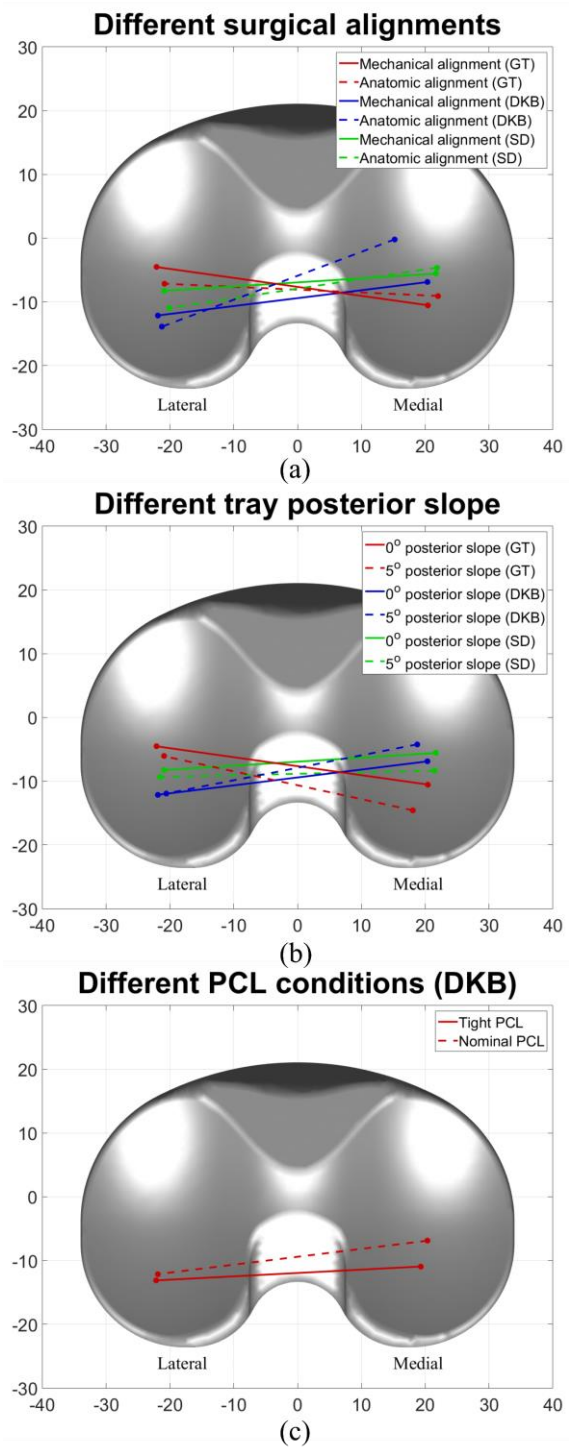

Figure 4.12: Femoral-insert contact locations at the peak loading frames under different surgical alignments, tray posterior slopes, and PCL balancing conditions. Results were derived from the lower limb model. *Note that for GT and SD, the PCL balancing conditions have no effect on femoral-insert contact since the PCL was slack during these two activities (c).

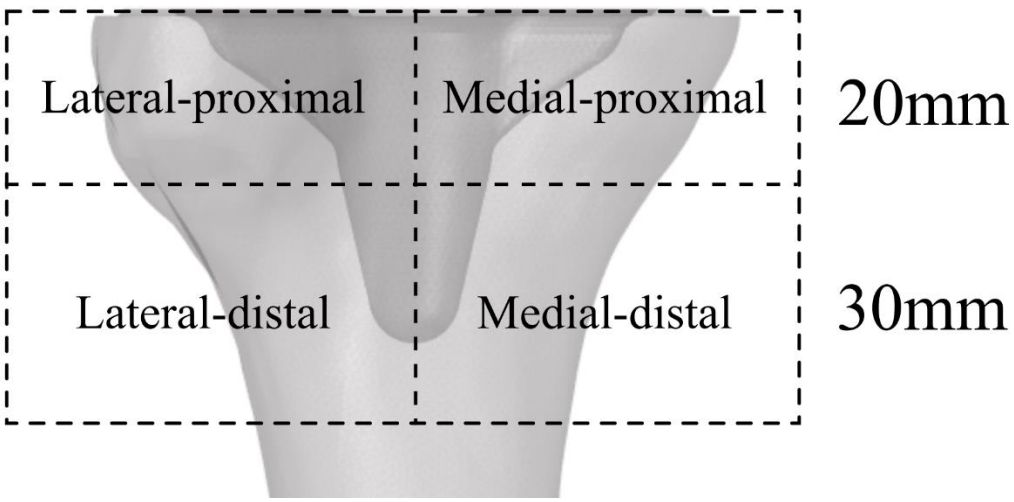

Figure 4.13: Region divisions of the proximal tibia.

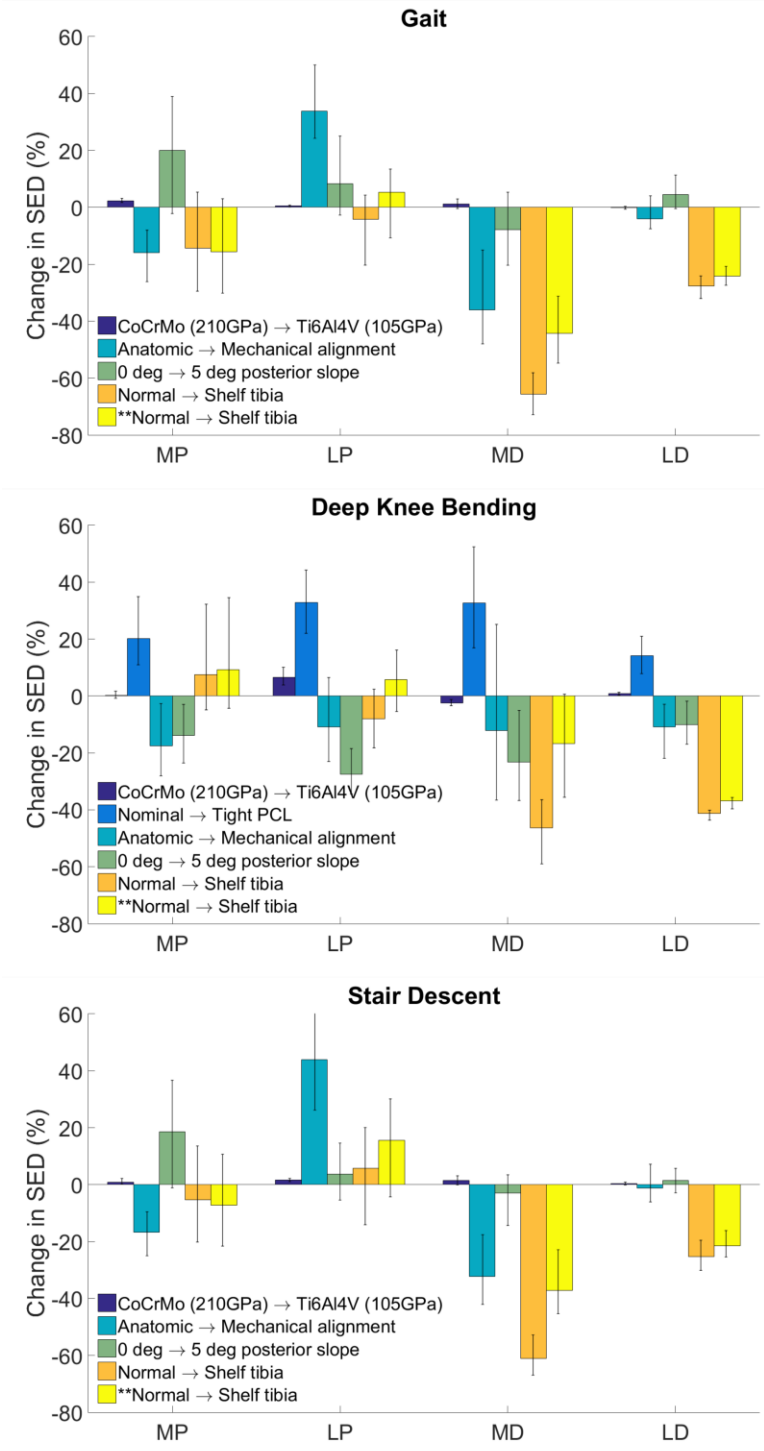

Figure 4.14: The overall change in SED for five comparison pairs: tray materials (Ti6Al4V and CoCrMo), PCL conditions (tight and nominal), surgical alignments (mechanical and anatomical), tray posterior slopes (0 degree and 5 degree), and tibial anatomy (shelf and normal). ** indicates that the same material properties were used for the normal and shelf tibiae and the results were normalized with respect to tibial regional volumes.

Table 4.3: P-value and contributions of each factor on changes in SED distributions (MP: medial-proximal; LP: lateral-proximal; MD: medial-distal; LD: lateral-distal).

		P-values				**Factor contributions**				
	Source	MP	LP	MD	LD	MP	LP	MD	LD	**Average**
GT	Surgical alignment	0.004	0.000	0.000	0.049	22.92%	81.13%	33.51%	1.16%	**34.68%**
	Posterior slope	0.002	0.022	0.058	0.004	29.34%	6.89%	1.69%	3.17%	**10.27%**
	Tray material	0.632	0.863	0.850	0.897	0.43%	0.03%	0.01%	0.00%	**0.12%**
	Tibia anatomy	0.002	0.284	0.000	0.000	28.04%	1.23%	60.60%	93.06%	**45.73%**
DKB	PCL balance	0.000	0.000	0.000	0.000	25.92%	35.41%	30.10%	7.00%	**24.61%**
	Surgical alignment	0.000	0.000	0.001	0.000	32.81%	8.13%	10.58%	5.70%	**14.31%**
	Posterior slope	0.000	0.000	0.000	0.000	19.35%	45.50%	27.52%	4.33%	**24.18%**
	Tray material	0.910	0.019	0.597	0.726	0.01%	1.82%	0.22%	0.02%	**0.52%**
	Tibia anatomy	0.003	0.033	0.001	0.000	6.35%	1.49%	11.83%	78.64%	**24.58%**
SD	Surgical alignment	0.001	0.000	0.000	0.922	36.86%	82.99%	38.81%	0.00%	**39.67%**
	Posterior slope	0.001	0.211	0.341	0.157	34.01%	1.04%	0.30%	0.73%	**9.02%**
	Tray material	0.848	0.593	0.746	0.781	0.07%	0.18%	0.03%	0.03%	**0.08%**
	Tibia anatomy	0.051	0.002	0.000	0.000	8.84%	9.31%	57.59%	95.76%	**42.88%**

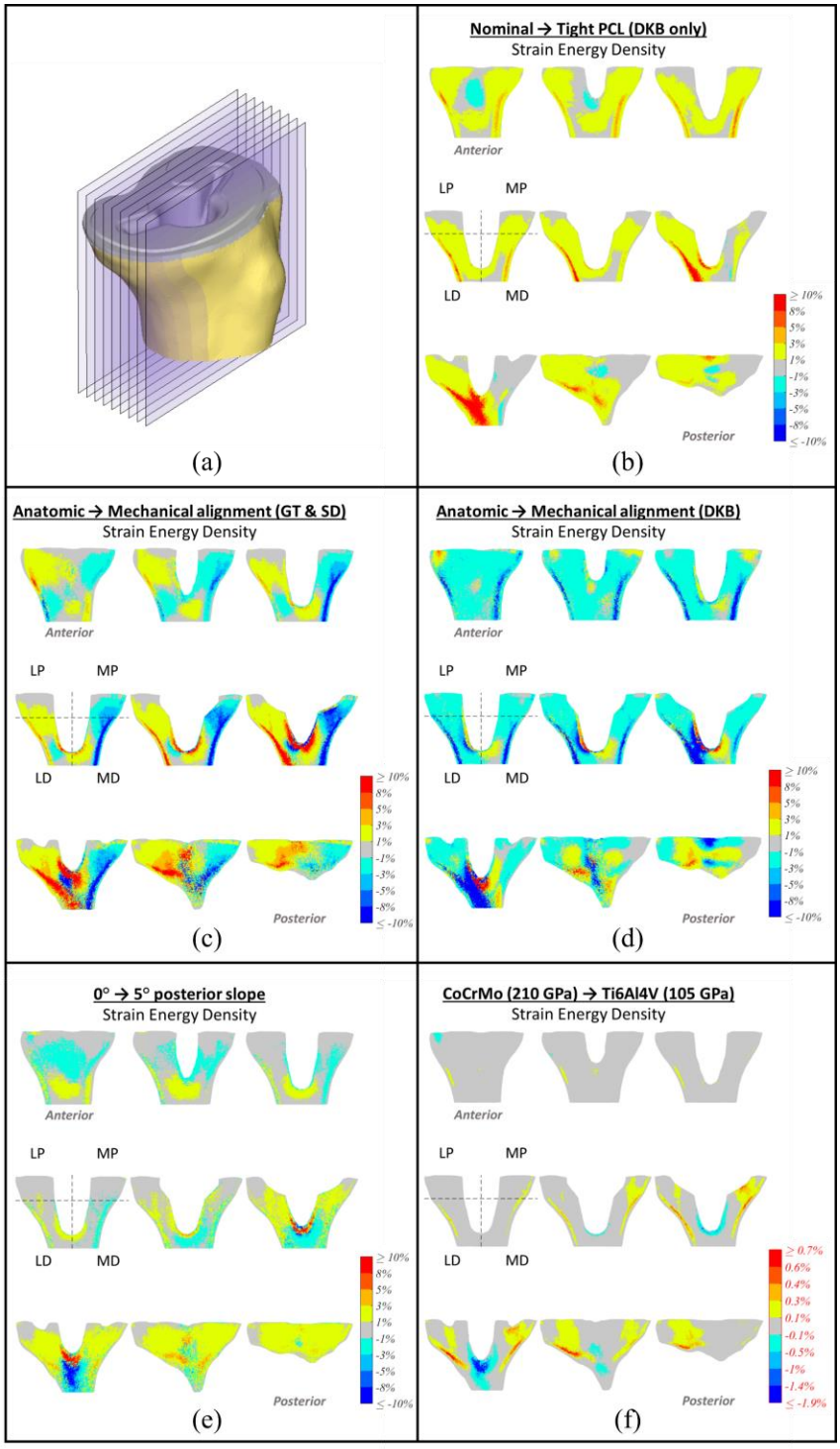

Figure 4.15: Contour maps of the changes in SED for each of the factors studied. (a) Cross-section divisions; (b) PCL balance (DKB only); (c) Surgical alignment (GT & SD); (d) Surgical alignment (DKB); (e) Tray posterior slope; (f) Tray materials. (The normal tibia was used for the plots; the shelf tibia has the similar results).

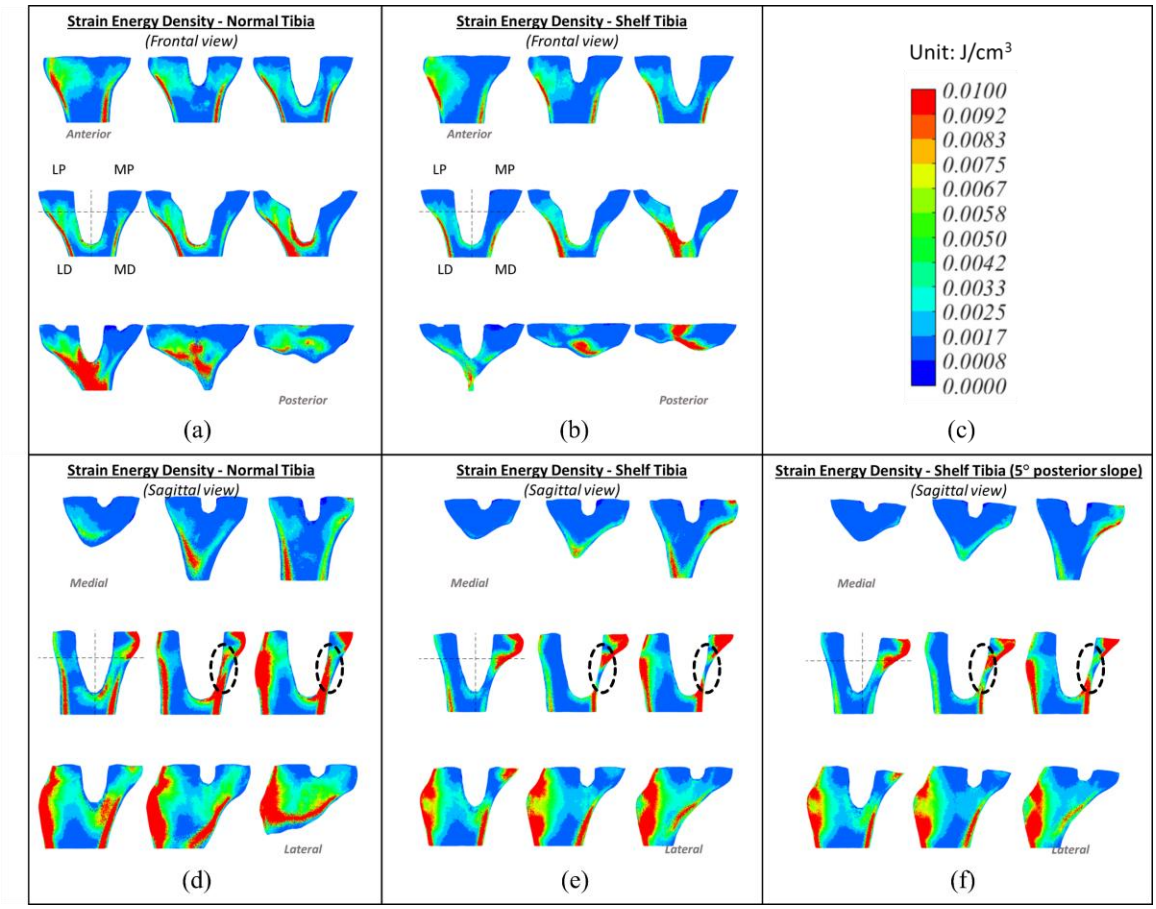

Figure 4.16: Contour maps of the bone SED distributions in the frontal and sagittal plane. (a & d) Normal tibia with 0° posterior slope; (b & e) Shelf tibia with 0° posterior slope; (f) Shelf tibia with 5° posterior slope; (*Representative configuration used for the plots: mechanical alignment, 0 or 5° posterior slope, nominal PCL condition, and CoCrMo tray material during deep knee bending activity*).

CHAPTER 5. IMPACT OF PATIENT, SURGICAL, AND IMPLANT DESIGN FACTORS ON PREDICTED TRAY-BONE INTERFACE MICROMOTIONS IN CEMENTLESS TOTAL KNEE ARTHROPLASTY

5.1 Abstract

Micromotion magnitudes exceeding 150 μm may prevent bone formations and limit fixation after cementless total knee arthroplasty (TKA). Many TKA factors influence the tray-bone interface micromotion but the sensitivities to the micromotion are unknown. Finite element models have been commonly used to estimate the interface micromotion that cannot be measured directly. In this study, we assessed the impacts of surgical (tray alignment, tibial coverage, resection surface preparation), patient (bone properties), and implant design (tray feature, surface friction, tibiofemoral kinematics) factors on the tray-bone interface micromotions during a series of activities of daily living. The changes in each factor were incorporated into three validated implant-bone models and the models were re-tested under gait, deep knee bending, and stair descent loads. Overall, peak micromotion was consistently found along the anterior edge of the tray for all activities. The average micromotion across the tray-bone cementless contact interface ranged from 9.3 to 111.4 μm. Maximizing tibial coverage above a right-sized tibial tray (an average of 12.3% additional area) had minimal impact on micromotion. For the design evaluated, the cone provided the majority of stability, as removal of all pegs only increased peak

micromotion by 13.3%. Micromotion was sensitive to small changes in tray alignment, as a 1mm anterior translation reduced the average micromotion by an average of 16.1%. Simulated tibial angular resection errors reduced the area for bone ingrowth up to 48.1%. The difference in tibial elastic properties from ±25% bone moduli resulted in up to 75.5% difference in the average micromotion. A more posterior tibiofemoral contact due to a 100N larger posterior force resulted in an average of 79.3% increment in the average micromotion. Overall, careful surgical technique, patient selection, and controlling kinematics through articular design all contribute meaningfully to minimizing micromotion in cementless TKA, with centralizing the load transfer to minimize the resulting moment at the anterior tray perimeter a consistent theme.

5.2 Introduction

As the number of younger and more active patients treated with total knee arthroplasty (TKA) continues to increase (Aggarwal et al., 2014; Aujla & Esler, 2017), implants are required to carry potentially greater dynamic activity cycles while maintaining long-term durability (Kim et al., 2016). Compared with cemented implants, current innovations in cementless tibial trays may offer a more long-lasting biological fixation (Dalury, 2016). The initial fixation of cementless tibial trays after TKA is crucial to bony ingrowth into the porous surface of the implants (Bragdon et al., 1996), as micromotion magnitudes exceeding 150 μm may prevent bone formation and lead to implant loosening (Engh et al., 1992; Pilliar et al., 1986). Many factors, such as surgical alignment, prosthesis design choices, and patient differences may affect the tray-bone micromotion. Therefore,

understanding the critical parameters impacting micromotion is required for optimal design, patient selection, and clinical performance.

In vitro experiments have been performed to investigate the impact of different TKA designs on tray-bone micromotion (Bhimji & Meneghini, 2014; Small et al., 2016). These studies measured the relative displacements between markers placed on the exposed surfaces of the tray and bone. Typically, the full tray-bone interface is not accessible and therefore surface micromotion has not been fully quantified experimentally (Malfroy Camine et al., 2016; Sukjamsri et al., 2015). Our prior study also indicated that these marker relative displacements did not numerically represent the actual micromotions at the contact surface (H. Yang et al., 2020). Therefore, finite element models have been commonly used in combination to estimate the interface micromotion and to investigate factors that are generally infeasible to study via experimental methods. Previous *in-silico* studies have primarily estimated the tray-bone micromotion under different loading conditions (Chong et al., 2010; M. Taylor et al., 2012), although a few also investigated the micromotion sensitivity of key factors such as implant alignment, design features, or individual differences. Sopher et al. investigated the impact of the implant design and positioning on the implant-bone micromotion in total ankle replacement (Sopher et al., 2017). Barker et al. virtually perturbed the circumferential flange of the tibial tray and predicted the influence on tray-bone shear micromotions (Barker et al., 2005). Hashemi and Shirazi-Adl (2000) compared the predicted micromotions between different fixation configurations of the tibial tray. The loading conditions applied in these TKA studies were typically simple vertical loads which do not account for the more complex physiological loading at the knee joint during daily activities.

Although a useful approach for investigating tray-bone interface micromotion, finite element models are limited by the necessary input and assumptions. Any poorly-characterized input would directly influence the accuracy of the resulting output (Sukjamsri et al., 2015). Thus, these computational models must be experimentally validated to draw reasonable conclusions. Our prior experimental-computational study has presented validation of predicted cementless tray-bone relative micromotions over a range of simulated activities of daily living for three implanted tibial bones (H. Yang et al., 2020). In addition, we evaluated the impact of alignment and tray-bone friction on the interface micromotion. Although these were important model sensitivities, they are by no means a comprehensive look at all of the potential factors that influence tray micromotion and hence resulting fixation. Several recent studies have reported that implant pegs have a considerable impact on tibial fixation (Barker et al., 2005; Hashemi & Shirazi-adl, 2000; Sopher et al., 2017). Additionally, maximizing tibial coverage is thought to improve fixation due to the more uniform distribution of the (Bertin, 2007; S. Martin et al., 2014; Wernecke et al., 2012). Plaskos et al. (2002) has reported that resection errors relative to the TKA cutting guide were in the range of 1.5~4.0° during bone preparation, which was foreseen to affect the tibial fixation. Differences in tibial elastic properties between samples with the same bone volume fraction have been reported to range up to 53% due to the different trabecular architectures (Ulrich et al., 1997). To our best knowledge, no one has systematically studied the impact of these common TKA factors on the tray-bone micromotion under physiological conditions.

Hence, this study aimed to investigate the influence of surgical (tray alignment, tibial coverage, resection surface preparation), patient (bone properties), and implant design (tray

features, surface friction, femur-tibial kinematics) factors on the tray-bone interface micromotions during a series of activities of daily living. Factors were studied using three previously-validated tibia-implant models during simulated gait (GT), deep knee bending (DKB), and stair descent (SD). The tray-bone interface micromotion for each model was predicted and compared with the original configuration, and critical parameters were identified.

5.3 Methods

5.3.1 Experimental setup and computational validation

Description of the experimental-computational framework used in this study can be found in Chapter 3 (section 3.3) but is also briefly summarized here. Three cadaveric tibiae were implanted with cementless tibial prostheses (best-fit size, rotating-platform, cruciate-retaining, ATTUNE®, Depuy Synthes, Warsaw, IN) by an experienced surgeon. Specimens were then cemented into custom fixtures and mounted in the 6-DoFs AMTI VIVO™ knee simulator (AMTO, Watertown, MA) to simulate gait (GT), deep knee bending (DKB), and stair descent (SD) activities. Experimental boundary conditions were derived from telemetric implant data and ASTM standard (Navacchia et al., 2016). Flexion/extension (FE) and internal/external rotation (IE) degrees of freedom (DoFs) were kinematically-driven while medial/lateral (ML), anterior/posterior (AP), superior/inferior (SI), and varus/valgus (VV) DoFs were load controlled. After bedding-in under cyclic compression for 200 cycles, 40 cycles of each activity were performed at a rate of 0.33Hz. Relative displacements between marker couples (placed at the anterior aspects of the tray and bone)

and tibial surface displacements were recorded with a digital image camera (DIC) system (Figure 5.1).

Corresponding computational models of the three specimens were developed in Abaqus/Standard (SIMULIA, Providence, RI) from CT scans with bone mineral density phantoms. Elastic moduli of the tibial elements were assigned based on Hounsfield units using established relationships (Anderson et al., 1992; Linde et al., 1991). Component alignment and marker locations were reconstructed from the experiments. The deformable implant-bone construct was virtually mounted into the VIVO simulator model (Fitzpatrick et al., 2016) and loaded via a rigid femoral component with the boundary conditions adopted from the VIVO experiment. The contact at the metal-poly and tray-bone interfaces were modeled with friction coefficients of 0.04 and 1.00, respectively. The marker and bone surface displacements were predicted and compared with experimental measurements (Figure 5.1). Prior convergence studies were completed during model development (including mesh size, the minimum number of simulated cycles required to reach a steady state, and the number of the material cards to characterize tibia properties). The average root-mean-square differences and correlations between measured marker relative displacements and predictions were 13.1 μm and 0.86, respectively.

5.3.2 Micromotion sensitivity research framework

The three validated cadaveric tibia-implant models were utilized for this follow-up study investigating the sensitivities of tray-bone interface micromotions to several common TKA factors. All boundary conditions (tray-bone alignment, activity loading, femoral-insert initial positions, etc.) were consistent with the prior study unless being perturbed

when studying specific factors. To differentiate with the perturbed models investigating micromotion sensitivities, the three original, validated models were indicated as 'baseline models' subsequently. For each factor studied, the change of the factor was incorporated into each baseline model and the newly generated model was re-tested during GT, DKB, and SD.

The parameters of each factor and corresponding model configurations are as below:

Surgical parameters

- Tray-bone alignment: For each baseline model, twenty-four models were developed by perturbing the initial tray-bone alignment (considering one perturbation at a time) ±0.5mm and ±1.0mm in translational DoFs (AP, ML, and SI) and ±0.5º and ±1.0º in rotational DoFs (FE, IE, and VV) (Figure 5.2a). After evaluating the impact of each parameter on the interface micromotion, an upper-bound model configuration was developed by considering all the parameters (a combination of 6 DoFs perturbations) which resulted in higher micromotions. Similarly, a lower-bound model configuration was developed.

  For each perturbation model, the changes in tibial contact surface modulus due to the re-alignments were investigated with consideration of the potential impact on micromotion. The tibial surface elements near the tray (distance from the tribal element center to the tray surface < 0.75mm) were isolated and the average elastic modulus of those elements was calculated (Figure 5.2a). For convenience, the applied activity loading conditions were consistent for each model since the perturbation was small. However, for verification purposes, we

also evaluated the changes in loading conditions due to the re-alignment by using a previously-validated lower limb model (Fitzpatrick et al., 2012). The maximum change in the femoral-insert contact forces was 0.60% which could be neglected.

- Tibial coverage: For each baseline model, the porous coating of the cementless tray was divided into four regions, anterolateral, anteromedial, posterolateral, and posteromedial (Figure 5.2b). The covered tibial area in each region was recorded. Four porous coating models were virtually created to achieve more coverage in each region (Figure 5.2b). Another coating model was created by enlarging the entire geometry (a combination of the previous four models), which had the same coverage area as using a two-size-upgraded tray. However, it should be noted that this was not completely equivalent to using a larger tray because the peg positions were unchanged. Thus, the impact of the tibial coverage was isolated.
- Tibial angular resection error: Each baseline tibial model was additionally resected with a 2^{o} medial, lateral, and posterior slope, respectively, to simulate an angular resection error during the tibial preparation. The slopes started from the center of the tray stem and the bottom of the pegs remained fully contacted with the tibia (a small portion of the peg surfaces was exposed, see Figure 5.2d). The scenario with an anterior slope resection error was not simulated since the anterior tibia is much more visible during the tibial preparation, so that the anterior tibia is more likely to be flat. The scenarios with resection errors resulting in more bone remaining (caused by the cutting blade deflecting

upward) were also not considered since the tray would still have enough supports at the edges, which should not be worse than the simulated cases.

Design parameters

- Tray-bone coefficient of friction: Based on test data from the manufacturer, the coefficient of friction was defined as 1.00 at the tray-bone interface for the baseline models. To study the impact of this factor, the coefficient of friction was perturbed from 0.6 to 1.4 (with a 0.2 increment) to cover a wide range of potential variability.
- Tray pegs: For each baseline model, three alternative models of the tray were created by removing the anterior pegs, posterior pegs, and all pegs, respectively. The corresponding tibial models were also recreated with the same changes in tray geometries (Figure 5.2c).
- Tibiofemoral AP/IE load/kinematics: For each activity, the AP forces through the activity were smoothly amplified by a ratio so that the peak force pushing the femur posterior was 50, 100, and 150N larger, respectively, whereas the profile of the loading was unchanged (The sign of the force was unchanged for any frame). All the baseline models were re-tested under these new loading conditions. The changes in tibiofemoral positioning due to changes in tibiofemoral internal-external rotations were also considered. The input IE kinematics were smoothly amplified so that the internal rotation of the tibia at the frame having peak micromotion was 5 and 10° larger (resulted in a more posterior contact position at the lateral condyle).

Patient factors

- Bone material property: Up to 53% differences in elastic properties between samples with the same bone volume fraction were reported due to the different trabecular architectures (Ulrich et al., 1997). As the density-elasticity relationship used in the validated baseline models was approximately average of the reported range of tibial properties (Anderson et al., 1992; Keyak et al., 1994; Linde et al., 1991; Morgan et al., 2003; Rho et al., 1995; Snyder & Schneider, 1991), we perturbed the elastic modulus of the baseline tibial models by ±25% to cover reported variations in tibial elastic properties.

For specific factors, the modifications in geometric models were performed in HyperMesh (Altair Engineering, Inc., Troy, Michigan). In summary, a total of 147 models (three baseline and 144 perturbation models) were created and 441 simulations (147 models tested under three loading conditions) were run to complete this study.

5.3.3 Data analysis

In this study, we defined the tray-bone interface micromotion as the relative motions between the tray and the tibia contact surface. In computational models, the change in the distance (considering both shear and normal components) between the nodes at the tray bottom surface and the nearest node on the tibia implantation surface were used to represent the tray-bone interface micromotion. For each perturbed model, the micromotion at the tray-bone interface was predicted during each simulated activity. The full-field micromotion contour map for the frame having the peak micromotion is presented. The

maximum value of the interface micromotions through the entire activity cycle and the average micromotion across the cementless tray-bone contact interface at the corresponding frame were compared with the corresponding baseline model, and the impact of each factor on micromotion was then calculated and ranked.

In addition, we divided the tibial coverage area into three regions: micromotion less than 50μm (ideal for bone ingrowth), micromotion ranging from 50 to 150μm, and micromotion exceeding 150μm (inhibiting bone formation) (Engh et al., 1992; Pilliar et al., 1986). For each model, the coverage ratio of each region was calculated to provide a more comprehensive view of the fixation stability.

5.4 Results

For better visualization of the resulting micromotion variations, the full-field interface micromotion contour maps were presented in Figure 5.3 for the first specimen during GT activity (gait always had the highest micromotions), which covered the typical configurations for all factors. The patterns of the micromotion distributions during DKB and SD activities were similar but different in magnitude and thus were not shown. Overall, peak micromotion was consistently found along the anterior edge of the tray for all activities and ranged from 33.9 (Specimen1 during deep knee bending activity with the removal of all pegs) to 572.3 μm (Specimen2 during gait activity with an additional 150N posterior force). It should be noted that the high magnitude (572.3 μm) does not equal to not achieving biologic fixation, as the coverage ratio of regions experiencing micromotion less than 150 μm for this case was still over 70% (For a graphic reference, Figure 5.3-Tibiofemoral AP translation). To avoid the potential misunderstanding from the readers,

the coverage ratios of the three fixation levels were presented in Figure 5.4 for the second specimen during GT activity (which had the highest coverage ratios of the region experiencing micromotion exceeding 150μm among all specimens and activities).

Surgical parameters:

- Tray-bone alignment: For all specimens and activities, perturbations of the tray alignments along the AP translational and tibial slope DoFs resulted in an average of 20.6% (16.1%) and 9.0% (7.3%) changes in peak micromotions per 1.0mm or degree variations (values in round brackets represented the changes in average micromotions. Same for the following results). The average changes caused by perturbations along the other directions were much smaller [ML: 4.8% (3.0%); SI: 5.8% (4.4%); VV: 2.6% (2.0%); IE: 3.6% (1.8%)] (Figure 5.5a). The tibial surface modulus was almost unchanged except when perturbing the tray alignment along the SI direction (Figure 5.5b). The average change in contact modulus for each quadrant was 5.1MPa (2.1%) and the maximum change was less than 10.0% except for SI perturbations. Implanting the tray more superiorly resulted in a stiffer engagement, while implanting the tray more inferiorly resulted in a softer engagement. The phenomenon was most pronounced for the first specimen, which led to a larger impact of the tray alignment along the SI direction on the micromotion comparing with the other two specimens. Specifically, with the small perturbations studied, implanting the tray anteriorly, superiorly, or introducing a tibial posterior slope always resulted in lower interface micromotions, and implanting the tray in the

opposite directions resulted in higher micromotions consistently for all specimens.

For 1.0mm & degree perturbation bound models, the peak micromotions predicted from the upper-bound models were on average of 135.5% (115.9%), 91.6% (43.8%), and 146.0% (122.5%) larger than those predictions from the lower-bound models during GT, DKB, and SD activities, respectively (Figure 5.5c). The corresponding changes in the coverage ratio of the region experiencing micromotion more than 150 μm were up to 18.5% (Figure 5.4). The micromotions during the DKB activity were significantly smaller in magnitude than those in GT and SD activities.

- Tibial coverage: For all specimens, considerable increments in tibial coverage were achieved by using the enlarged tray models (Figure 5.6 top). When using the tray model with extra coverage in all regions (an average of 12.3% additional area), the tibia was fully covered around the perimeter except the zone for the posterior cruciate ligament (Figure 5.2b). The average changes in the peak micromotion with the usage of these all-covered tray models were 0.7% (0.5%), 1.3% (0.7%), and 1.9% (0.9%) for specimens 1, 2, and 3, respectively (Figure 5.6 bottom). The maximum change in micromotion was less than 4% (2%). It should be noted that the micromotion at the extra surface of the tray beyond bony contact were excluded from the results (Figure 5.3-Tibial coverage) for the comparison.
- Tibial angular resection error: The impact of angular resection errors was substantial for the DKB activity (Figure 5.7a) but remained smaller than GT or

SD activities. This was a result of relative motions of the unsupported regions greatly exceeded the small baseline micromotions at the anterior aspect (Figure 5.3-Resection error). For all activities, the peak micromotions at the anterior aspect were increased by an average of 13.8% due to the instability introduced by the resection errors. However, the average micromotion increased by an average of 74.8% due to the significantly reduced area experiencing micromotion less than 50 μm. The impact was highest for a posterior angular resection error followed by medial, and lateral resection errors, however, at the same level. In addition, regions experiencing micromotion less than 50 μm reduced by an average of 33.5%, 16.3%, and 42.4% during GT, DKB, and SD, respectively, when a posterior resection error was created (Figure 5.4). These reductions in the ideal area for bone ingrowth (<50 μm) were more severe than those with a medial or lateral angular resection error (Table 5.1).

Design parameters:

- Tray-bone coefficient of friction: Overall the peak micromotions (occurred during gait among the three activities) reduced by an average of only 9.7% (15.1%) when increasing the coefficient of friction from 0.6 to 1.4 (the full range evaluated here) (Figure 5.7b).
- Tray pegs: The impact of tray pegs was small for the rotating-platform implant (Figure 5.7c). The anterior pegs play some role in restricting the tray tilting motion at the anterior side (Figure 5.3-Removal of tray pegs). The peak micromotions increased by an average of 11.1% with the removal of anterior

pegs when the micromotion exceeded 150 μm (specimens 1and 2 during GT and SD). However, the removal of all pegs did not make these situations substantially worse. The peak micromotions only increased by an average of 13.3% with the removal of all pegs. For the implant studied, the cone provided this primarily stability resisting micromotion. It should be noted that with the removal of peg geometries, the total cementless contact area reduced by 25%, which led to a higher increase in the average micromotion (22.2%) as the removed geometries had small micromotions.

- Tibiofemoral AP/IE load/kinematics: The changes in tibiofemoral contact positioning due to the different AP forces and IE rotations were shown in Figure 5.8a for specimen 1 (The patterns for specimens 2 and 3 were similar). The medial and lateral contact locations moved posteriorly with increased AP forces. A posterior tibiofemoral contact position due to a 100N larger posterior force resulted in 54.8% (60.1%), 65.2% (71.2%), and 81.8% (82.7%) increments in the peak micromotions for specimens 1, 2, and 3, respectively (Figure 5.8b). The medial-lateral contact rotated by a similar angle when the IE rotations were perturbed (Figure 5.8a). During DKB activity, the lateral contact also moved posteriorly with increased tibial internal rotation. Peak micromotions were increased by an average of 198.5 μm during DKB activity but increases were much smaller during GT and SD activities (changed by an average of 24.7 μm) when the tibial internal rotation was increased by 10° (Figure 5.8c). For all models (with increased AP force or increased tibial

internal rotation), the micromotions were linearly related to the resulting moments as a result of the posterior positions evaluated (R=0.99).

Patient factor:

- Bone material property: The peak interface micromotions reduced by an average of 19.9% (17.1%) when the tibial material properties were increased by 25%, and micromotions increased by an average of 38.4% (34.3%) when the tibial material properties were decreased by 25% (Figure 5.7d). Up to 14.7% difference in the coverage ratio of the region experiencing micromotion exceeding 150 μm was found due to the variations in the tibial elastic property (Figure 5.4).

For each factor, micromotions in liftoff and shear directions increased/decreased simultaneously following the same trend as the presented total micromotions, where the liftoff micromotions were more sensitive to the studied factors than the shear micromotions (Figure 5.9).

5.5 Discussion

The coverage ratio of the tray-bone cementless contact region experiencing micromotion less than 50 μm was highly related to the average micromotion across the contact interface. Therefore, investigating the tray-bone interface micromotion is a good approach to evaluate the tibial fixation performance. In this study, we investigated tray-bone interface micromotion during gait, deep knee bending, and stair descent activities for

three validated proximal tibial models. Specifically, we assessed the impact of seven common TKA factors on the interface micromotions. In all cases, the maximum micromotion always occurred at the anterior tray-bone contact interface, and no more than 50μm micromotions were observed in the posterior regions except when a posterior resection error was created.

The tray-bone alignment had a significant impact on tray-bone micromotions. We found that implanting the tray anteriorly, superiorly, or increasing the tibial posterior slope reduced the micromotion for all three specimens. Among these, the decrease in micromotion caused by the superior implantation was due to the increased tibial elastic modulus at the contact surface. When the change in surface modulus was small, the corresponding change in micromotion was also minimal (Figure 5.5-Specimen 2). It was hypothesized that anteriorly aligning the tray might increase the contact modulus anteriorly (tray on a cortical lip) but decrease it posteriorly (tray off a cortical lip). However, for the three tibial specimens used in this study, the average change in contact modulus for each quadrant due to perturbing the tray alignment 1.0 mm in the AP direction was only 3.0% (the maximum value was 7.0%). The decrease in micromotion caused by anterior implantation was a result of the tray-bone contact locations also moving anteriorly, which centralized the load transfer with respect to the tibial shaft, reducing the tibial bending and thereby reducing lifting of the tray at the anterior aspect. Micromotion was not sensitive to perturbation of the alignments along the other DoFs (ML, VV, and IE).

Similar to posterior positioning of the tray, posterior load transfer as a result of 100N increases in posterior loading leads to significant increases in micromotion. Again, this is the result of greater posterior offset of the load which maximizes the flexion-extension

moment and anterior tray micromotion. Similarly, the micromotion was significantly increased during the DKB activity due to the considerable posterior offset of the load. Changes in micromotion were much smaller during GT and SD activities as the contact locations were minimally shifted in the AP direction (Figure 5.8c). The interaction here with articular design is important to note in that a geometry that constrains the load transfer more centrally will minimize the anterior micromotion. This is in line with a previous study which denied the hypothesis that a relatively unconstrained articular geometry would result in less migration of the tibial component (Uvehammer, 2001), but peak micromotion appears primarily influenced by AP contact position and the resulting increase in moment about the anterior aspects of the tray.

Several studies have proposed that maximizing the tibial coverage should theoretically improve fixation performance due to the more uniform force distributions (Bertin, 2007; S. Martin et al., 2014; Wernecke et al., 2012). However, we found that the extra coverage above a 'best-fit' symmetric tray had a minimal impact on the micromotion. An average of 8.9% extra coverage only resulted in a 1.3% change in the micromotion. In addition, as it is impossible to obtain greater tibial coverage than using the virtual implant (which covered all the tibial resection surface) created in this study the impact of maximizing the tibial coverage on the micromotion would be even smaller in clinical practice. In fact, choosing a larger tray to maximize coverage, but also simultaneously moving (as typical) contact locations posteriorly may even be counterproductive, as the influence of the posterior load transfer would increase micromotion. This evaluation also suggests that design efforts with respect to micromotion need not focus on maximizing coverage via tray asymmetry.

Finally, note that this study did not focus on determining a minimum appropriate coverage, which should be further explored.

The uneven resection surface caused by angular cutting error during the tibial preparation had a moderate influence on the peak micromotion, as the peak micromotions at the anterior aspect did not increase greatly, indicating that the cone provides significant support compared with the tray surface. However, introducing large unsupported regions (Figure 5.3-Resection error), led to a significant reduction in the ideal area for bone ingrowth (<50 μm) as expected. Clearly, minimizing angular resection error at the posterior aspect is important as this pattern resulted in a minimal ideal area for bone ingrowth.

It should be noted that the implant used in this study was a rotating-platform design. The impact of tray pegs investigated here is not directly comparable to typical a fixed-bearing implant. We found that the anterior tray pegs inhibited micromotion, likely as the peak micromotions always occurred at the anterior aspect. However, overall, the pegs were responsible for only a small percentage of tray stability, as complete removal demonstrated an average increase of 13.3% of peak micromotion. The coefficient of friction also has only a small impact on the micromotion over a wide range studied, but clearly, intentional increase in friction will aid minimizing micromotion. Patient individual differences with respect to bone material properties had significant impact on the tray-bone interface micromotion. The differences in elastic modulus evaluated, up to 53% with the same bone volume fraction (Ulrich et al., 1997), resulted in up to 74% differences in the micromotion.

This study has limitations to note. Only one implant design (rotating-platform, cruciate-retaining) was considered. The external boundary conditions and resulting sensitivities may be different for other tray designs. The impact of tray pegs investigated here is likely

not reflective of the response for a fixed-bearing design. However, we believe the relative impact of the other factors would be still valid for a fixed-bearing design and other implants, as the mechanisms are relatively unchanged. We used 1 mm and 1 degree as the upper limit of the perturbations when studying the impact of tray-bone alignment parameters, and the translational positioning reflects available space on the resection surface. We verified the corresponding changes in the joint loading conditions were negligible under these perturbations. However, when the perturbations are large enough, the impact of the changes in the implant loading conditions may not be ignored. A 5° posterior slope would result in modification of femoral-insert posterior contact comparing with a 0-degree slope (H. Yang et al., 2021), which would offset the positive effect of increasing the posterior slope on reducing the micromotion. In addition, tibiofemoral anterior-posterior positioning is multifactorial, as patient factors (body weight, limb alignment) surgical choices (posterior slope), and articular design all contribute. Further research could include a more comprehensive study on this factor.

In general, this study assessed the impact of seven common TKA factors on the tray-bone interface micromotion. Based on the results and discussion above, we ranked the impact of each factor on the peak micromotion from high to low in the following order: tibiofemoral posterior positioning (due to posterior load), tray-bone alignment, bone elastic properties, tibial angular resection error, the inclusion of tray pegs (anterior pegs having a greatest effect), tray-bone coefficient of friction, and tibial coverage. Among these, the impact of the tibial coverage was negligible. If looking at the average micromotion instead of peak micromotion, the tibial resection error would be the most impactful since it resulted in the highest average micromotion whereas the changes in the peak micromotion were not

significant. The other factors remain in the same order. The ranking is clearly dependent on the parameter settings evaluated for each factor. There are clear recommendations for minimizing micromotion from this assessment, including centralizing the load transfer where possible with tray positioning, and less concern toward maximizing tibial coverage. However, as this is primarily a sensitivity screening study, critical parameters identified should be further explored to understand the potentially complex relationship with resulting micromotion. The study also highlights the importance of articular design in that greater AP stability that centralizes the contact point will aid in minimizing micromotion.

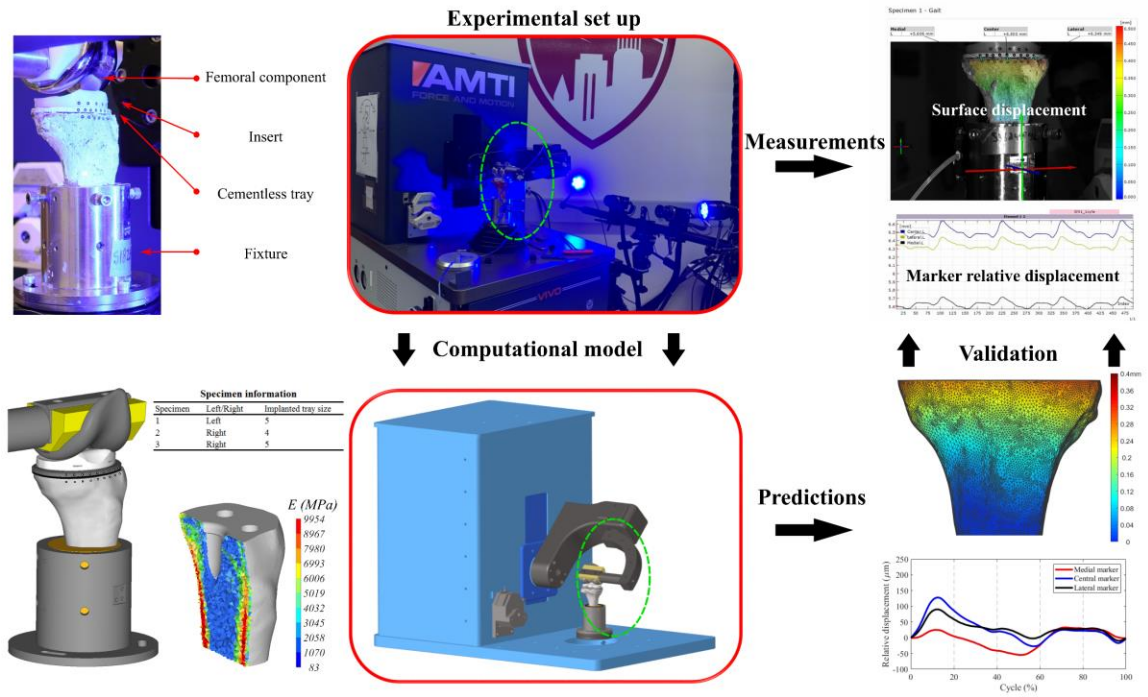

Figure 5.1: Computational-experimental validation framework. Specimen information was listed in the table.

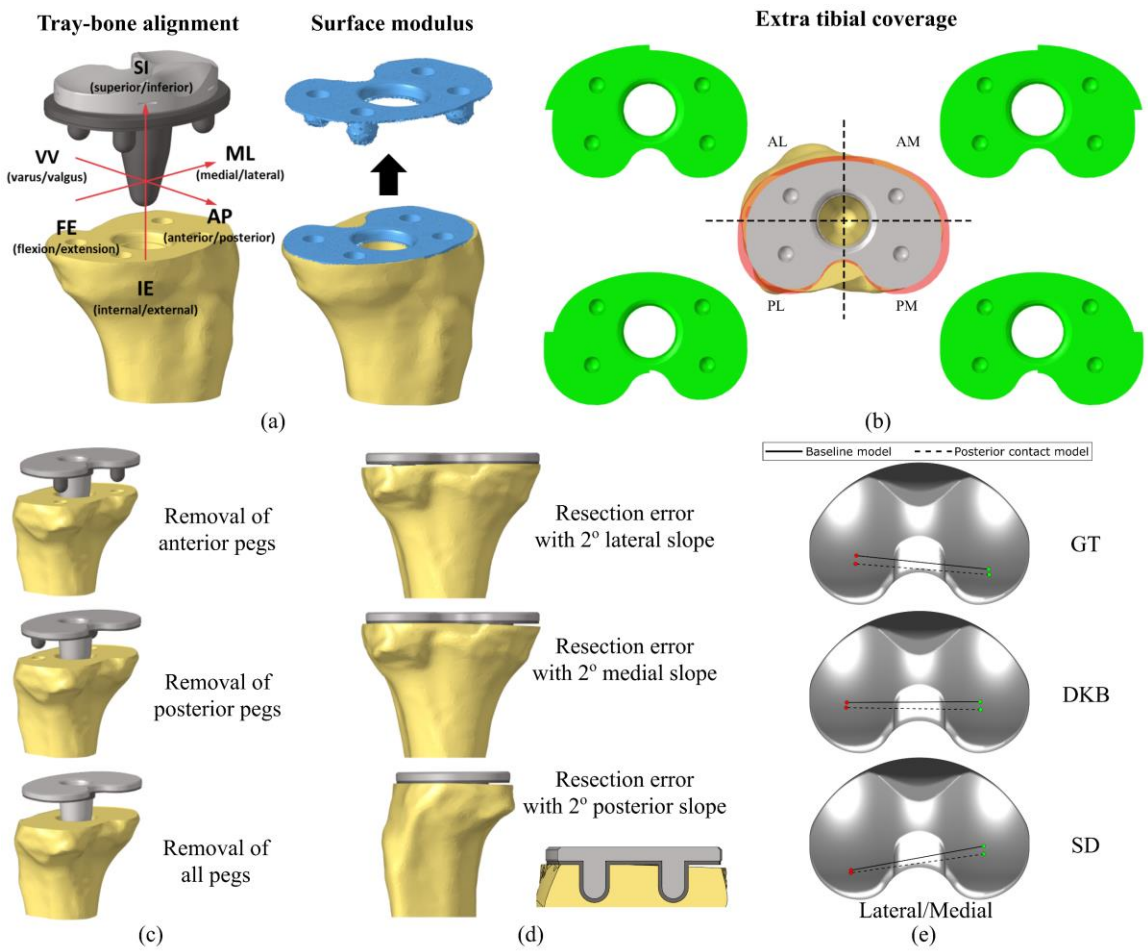

Figure 5.2: Illustration of the perturbation models for micromotion sensitivity tests (using a left tibia sample). (a) Tray-bone alignment perturbations and the isolated elements for calculating tibial surface modulus. (b) Region divisions of the tibial coverage (AL – Anterolateral; AM – Anteromedial; PL – Posterolateral; PM - Posteromedial). Five virtual tray models with extra tibial coverages (Grey – original tray; Green – trays with extra coverage in each quadrant; Red – tray with extra coverage in all regions). (c) Tray and tibial models for studying the impact of tray pegs. (d) Tibial models with 2°-slope resection errors. (e) Differences in tibiofemoral AP translations between baseline models and posterior-contact models (+100N posterior load) at peaking micromotion frames.

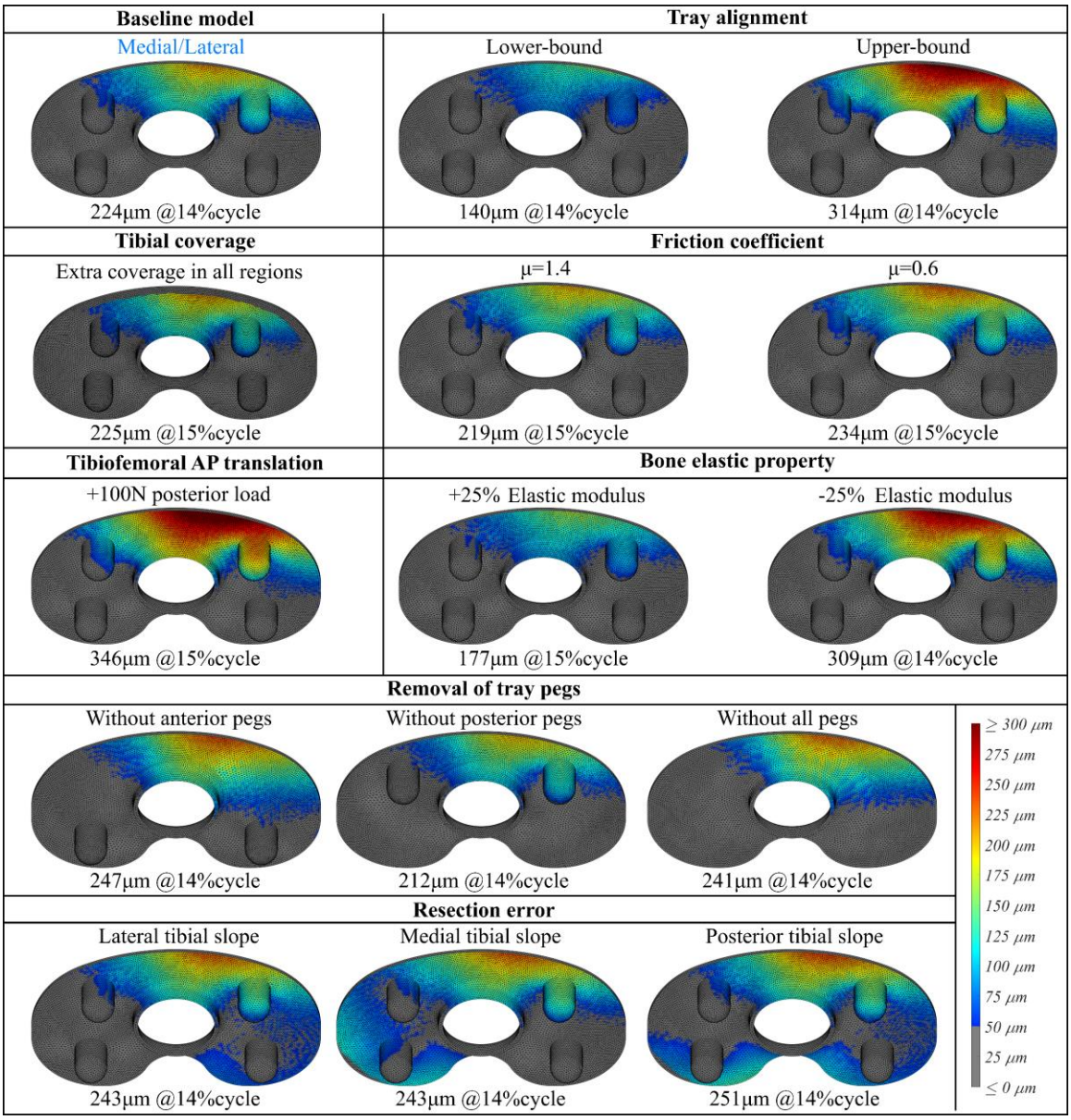

Figure 5.3: The predicted full-filed interface micromotion contour maps at the frames having peak micromotion magnitudes for the baseline model and the typical perturbation models of each factor. (The presented plots were from the first specimen during gait activity)

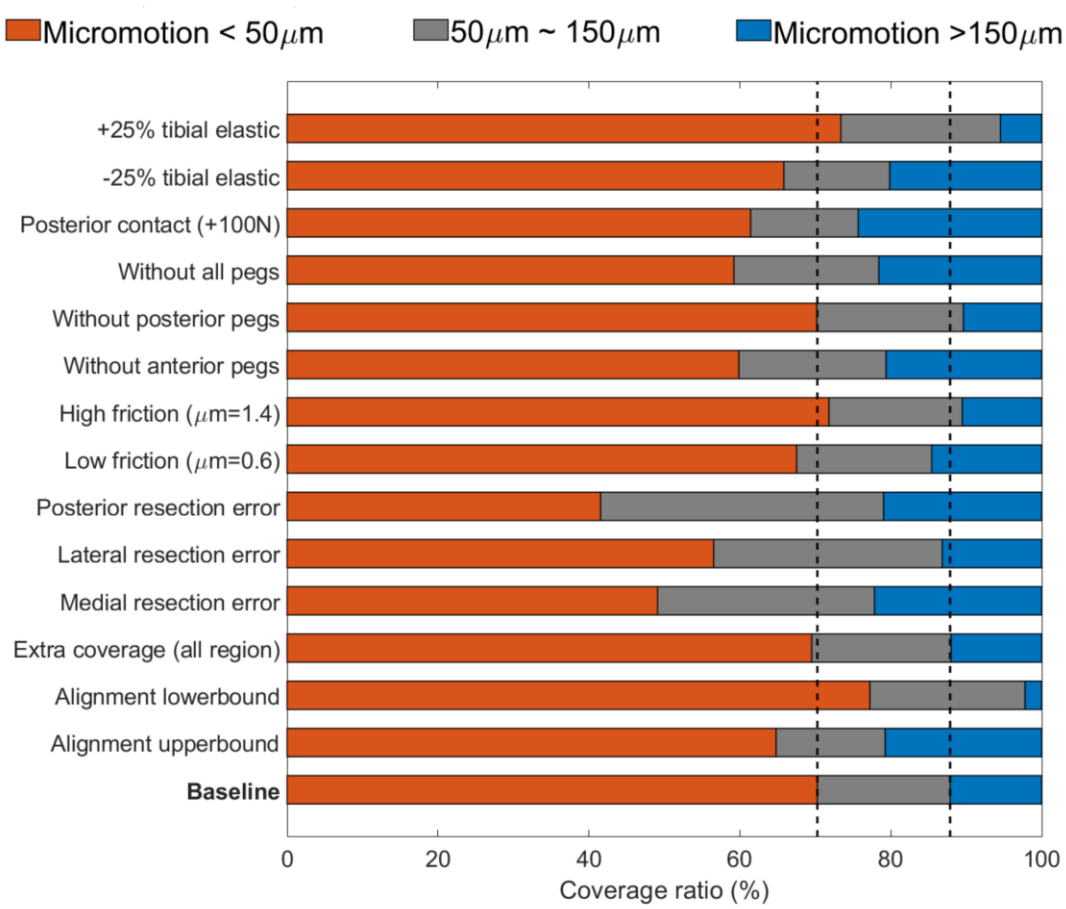

Figure 5.4: The coverage ratios of the three fixation levels at the tray-bone contact interface. (The presented plot was from the second specimen during gait activity)

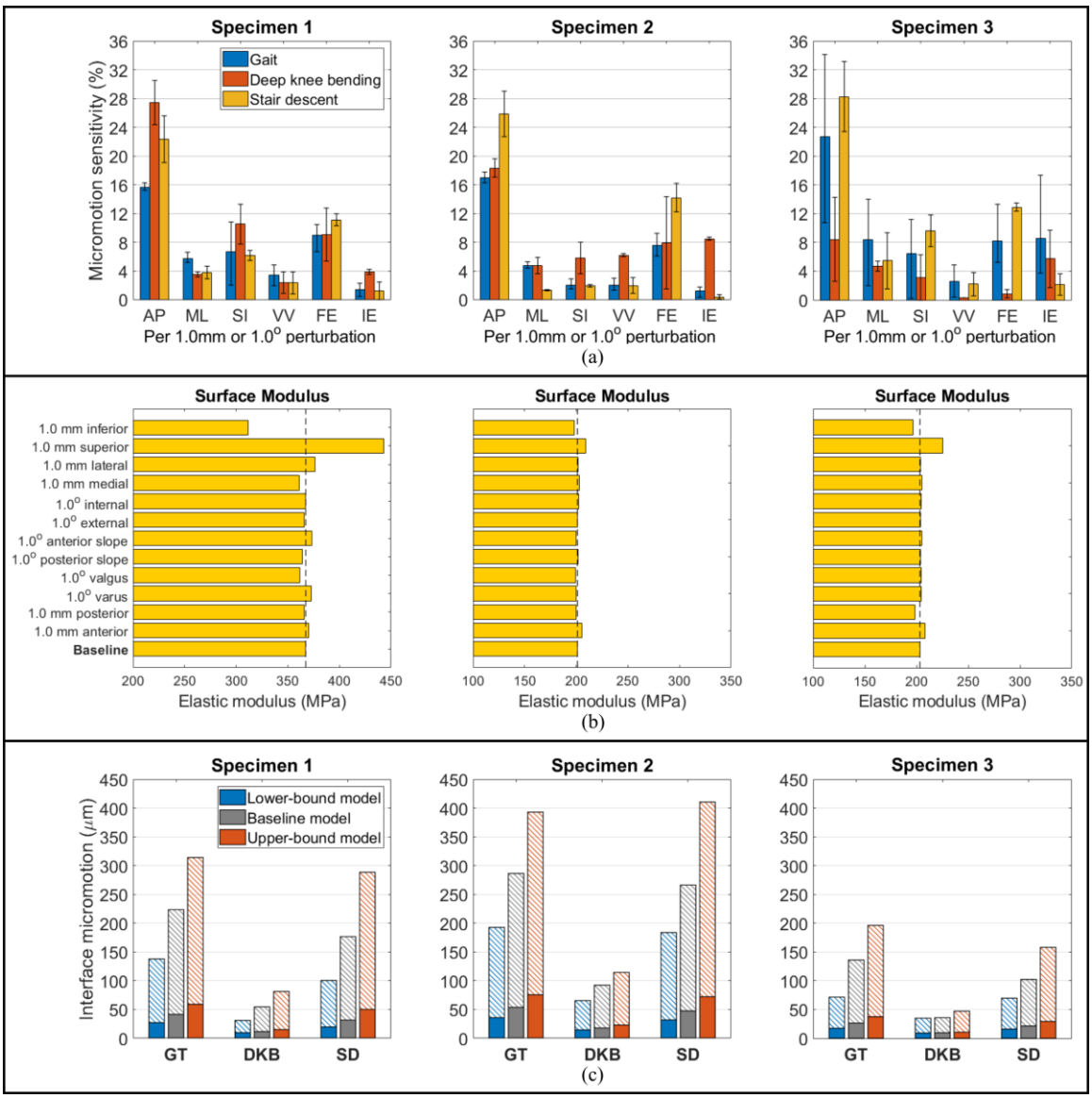

Figure 5.5: (a) The impact of tray alignment parameters on the interface micromotion with per 0.5 mm or degree perturbation. (b) Variations of the tibial surface modulus at the contact interface due to the changes in the tray-bone alignment. (c) Comparisons of the interface micromotions between the baseline models and the lower/upper-bound models (combination of perturbing tray-bone alignment 1.0 mm & degree in 6-DoFs). *(Note: The hatched bars represented the peak micromotions and the solid bars represented the average micromotions. Same for the subsequent figures)*

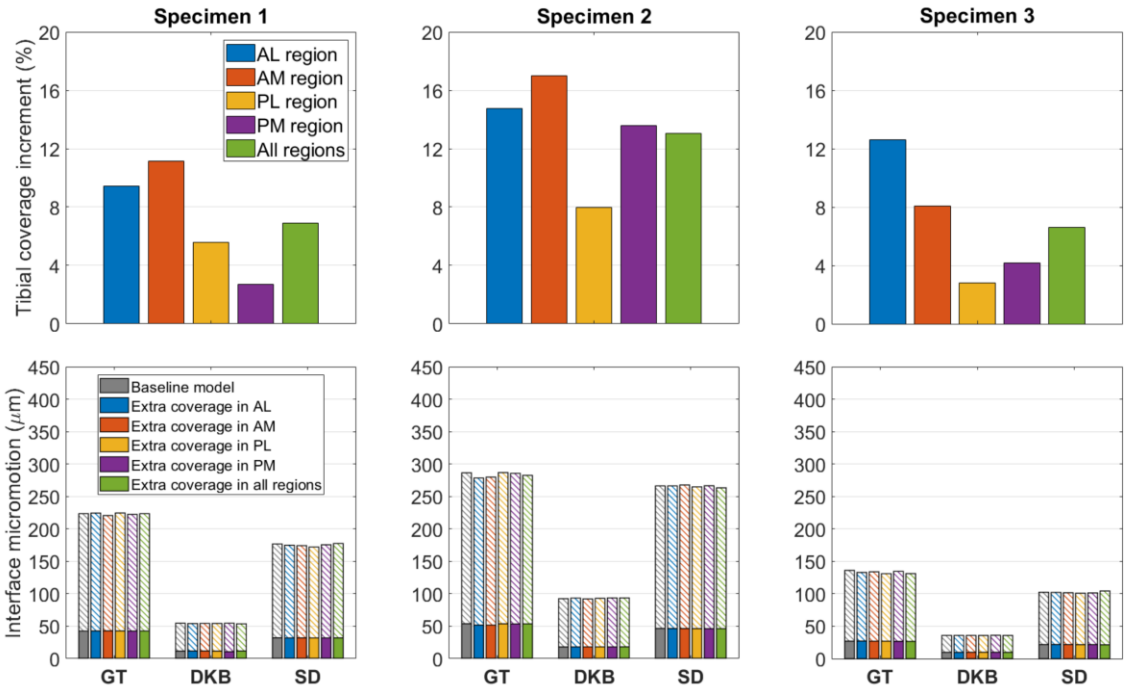

Figure 5.6: Tibial coverage increments in each region when using enlarged tray models (top). Comparisons of the interface micromotions between the baseline models and the models with extra tibial coverage (bottom). (*AL – Anterolateral; AM – Anteromedial; PL – Posterolateral; PM – Posteromedial)*

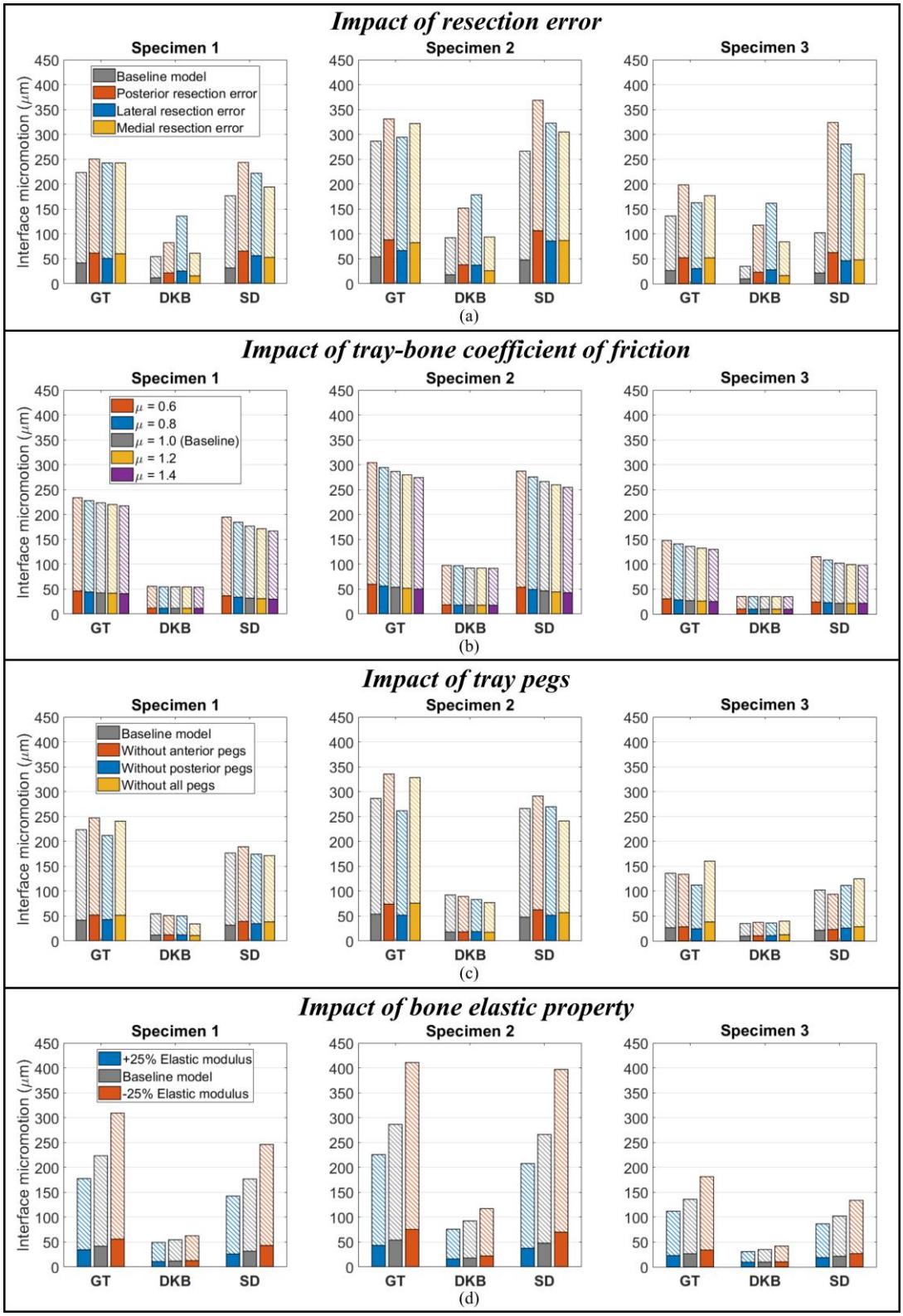

Figure 5.7: Impact of resection error (a), tray-bone coefficient of friction (b), tray pegs (c), and bone elastic property (d) on the interface micromotions.

Table 5.1: Ratio of the tray-bone cementless contact regions experiencing micromotion less than 50 μm to total bone-porous contact area. The minimal ratios were highlighted in bold.

Specimen 1	**Baseline model**	**Model with resection errors**		
		Medial	Lateral	Posterior
Gait	74.1%	53.3%	64.6%	53.0%
Deep knee bending	99.9%	99.7%	83.3%	91.4%
Stair descent	80.2%	54.6%	60.0%	**49.0%**
Specimen 2	**Baseline model**	**Model with resection errors**		
		Medial	Lateral	Posterior
Gait	70.3%	49.1%	56.5%	41.6%
Deep knee bending	93.9%	85.4%	71.9%	69.7%
Stair descent	75.0%	47.5%	52.3%	**38.9%**
Specimen 3	**Baseline model**	**Model with resection errors**		
		Medial	Lateral	Posterior
Gait	84.6%	56.0%	80.9%	58.3%
Deep knee bending	100.0%	97.5%	80.4%	85.6%
Stair descent	90.7%	65.4%	67.6%	**53.9%**

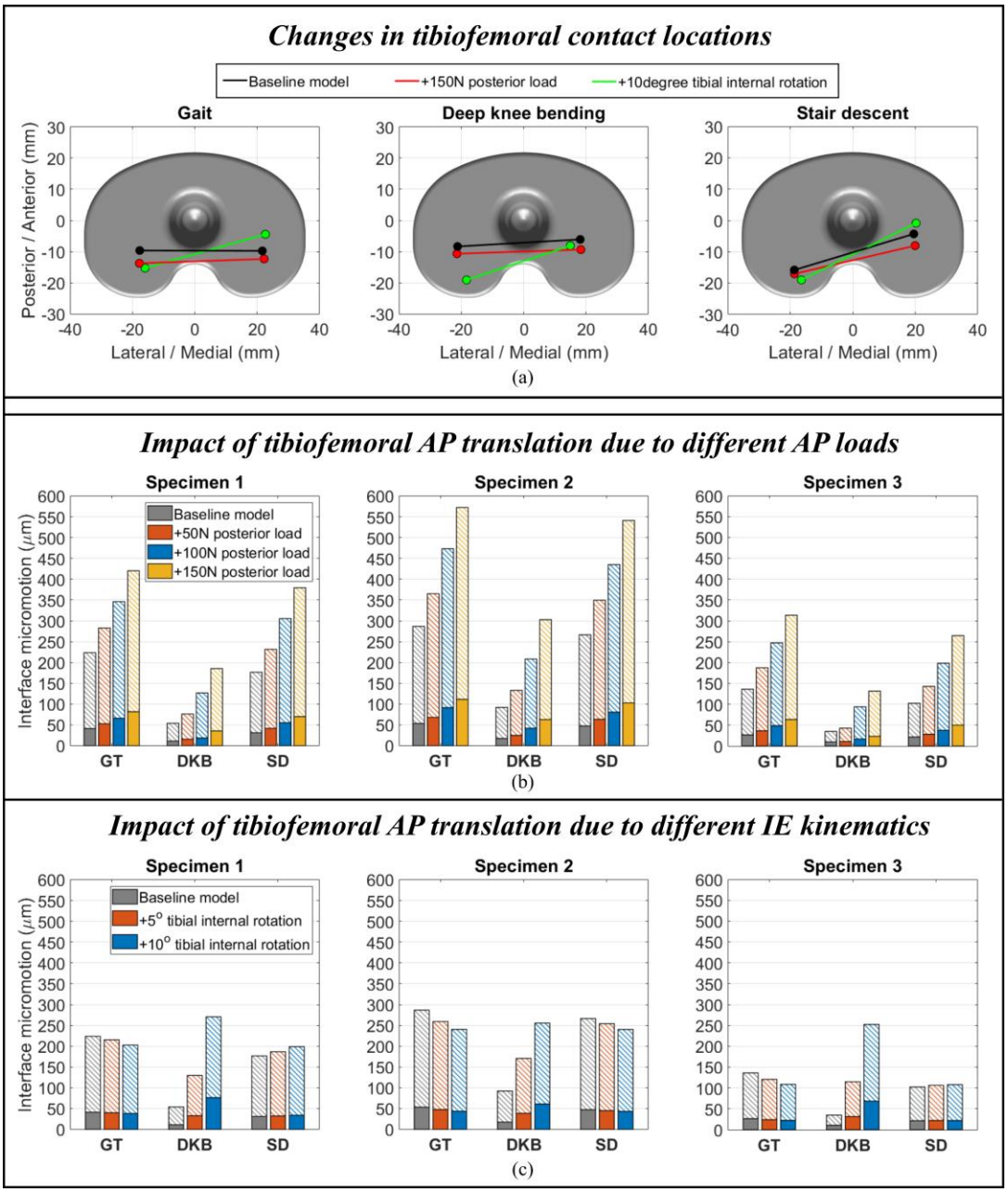

Figure 5.8: (a) Projection of the femoral-insert medial/lateral contact points on the cementless tray for a left tibia specimen. (b) Comparison of the interface micromotions between the baseline models and the models with increased posterior loads. (c) Comparison of the interface micromotions between the baseline models and the models with increased tibial internal rotations.

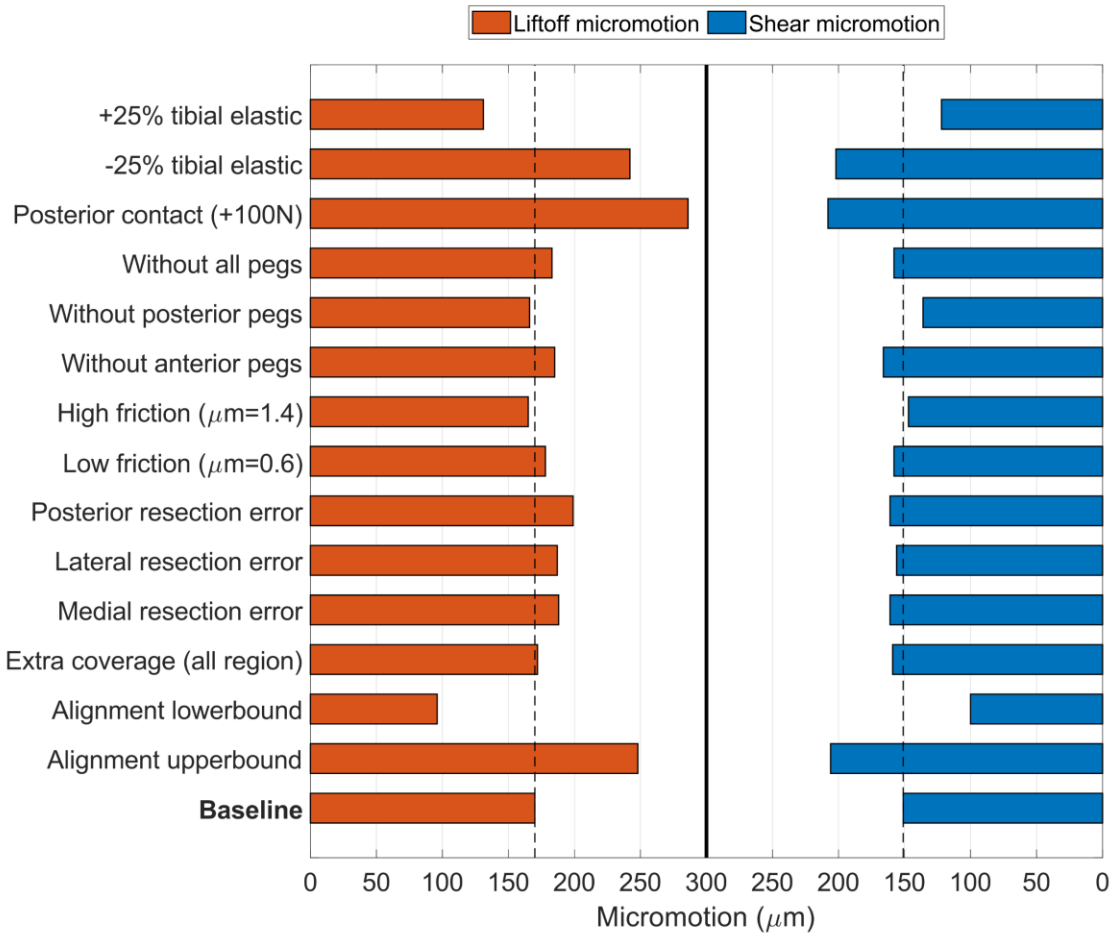

Figure 5.9: The liftoff and shear components of the total micromotion presented in this study (The reference plot was from the first specimen during gait activity).

CHAPTER 6. CONCLUSIONS AND RECOMMENDATIONS

6.1 Conclusion

Good implant fixation after TKA is essential to ensure long-term survivorship. Understanding how the TKA factors influence bone remodeling and osseointegration is very important to improve tibial fixation. The overall objective of this dissertation was to create an experiment to finite element analysis pipeline for investigating the sensitivities of common TKA factors to the tibial strain energy density distributions and the tray-bone interface micromotion. Three interrelated studies were performed to achieve this goal. An experimental-computational validation framework for predicting the tibial micromotion and bone deformation was developed firstly, which addressed the main issue that limited the use of computational modeling in clinical practice: *model validation*. The validated models were then used to investigate sensitivities of common TKA factors to the tibial strain energy density (SED) and tray-bone interface micromotion.

Computational models must be validated in order to be trusted. A significant contribution of this dissertation was the extensive model validations under physiological conditions, which were firstly performed in Chapter 3 and utilized in the subsequent studies. Chapter 3 presented an experimental-computational validation framework based on cadaveric tests for investigating tray-bone interface micromotions and bone deformations under physiological loading conditions. Unlike other studies that only

validated their model by comparing the predictions and measurements in a few distinct points, our validation considered both marker relative displacements and surface displacements, which greatly improved the reliability of the validation and thus providing more confidence in predictions in the subsequent studies. Although mainly focused on validation, this study also had some important findings. It was found that the initial tray-bone alignment in anterior-posterior directions had a considerable impact on the interface micromotions, which was the motivation of the follow-up micromotion sensitivity study in Chapter 5. We also found marker relative displacements were usually smaller than actual interface micromotions. This was mainly because that the peak interface micromotion usually occurred in between the positioned marker couples. Therefore, we suggest that some caution should be taken when using marker relative displacements to characterize the actual interface micromotion.

Bone remodeling after TKA surgery is regulated by the changes in strain energy density. Understanding how TKA factors influence the post-operative SED distribution is very important to improve fixation performance. Chapter 4 evaluated the potential differences in post-operative proximal tibial SED distributions for five typical TKA parameters. The study was the first one that considered both femoral-insert contact and soft tissue loading conditions when investigating bone strains. The tibial anatomy was found to have the largest impact on post-operative bone strains. For the tibia that had less remaining bone stock posteriorly, a relatively larger posterior slope was recommended to increase the posterior wall thickness, which improved the SED distributions and thus could avoid potential bone loss. The impact of PCL balancing, surgical alignment, and tray posterior slope were considerable. The SED changes for these three factors were mainly due to the

changes in loading conditions. Among those, PCL balancing affects the overall strain energy magnitude, whereas the alignment and posterior slope primarily influence the medial-lateral and anterior-posterior SED distributions, respectively. The impact of tray material modification was much smaller than the factors above. These findings indicated the maximizing post-operative fixation is possible using optimized surgical parameters to address patient anatomy.

The initial fixation of cementless tibial trays is crucial to bony ingrowth onto the porous surface of the implants, as micromotion magnitudes exceeding 150 μm may inhibit bone formations and limit fixation. Chapter 5 assessed the impact of seven common TKA factors on the tray-bone interface micromotion during a series of activities of daily living. The computational models and boundary conditions were adopted directly from the validation study in Chapter 3, which provided more confidence in the computational outcomes. It was found that the tray-bone interface micromotion was very sensitive to femoral-insert posterior contact (achieved by posterior tray alignment and increasing tibiofemoral posterior forces in this study), as the posterior offset of the load maximized the flexion-extension moment and anterior tray micromotion. An angular resection error at the tibial resection surface did not greatly increase the peak micromotion but resulted in a minimal ideal area for bone ingrowth. It was thought that maximizing the tibial coverage should theoretically improve fixation performance due to the more uniform force distributions (Bertin, 2007; S. Martin et al., 2014; Wernecke et al., 2012). However, we found that the extra coverage above a 'best-fit' symmetric tray had a minimal impact on the micromotion. Due to the difference in bone material properties between individuals, we found the same knee system could result in up to 73.8% difference in the micromotion, which cannot be

avoided in the clinic. Therefore, minimizing the micromotion may be particularly required in some situations. The findings in this study brought clear recommendations for minimizing micromotion, including centralizing the load transfer where possible with tray positioning, centralizing the contact point using the implant that has greater AP stability, minimizing resection error at the posterior aspect, and less concern toward maximizing tibial coverage.

6.2 Recommendations

The studies presented in this dissertation were mainly performed via finite element methods, supplemented by experimental testing for validation purposes, as most of the research cannot be achieved through experimental methods. Although the goal of the dissertation was smoothly attained, there always be opportunities to improve the detail and complexity of models for more accurate and comprehensive investigations.

One limitation in the validation study (Chapter 3) was that only one density-elasticity relationship was considered for the three tibiae specimens. A previous study discussed that each bone specimen could have a characteristic density-elasticity relationship (Eberle et al., 2013). Another study also reported that differences in tibial elastic properties between samples with the same bone volume fraction could range up to 53% due to the different trabecular architectures (Ulrich et al., 1997). These indicated that directly mapping bone material properties from CT scans with a fixed density-elasticity relationship may not represent the actual material properties. Future validation studies using human bone models could modify the bone properties within the reported range during the validation procedure to improve the validation accuracy.

The main limitation in the application studies (Chapter 4 and 5) was that the computational analyses were based on a limited number of tibial models (no more than three), which was insufficient to cover a large patient population. The outcomes may still be true when extrapolating our findings to a larger patient population but need verifications. However, including more specimens requires more effort in model validations, and the specimens may still not fully represent the large variation in human bones. We recommend that future studies make attempts to utilize statistical shape models (SSMs) to assess the implant stability and study the sensitivity of critical parameters influencing fixation performance, as SSMs describe the anatomical variation and have characterized the morphology of individual bones (Smoger et al., 2017).

Additionally, the number of tested implants was also limited in each study. Some of the outcomes may be different for other implant designs. For example, In Chapter 4, the loading patterns may be different for other implants, which would influence the strain distributions; In Chapter 5, the impact of tray pegs investigated for a rotating-platform design is likely not reflective of the response for a fixed-bearing tray. More implant designs could be easily tested in the future by using the computational models and workflows presented in this dissertation.

In Chapter 4, the change in tibial strain energy density distributions was investigated to evaluate the effect of each factor on bone remodeling. However, the extent of bone remodeling due to these SED changes was unknown. Computational simulations have already been utilized to directly predict bone remodeling patterns using the strain-parameter-related remodeling equations (Anijs et al., 2020; Cawley et al., 2012; Chong et al., 2011b; Jia et al., 2017; Quilez et al., 2017). These predictions may be more preferred

by surgeons and implant developers because they provide a direct evaluation of the risk of potential aseptic loosening. However, these predictions are hard to validate, as different remodeling equations could result in distinct predictions, which is also why this method was not used in this dissertation. Future works could use validated bone remodeling equations to study the effect of TKA factors.

6.3 Closing

In conclusion, this dissertation presented a systematic research framework from model validation to model application for evaluating the TKA fixation stability. The findings in this work contributed to the pre-clinical assessment and further implant development. There are clear recommendations for improving the implant fixation after the cemented and cementless TKA, such as optimizing surgical parameters to improve the bone SED distributions and centralizing the load transfer to reduce the tray-bone micromotion. Future work is needed to improve the research methods and to extrapolate our findings to a larger population. The computational tools developed in this work could be used as a good start for future research.

REFERENCES

Abdul-Kadir, M. R., Hansen, U., Klabunde, R., Lucas, D., & Amis, A. (2008). Finite element modelling of primary hip stem stability: The effect of interference fit. *Journal of Biomechanics*, *41*(3), 587–594.

Abrahams, M. (1967). Mechanical behaviour of tendonIn vitro. *Medical & Biological Engineering*, *5*(5), 433–443.

Abu-Amer, Y., Darwech, I., & Clohisy, J. C. (2007). Aseptic loosening of total joint replacements: mechanisms underlying osteolysis and potential therapies. *Arthritis Research & Therapy*, *9*(Suppl 1), S6.

Abu-Rajab, R. B., Watson, W. S., Walker, B., Roberts, J., Gallacher, S. J., & Meek, R. M. D. (2006). Peri-prosthetic bone mineral density after total knee arthroplasty. *The Journal of Bone and Joint Surgery. British Volume*, *88-B*(5), 606–613.

Adalberth, G., Nilsson, K. G., Byström, S., Kolstad, K., & Milbrink, J. (2001). All-polyethylene versus metal-backed and stemmed tibial components in cemented total knee arthroplasty. *The Journal of Bone and Joint Surgery. British Volume*, *83-B*(6), 825–831.

Aggarwal, V. K., Goyal, N., Deirmengian, G., Rangavajulla, A., Parvizi, J., & Austin, M. S. (2014). Revision Total Knee Arthroplasty in the Young Patient: Is There Trouble on the Horizon? *Journal of Bone and Joint Surgery*, *96*(7), 536–542.

Ali, A. A., Mannen, E. M., Rullkoetter, P. J., & Shelburne, K. B. (2020). Validated Computational Framework for Evaluation of In Vivo Knee Mechanics. *Journal of Biomechanical Engineering*, *142*(8).

Ali, A. A., Shalhoub, S. S., Cyr, A. J., Fitzpatrick, C. K., Maletsky, L. P., Rullkoetter, P. J., & Shelburne, K. B. (2016). Validation of predicted patellofemoral mechanics in a finite element model of the healthy and cruciate-deficient knee. *Journal of Biomechanics*, *49*(2), 302–309.

Ali, A. M., Newman, S. D. S., Hooper, P. A., Davies, C. M., & Cobb, J. P. (2017). The effect of implant position on bone strain following lateral unicompartmental knee arthroplasty. *Bone & Joint Research*, *6*(8), 522–529.

Alipit, V., Kirk, A., Scholl, D., Schmidig, G., Springer, B. D., & Lee, G. C. (2021). Micromotion Analysis of Various Tibial Constructs in Moderate Tibial Defects in Revision Total Knee Arthroplasty. *The Journal of Arthroplasty*, *36*(1), 362–367.

Amiri, S., & Wilson, D. R. (2012). A Computational Modeling Approach for Investigating Soft Tissue Balancing in Bicruciate Retaining Knee Arthroplasty. *Computational and Mathematical Methods in Medicine*, *2012*, 1–11.

Anderson, M. J., Keyak, J. H., & Skinner, H. B. (1992). Compressive mechanical properties of human cancellous bone after gamma irradiation. *The Journal of Bone & Joint Surgery*, *74*(5), 747–752.

Anijs, T., Wolfson, D., Verdonschot, N., & Janssen, D. (2020). Population-based effect of total knee arthroplasty alignment on simulated tibial bone remodeling. *Journal of the Mechanical Behavior of Biomedical Materials*, *111*, 104014.

Aprato, A., Risitano, S., Sabatini, L., Giachino, M., Agati, G., & Massè, A. (2016). Cementless total knee arthroplasty. *Annals of Translational Medicine*, *4*(7), 129.

Ardestani, M. M., Moazen, M., Maniei, E., & Jin, Z. (2015). Posterior stabilized versus cruciate retaining total knee arthroplasty designs: Conformity affects the performance reliability of the design over the patient population. *Medical Engineering & Physics*, *37*(4), 350–360.

Ardestani, M. M., ZhenXian, C., Noori-Dokht, H., Moazen, M., & Jin, Z. (2019). Computational analysis of knee joint stability following total knee arthroplasty. *Journal of Biomechanics*, *86*, 17–26.

Asokan, A., Plastow, R., Kayani, B., Radhakrishnan, G. T., Magan, A. A., & Haddad, F. S. (2021). Cementless knee arthroplasty: a review of recent performance. *Bone & Joint Open*, *2*(1), 48–57.

Au, A. G., James Raso, V., Liggins, A., & Amirfazli, A. (2007). Contribution of loading conditions and material properties to stress shielding near the tibial component of total knee replacements. *Journal of Biomechanics*, *40*(6), 1410–1416.

August, A., Aldam, C., & Pynsent, P. (1986). The McKee-Farrar hip arthroplasty. A long-term study. *The Journal of Bone and Joint Surgery. British Volume*, *68-B*(4), 520–527.

Aujla, R. S., & Esler, C. N. (2017). Total Knee Arthroplasty for Osteoarthritis in Patients Less Than Fifty-Five Years of Age: A Systematic Review. *The Journal of Arthroplasty*, *32*(8), 2598–2603.

Bah, M. T., Shi, J., Heller, M. O., Suchier, Y., Lefebvre, F., Young, P., King, L., Dunlop, D. G., Boettcher, M., Draper, E., & Browne, M. (2015). Inter-subject variability effects on the primary stability of a short cementless femoral stem. *Journal of Biomechanics*, *48*(6), 1032–1042.

Barker, D. S., Tanner, K. E., & Ryd, L. (2005). A Circumferentially Flanged Tibial Tray Minimizes Bone-Tray Shear Micromotion. *Proceedings of the Institution of Mechanical Engineers, Part H: Journal of Engineering in Medicine*, *219*(6), 449–456.

Beaupré, G. S., Orr, T. E., & Carter, D. R. (1990). An approach for time-dependent bone modeling and remodeling-theoretical development. *Journal of Orthopaedic Research*, *8*(5), 651–661.

Behery, O. A., Kearns, S. M., Rabinowitz, J. M., & Levine, B. R. (2017). Cementless vs Cemented Tibial Fixation in Primary Total Knee Arthroplasty. *The Journal of Arthroplasty*, *32*(5), 1510–1515.

Bercik, M. J., Joshi, A., & Parvizi, J. (2013). Posterior Cruciate-Retaining Versus Posterior-Stabilized Total Knee Arthroplasty. *The Journal of Arthroplasty*, *28*(3), 439–444.

Berend, M. E., Small, S. R., Ritter, M. A., & Buckley, C. A. (2010). The Effects of Bone Resection Depth and Malalignment on Strain in the Proximal Tibia After Total Knee Arthroplasty. *The Journal of Arthroplasty*, *25*(2), 314–318.

Berger, R. A., Lyon, J. H., Jacobs, J. J., Barden, R. M., Berkson, E. M., Sheinkop, M. B., Rosenberg, A. G., & Galante, J. O. (2001). Problems With Cementless Total Knee Arthroplasty at 11 Years Followup. *Clinical Orthopaedics and Related Research*, *392*, 196–207.

Berry, D. J., Currier, J. H., Mayor, M. B., & Collier, J. P. (2012). Knee Wear Measured in Retrievals: A Polished Tray Reduces Insert Wear. *Clinical Orthopaedics & Related Research*, *470*(7), 1860–1868.

Bertin, K. C. (2007). Tibial Component Fixation in Total Knee Arthroplasty. *The Journal of Arthroplasty*, *22*(5), 670–678.

Bhimji, S., & Meneghini, R. M. (2012). Micromotion of Cementless Tibial Baseplates Under Physiological Loading Conditions. *The Journal of Arthroplasty*, *27*(4), 648–654.

Bhimji, S., & Meneghini, R. M. (2014). Micromotion of Cementless Tibial Baseplates: Keels with Adjuvant Pegs Offer More Stability Than Pegs Alone. *The Journal of Arthroplasty*, *29*(7), 1503–1506.

Boulanaache, Y., Becce, F., Farron, A., Pioletti, D., & Terrier, A. (2020). Glenoid bone strain after anatomical total shoulder arthroplasty: In vitro measurements with micro-CT and digital volume correlation. *Medical Engineering & Physics*, *85*, 48–54.

Bozic, K. J., Kurtz, S. M., Lau, E., Ong, K., Chiu, V., Vail, T. P., Rubash, H. E., & Berry, D. J. (2010). The Epidemiology of Revision Total Knee Arthroplasty in the United States. *Clinical Orthopaedics & Related Research*, *468*(1), 45–51.

Bragdon, C. R., Burke, D., Lowenstein, J. D., O'Connor, D. O., Ramamurti, B., Jasty, M., & Harris, W. H. (1996). Differences in stiffness of the interface between a cementless porous implant and cancellous bone in vivo in dogs due to varying amounts of implant motion. *The Journal of Arthroplasty*, *11*(8), 945–951.

Burger, E. H., & Klein-Nulend, J. (1999). Mechanotransduction in bone—role of the lacunocanalicular network. *The FASEB Journal*, *13*(9001).

Callaghan, J. J., O'Rourke, M. R., & Saleh, K. J. (2004). Why knees fail. *The Journal of Arthroplasty*, *19*(4), 31–34.

Capella, M., Dolfin, M., & Saccia, F. (2016). Mobile bearing and fixed bearing total knee arthroplasty. *Annals of Translational Medicine*, *4*(7), 127.

Carlsson, K., Björkman, A., Besjakov, J., & ÖNsten, I. (2005). Cemented tibial component fixation performs better than cementless fixation. *Acta Orthopaedica*, *76*(3), 362–369.

Catelas, I., Wimmer, M. A., & Utzschneider, S. (2011). Polyethylene and metal wear particles: characteristics and biological effects. *Seminars in Immunopathology*, *33*(3), 257–271.

Cawley, D. T., Kelly, N., Simpkin, A., Shannon, F. J., & McGarry, J. P. (2012). Full and surface tibial cementation in total knee arthroplasty: A biomechanical investigation of stress distribution and remodeling in the tibia. *Clinical Biomechanics*, *27*(4), 390–397.

Cheng, M., Chen, D., Guo, Y., Zhu, C., & Zhang, X. (2013). Comparison of fixed- and mobile-bearing total knee arthroplasty with a mean five-year follow-up: A meta-analysis. *Experimental and Therapeutic Medicine*, *6*(1), 45–51.

Chong, D. Y. R., Hansen, U. N., & Amis, A. A. (2010). Analysis of bone–prosthesis interface micromotion for cementless tibial prosthesis fixation and the influence of loading conditions. *Journal of Biomechanics*, *43*(6), 1074–1080.

Chong, D. Y. R., Hansen, U. N., & Amis, A. A. (2011a). The influence of tibial prosthesis design features on stresses related to aseptic loosening and stress shielding. *Journal of Mechanics in Medicine and Biology*, *11*(01), 55–72.

Chong, D. Y. R., Hansen, U. N., & Amis, A. A. (2016). Cementless mis mini-keel prosthesis reduces interface micromotion versus standard stemmed tibial components. *Journal of Mechanics in Medicine and Biology*, *16*(05), 1650070.

Chong, D. Y. R., Hansen, U. N., van der Venne, R., Verdonschot, N., & Amis, A. A. (2011b). The influence of tibial component fixation techniques on resorption of

supporting bone stock after total knee replacement. *Journal of Biomechanics*, *44*(5), 948–954.

Colwell, C. W., Chen, P. C., & D'Lima, D. (2011). Extensor malalignment arising from femoral component malrotation in knee arthroplasty: Effect of rotating–bearing. *Clinical Biomechanics*, *26*(1), 52–57.

Completo, A., Fonseca, F., & Simões, J. (2008a). Strain shielding in proximal tibia of stemmed knee prosthesis: Experimental study. *Journal of Biomechanics*, *41*(3), 560–566.

Completo, A., Fonseca, F., & Simões, J. A. (2007). Finite Element and Experimental Cortex Strains of the Intact and Implanted Tibia. *Journal of Biomechanical Engineering*, *129*(5), 791–797.

Completo, A., Rego, A., Fonseca, F., Ramos, A., Relvas, C., & Simões, J. (2010). Biomechanical evaluation of proximal tibia behaviour with the use of femoral stems in revision TKA: An in vitro and finite element analysis. *Clinical Biomechanics*, *25*(2), 159–165.

Completo, A., Simões, J. A., & Fonseca, F. (2008b). Experimental Evaluation of Strain Shielding in Distal Femur in Revision TKA. *Experimental Mechanics*, *48*(6), 817–824.

Completo, A., Simões, J., Fonseca, F., & Oliveira, M. (2008c). The influence of different tibial stem designs in load sharing and stability at the cement–bone interface in revision TKA. *The Knee*, *15*(3), 227–232.

Completo, A., Talaia, P., Fonseca, F., & Simões, J. (2009). Relationship of design features of stemmed tibial knee prosthesis with stress shielding and end-of-stem pain. *Materials & Design*, *30*(4), 1391–1397.

Crook, P. D., Owen, J. R., Hess, S. R., Al-Humadi, S. M., Wayne, J. S., & Jiranek, W. A. (2017). Initial Stability of Cemented vs Cementless Tibial Components Under Cyclic Load. *The Journal of Arthroplasty*, *32*(8), 2556–2562.

Dalury, D. F. (2016). Cementless total knee arthroplasty. *The Bone & Joint Journal*, *98-B*(7), 867–873.

Dalury, D. F., Pomeroy, D. L., Gorab, R. S., & Adams, M. J. (2013). Why are Total Knee Arthroplasties Being Revised? *The Journal of Arthroplasty*, *28*(8), 120–121.

D'Anchise, R., Andreata, M., Balbino, C., & Manta, N. (2013). Posterior cruciate ligament-retaining and posterior-stabilized total knee arthroplasty: differences in surgical technique. *Joints*, *1*(1), 5–9.

de Ruiter, L., Rankin, K., Browne, M., Briscoe, A., Janssen, D., & Verdonschot, N. (2021). Decreased stress shielding with a PEEK femoral total knee prosthesis measured in validated computational models. *Journal of Biomechanics*, *118*, 110270.

De, S., Guilak, F., & Mofrad, M. (2010). *Computational Modeling in Biomechanics*. Springer Publishing.

DesJardins, J. D., Walker, P. S., Haider, H., & Perry, J. (2000). The use of a force-controlled dynamic knee simulator to quantify the mechanical performance of total knee replacement designs during functional activity. *Journal of Biomechanics*, *33*(10), 1231–1242.

Doblaré, M., & García, J. (2002). Anisotropic bone remodelling model based on a continuum damage-repair theory. *Journal of Biomechanics*, *35*(1), 1–17.

Dowd, J. E., Sychterz, C. J., Young, A. M., & Engh, C. A. (2000). Characterization of Long-Term Femoral-Head-Penetration Rates. *The Journal of Bone and Joint Surgery-American Volume*, *82*(8), 1102–1107.

Drees, P., Eckardt, A., Gay, R. E., Gay, S., & Huber, L. C. (2007). Mechanisms of Disease: molecular insights into aseptic loosening of orthopedic implants. *Nature Clinical Practice Rheumatology*, *3*(3), 165–171.

Duda, G. N., Heller, M., Albinger, J., Schulz, O., Schneider, E., & Claes, L. (1998). Influence of muscle forces on femoral strain distribution. *Journal of Biomechanics*, *31*(9), 841–846.

Duffy, G. P., Berry, D. J., & Rand, J. A. (1998). Cement Versus Cementless Fixation In Total Knee Arthroplasty. *Clinical Orthopaedics and Related Research*, *356*, 66–72.

Eberle, S., Göttlinger, M., & Augat, P. (2013). Individual density–elasticity relationships improve accuracy of subject-specific finite element models of human femurs. *Journal of Biomechanics*, *46*(13), 2152–2157.

Eidel, B., Gote, A., Fritzen, C. P., Ohrndorf, A., & Christ, H. J. (2020). Tibial implant fixation in TKA worth a revision?—how to avoid stress-shielding even for stiff metallic implants. *Computer Methods in Biomechanics and Biomedical Engineering*, *24*(3), 320–332.

Engh, C. A., O'Connor, D., Jasty, M., Mcgovern, T. F., Bobyn, J. D., & Harris, W. H. (1992). Quantification of Implant Micromotion, Strain Shielding, and Bone Resorption With Porous-Coated Anatomic Medullary Locking Femoral Prostheses. *Clinical Orthopaedics and Related Research*, *NA;*(285), 13???29.

Ersan, N., ÖZtürk, A., ÇAtma, M. F., ÜNlü, S., Akdoğan, M., & Ateş, Y. (2017). Total knee replacement—cementless tibial fixation with screws: 10-year results. *Acta Orthopaedica et Traumatologica Turcica*, *51*(6), 433–436.

Ertan Taskin, M., Zhang, T., Fraser, K. H., Griffith, B. P., & Wu, Z. J. (2012). Design Optimization of a Wearable Artificial Pump-Lung Device with Computational Modeling. *Journal of Medical Devices*, *6*(3).

Escamilla, R. F., MacLeod, T. D., Wilk, K. E., Paulos, L., & Andrews, J. R. (2012). Cruciate ligament loading during common knee rehabilitation exercises. *Proceedings of the Institution of Mechanical Engineers, Part H: Journal of Engineering in Medicine*, *226*(9), 670–680.

Fantozzi, S., Catani, F., Ensini, A., Leardini, A., & Giannini, S. (2006). Femoral rollback of cruciate-retaining and posterior-stabilized total knee replacements: In vivo fluoroscopic analysis during activities of daily living. *Journal of Orthopaedic Research*, *24*(12), 2222–2229.

Fehring, T. K., Odum, S., Griffin, W. L., Mason, J. B., & Nadaud, M. (2001). Early Failures in Total Knee Arthroplasty. *Clinical Orthopaedics and Related Research*, *392*, 315–318.

Fenech, C. M., & Keaveny, T. M. (1999). A Cellular Solid Criterion for Predicting the Axial-Shear Failure Properties of Bovine Trabecular Bone. *Journal of Biomechanical Engineering*, *121*(4), 414–422.

Fernandes, P., Rodrigues, H., & Jacobs, C. (1999). A Model of Bone Adaptation Using a Global Optimisation Criterion Based on the Trajectorial Theory of Wolff. *Computer Methods in Biomechanics and Biomedical Engineering*, *2*(2), 125–138.

Fitzpatrick, C. K., Baldwin, M. A., Clary, C. W., Maletsky, L. P., & Rullkoetter, P. J. (2012). Evaluating knee replacement mechanics during ADL with PID-controlled dynamic finite element analysis. *Computer Methods in Biomechanics and Biomedical Engineering*, *17*(4), 360–369.

Fitzpatrick, C. K., Maag, C., Clary, C. W., Metcalfe, A., Langhorn, J., & Rullkoetter, P. J. (2016). Validation of a new computational 6-DOF knee simulator during dynamic activities. *Journal of Biomechanics*, *49*(14), 3177–3184.

Frost, H. M. (1990). Skeletal structural adaptations to mechanical usage (SATMU): 1. Redefining Wolff's Law: The bone modeling problem. *The Anatomical Record*, *226*(4), 403–413.

Frost, H. M. (1992). Perspectives: The role of changes in mechanical usage set points in the pathogenesis of osteoporosis. *Journal of Bone and Mineral Research*, *7*(3), 253–261.

Gillard, F., Boardman, R., Mavrogordato, M., Hollis, D., Sinclair, I., Pierron, F., & Browne, M. (2014). The application of digital volume correlation (DVC) to study the microstructural behaviour of trabecular bone during compression. *Journal of the Mechanical Behavior of Biomedical Materials*, *29*, 480–499.

Gioe, T. J., Killeen, K. K., Grimm, K., Mehle, S., & Scheltema, K. (2004). Why Are Total Knee Replacements Revised? *Clinical Orthopaedics & Related Research*, *428*, 100–106.

Glenday, J. D., Wright, T. M., Lipman, J. D., Sculco, P. K., Mayman, D. J., Vigdorchik, J. M., & Quevedo-Gonzalez, F. J. (2021). Effect of varus alignment on the bone-implant interaction of a cementless tibial baseplate during gait. *Journal of Orthopaedic Research*. Published.

Glisson, R. R., Musgrave, D. S., Graham, R. D., & Vail, T. P. (2000). Validity of Photoelastic Strain Measurement on Cadaveric Proximal Femora. *Journal of Biomechanical Engineering*, *122*(4), 423–429.

Godest, A. C., Beaugonin, M., Haug, E., Taylor, M., & Gregson, P. (2002). Simulation of a knee joint replacement during a gait cycle using explicit finite element analysis. *Journal of Biomechanics*, *35*(2), 267–275.

Godest, A. C., Simonis De Cloke, C., Taylor, M., Gregson, P., Keane, A., Sathasivan, S., & Walker, P. (2000). A computational model for the prediction of total knee replacement kinematics in the sagittal plane. *Journal of Biomechanics*, *33*(4), 435–442.

González, O., Smith, R. L., & Goodman, S. B. (1996). Effect of size, concentration, surface area, and volume of polymethylmethacrylate particles on human macrophagesin vitro. *Journal of Biomedical Materials Research*, *30*(4), 463–473.

Grassi, L., & Isaksson, H. (2015). Extracting accurate strain measurements in bone mechanics: A critical review of current methods. *Journal of the Mechanical Behavior of Biomedical Materials*, *50*, 43–54.

Green, G. V., Berend, K. R., Berend, M. E., Glisson, R. R., & Vail, T. P. (2002). The effects of varus tibial alignment on proximal tibial surface strain in total knee arthroplasty. *The Journal of Arthroplasty*, *17*(8), 1033–1039.

Grood, E. S., & Suntay, W. J. (1983). A Joint Coordinate System for the Clinical Description of Three-Dimensional Motions: Application to the Knee. *Journal of Biomechanical Engineering*, *105*(2), 136–144.

Guccione, J. M., Kassab, G. S., & Ratcliffe, M. (2010). *Computational Cardiovascular Mechanics*. Springer Publishing.

Halloran, J. P., Clary, C. W., Maletsky, L. P., Taylor, M., Petrella, A. J., & Rullkoetter, P. J. (2010). Verification of Predicted Knee Replacement Kinematics During Simulated Gait in the Kansas Knee Simulator. *Journal of Biomechanical Engineering*, *132*(8).

Halloran, J. P., Petrella, A. J., & Rullkoetter, P. J. (2005). Explicit finite element modeling of total knee replacement mechanics. *Journal of Biomechanics*, *38*(2), 323–331.

Han, S., Patel, R. V., Ismaily, S. K., Jones, H. L., Gold, J. E., & Noble, P. C. (2021). Micromotion and Migration of Cementless Tibial Trays Under Functional Loading Conditions. *The Journal of Arthroplasty*, *36*(1), 349–355.

Harris, W., Schiller, A., Scholler, J., Freiberg, R., & Scott, R. (1976). Extensive localized bone resorption in the femur following total hip replacement. *The Journal of Bone & Joint Surgery*, *58*(5), 612–618.

Hashemi, A., & Shirazi-adl, A. (2000). Finite Element Analysis of Tibial Implants — Effect of Fixation Design and Friction Model. *Computer Methods in Biomechanics and Biomedical Engineering*, *3*(3), 183–201.

Heilemann, M., Wendler, T., Münst, P., Schleifenbaum, S., Scholz, R., & Voigt, C. (2020). A novel micromotion measurement method to gain instructive insight into the acetabular bone-implant interface. *Medical Engineering & Physics*, *86*, 138–145.

Henninger, H. B., Reese, S. P., Anderson, A. E., & Weiss, J. A. (2009). Validation of computational models in biomechanics. *Proceedings of the Institution of Mechanical Engineers, Part H: Journal of Engineering in Medicine*, *224*(7), 801–812.

Hensler, D., Musahl, V., Illingworth, K. D., Thorhauer, E. D., & Tashman, S. (2012, February). *The function of the two bundles of the posterior cruciate ligament –an in-vivo study using dynamic stereo X-ray system (DSX)* [Poster No. 2297]. ORS Annual Meeting, San Francisco, California.

Hillam, R. A., Goodship, A. E., & Skerry, T. M. (2015). Peak strain magnitudes and rates in the tibia exceed greatly those in the skull: An in vivo study in a human subject. *Journal of Biomechanics*, *48*(12), 3292–3298.

Hofmann, A. A., Heithoff, S. M., & Camargo, M. (2002). Cementless Total Knee Arthroplasty in Patients 50 Years or Younger. *Clinical Orthopaedics and Related Research*, *404*, 102–107.

Hoshaw, S., Fyhrie, D., Takano, Y., Burr, D., & Milgrom, C. (1997). A method suitable for in vivo measurement of bone strain in humans. *Journal of Biomechanics*, *30*(5), 521–524.

Hossain, F., Patel, S., & Haddad, F. S. (2010). Midterm Assessment of Causes and Results of Revision Total Knee Arthroplasty. *Clinical Orthopaedics & Related Research*, *468*(5), 1221–1228.

Howell, S. M., Howell, S. J., Kuznik, K. T., Cohen, J., & Hull, M. L. (2013). Does A Kinematically Aligned Total Knee Arthroplasty Restore Function Without Failure Regardless of Alignment Category? *Clinical Orthopaedics & Related Research*, *471*(3), 1000–1007.

Howie, D. W., Vernon-Roberts, B., Oakeshott, R., & Manthey, B. (1988). A rat model of resorption of bone at the cement-bone interface in the presence of polyethylene wear particles. *The Journal of Bone & Joint Surgery*, *70*(2), 257–263.

Huiskes, R., Weinans, H., Grootenboer, H., Dalstra, M., Fudala, B., & Slooff, T. (1987). Adaptive bone-remodeling theory applied to prosthetic-design analysis. *Journal of Biomechanics*, *20*(11–12), 1135–1150.

Ibrahim, H., Esfahani, S. N., Poorganji, B., Dean, D., & Elahinia, M. (2017). Resorbable bone fixation alloys, forming, and post-fabrication treatments. *Materials Science and Engineering: C*, *70*, 870–888.

Ingham, E., & Fisher, J. (2000). Biological reactions to wear debris in total joint replacement. *Proceedings of the Institution of Mechanical Engineers, Part H: Journal of Engineering in Medicine*, *214*(1), 21–37.

Innocenti, B., Truyens, E., Labey, L., Wong, P., Victor, J., & Bellemans, J. (2009). Can medio-lateral baseplate position and load sharing induce asymptomatic local bone resorption of the proximal tibia? A finite element study. *Journal of Orthopaedic Surgery and Research*, *4*(1).

Jang, I. G., Kim, I. Y., & Kwak, B. M. (2008). Analogy of Strain Energy Density Based Bone-Remodeling Algorithm and Structural Topology Optimization. *Journal of Biomechanical Engineering*, *131*(1).

Jasty, M., Bragdon, C., Burke, D., O'Connor, D., Lowenstein, J., & Harris, W. H. (1997). In Vivo Skeletal Responses to Porous-Surfaced Implants Subjected to Small Induced Motions*. *The Journal of Bone and Joint Surgery (American Volume)*, *79*(5), 707–714.

Jasty, M., Bragdon, C. R., Zalenski, E., O'Connor, D., Page, A., & Harris, W. H. (1997). Enhanced stability of uncemented canine femoral components by bone ingrowth into the porous coatings. *The Journal of Arthroplasty*, *12*(1), 106–113.

Jia, Z., Gong, H., Hu, S., Fang, J., & Fan, R. (2017). Influence of design features of tibial stems in total knee arthroplasty on tibial bone remodeling behaviors. *Medical Engineering & Physics*, *48*, 103–113.

Johanson, P. E., Digas, G., Herberts, P., Thanner, J., & Kärrholm, J. (2012). Highly Crosslinked Polyethylene Does Not Reduce Aseptic Loosening in Cemented THA 10-year Findings of a Randomized Study. *Clinical Orthopaedics & Related Research*, *470*(11), 3083–3093.

Jones, M. D., & Buckle, C. L. (2020). How does aseptic loosening occur and how can we prevent it? *Orthopaedics and Trauma*, *34*(3), 146–152.

Justine, M., & Ibrahim, A. (2019). Physiotherapy Approach in Improving Knee Function Following Total Knee Replacement: A Case Report. *Indian Journal of Physiotherapy and Occupational Therapy - An International Journal*, *13*(2), 90–94.

Kaczmarczyk, Ł., & Pearce, C. (2011). Efficient numerical analysis of bone remodelling. *Journal of the Mechanical Behavior of Biomedical Materials*, *4*(6), 858–867.

Kaneko, T. S., Bell, J. S., Pejcic, M. R., Tehranzadeh, J., & Keyak, J. H. (2004). Mechanical properties, density and quantitative CT scan data of trabecular bone with and without metastases. *Journal of Biomechanics*, *37*(4), 523–530.

Kasahara, Y., Majima, T., Kimura, S., Nishiike, O., & Uchida, J. (2013). What Are the Causes of Revision Total Knee Arthroplasty in Japan? *Clinical Orthopaedics & Related Research*, *471*(5), 1533–1538.

Keane, A., & Nair, P. (2005). *Computational Approaches for Aerospace Design: The Pursuit of Excellence* (1st ed.). Wiley.

Keyak, J. H., Lee, I. Y., & Skinner, H. B. (1994). Correlations between orthogonal mechanical properties and density of trabecular bone: Use of different densitometric measures. *Journal of Biomedical Materials Research*, *28*(11), 1329–1336.

Kienapfel, H., Sprey, C., Wilke, A., & Griss, P. (1999). Implant fixation by bone ingrowth. *The Journal of Arthroplasty*, *14*(3), 355–368.

Kim, Y. H., Choi, Y., & Kim, J. S. (2010). Osteolysis in Well-functioning Fixed- and Mobile-bearing TKAs in Younger Patients. *Clinical Orthopaedics & Related Research*, *468*(11), 3084–3093.

Kim, Y. H., Park, J. W., & Kim, J. S. (2016). A Comparison of 5 Models of Total Knee Arthroplasty in Young Patients. *The Journal of Arthroplasty*, *31*(5), 994–999.

Kim, Y. H., Park, J. W., Lim, H. M., & Park, E. S. (2014). Cementless and cemented total knee arthroplasty in patients younger than fifty-five years. Which is better? *International Orthopaedics*, *38*(2), 297–303.

Knight, L. A., Pal, S., Coleman, J. C., Bronson, F., Haider, H., Levine, D. L., Taylor, M., & Rullkoetter, P. J. (2007). Comparison of long-term numerical and experimental total knee replacement wear during simulated gait loading. *Journal of Biomechanics*, *40*(7), 1550–1558.

Ko, D. O., Lee, S., Kim, K. T., Lee, J. I., Kim, J. W., & Yi, S. M. (2017). Cement Mantle Thickness at the Bone Cement Interface in Total Knee Arthroplasty: Comparison of PS150 RP and LPS-Flex Knee Implants. *Knee Surgery & Related Research*, *29*(2), 115–121.

Kolisek, F. R., McGrath, M. S., Marker, D. R., Jessup, N., Seyler, T. M., Mont, M. A., & Lowry Barnes, C. (2009). Posterior-stabilized versus posterior cruciate ligament-retaining total knee arthroplasty. *The Lowa Orthopaedic Journal*, *29*, 23–27.

Komistek, R. D., Kane, T. R., Mahfouz, M., Ochoa, J. A., & Dennis, D. A. (2005). Knee mechanics: a review of past and present techniques to determine in vivo loads. *Journal of Biomechanics*, *38*(2), 215–228.

Kraemer, W. J., Harrington, I. J., & Hearn, T. C. (1995). Micromotion secondary to axial, torsional, and shear loads in two models of cementless tibial components. *The Journal of Arthroplasty*, *10*(2), 227–235.

Kung, E., Farahmand, M., & Gupta, A. (2019). A Hybrid Experimental-Computational Modeling Framework for Cardiovascular Device Testing. *Journal of Biomechanical Engineering*, *141*(5).

Kuperman, E. F., Schweizer, M., Joy, P., Gu, X., & Fang, M. M. (2016). The effects of advanced age on primary total knee arthroplasty: a meta-analysis and systematic review. *BMC Geriatrics*, *16*(1).

Kurtz, S. M. (2009). *UHMWPE Biomaterials Handbook: Ultra High Molecular Weight Polyethylene in Total Joint Replacement and Medical Devices (Plastics Design Library)* (2nd ed.). Academic Press.

Kurtz, S. M., Lau, E., Ong, K., Zhao, K., Kelly, M., & Bozic, K. J. (2009). Future Young Patient Demand for Primary and Revision Joint Replacement: National Projections from 2010 to 2030. *Clinical Orthopaedics & Related Research*, *467*(10), 2606–2612.

Kurtz, S. M., Ong, K., Lau, E., Mowat, F., & Halpern, M. (2007). Projections of Primary and Revision Hip and Knee Arthroplasty in the United States from 2005 to 2030. *The Journal of Bone & Joint Surgery*, *89*(4), 780–785.

Kutzner, I., Heinlein, B., Graichen, F., Bender, A., Rohlmann, A., Halder, A., Beier, A., & Bergmann, G. (2010). Loading of the knee joint during activities of daily living measured in vivo in five subjects. *Journal of Biomechanics*, *43*(11), 2164–2173.

Lanyon, L. E., Hampson, W. G. J., Goodship, A. E., & Shah, J. S. (1975). Bone Deformation Recorded in vivo from Strain Gauges Attached to the Human Tibial Shaft. *Acta Orthopaedica Scandinavica*, *46*(2), 256–268.

Le, D. H., Goodman, S. B., Maloney, W. J., & Huddleston, J. I. (2014). Current Modes of Failure in TKA: Infection, Instability, and Stiffness Predominate. *Clinical Orthopaedics & Related Research*, *472*(7), 2197–2200.

Leichtenberg, C. S., Vliet Vlieland, T. P. M., Kroon, H. M., Dekker, J., Marijnissen, W. J., Damen, P. J., Nelissen, R. G. H. H., & van der Esch, M. (2018). Self-reported knee instability associated with pain, activity limitations, and poorer quality of life before and 1 year after total knee arthroplasty in patients with knee osteoarthritis. *Journal of Orthopaedic Research®*, *36*(10), 2671–2678.

Linde, F., Hvid, I., & Madsen, F. (1991). The effect of specimen size and geometry on the mechanical behaviour of trabecular bone specimens. *Journal of Biomechanics*, *24*(6), 454.

Linde, F., Pongsoipetch, B., Frich, L. H., & Hvid, I. (1990). Three-axial strain controlled testing applied to bone specimens from the proximal tibial epiphysis. *Journal of Biomechanics*, *23*(11), 1167–1172.

Lonner, J. H., Klotz, M., Levitz, C., & Lotke, P. A. (2001). Changes in bone density after cemented total knee arthroplasty. *The Journal of Arthroplasty*, *16*(1), 107–111.

Makhdom, A. M., & Parvizi, J. (2017). Modular versus nonmodular tibial inserts in total knee arthroplasty: what are the differences? *Annals of Translational Medicine*, *5*(10), 225.

Maletsky, L. P., & Hillberry, B. M. (2005). Simulating Dynamic Activities Using a Five-Axis Knee Simulator. *Journal of Biomechanical Engineering*, *127*(1), 123–133.

Malfroy Camine, V., Rüdiger, H., Pioletti, D., & Terrier, A. (2016). Full-field measurement of micromotion around a cementless femoral stem using micro-CT imaging and radiopaque markers. *Journal of Biomechanics*, *49*(16), 4002–4008.

Malinzak, R. A., Small, S. R., Rogge, R. D., Archer, D. B., Oja, J. W., Berend, M. E., & Ritter, M. A. (2014). The Effect of Rotating Platform TKA on Strain Distribution and Torque Transmission on the Proximal Tibia. *The Journal of Arthroplasty*, *29*(3), 541–547.

Malony, W. J., & Smith, R. L. (1995). Periprosthetic Osteolysis in Total Hip Arthroplasty. *The Journal of Bone & Joint Surgery*, *77*(9), 1448–1461.

Markolf, K. L., Gorek, J. F., Kabo, J. M., & Shapiro, M. S. (1990). Direct measurement of resultant forces in the anterior cruciate ligament. An in vitro study performed with

a new experimental technique. *The Journal of Bone & Joint Surgery*, *72*(4), 557–567.

Martin, J. R., Watts, C. D., Levy, D. L., Miner, T. M., Springer, B. D., & Kim, R. H. (2017). Tibial Tray Thickness Significantly Increases Medial Tibial Bone Resorption in Cobalt–Chromium Total Knee Arthroplasty Implants. *The Journal of Arthroplasty*, *32*(1), 79–82.

Martin, S., Saurez, A., Ismaily, S., Ashfaq, K., Noble, P., & Incavo, S. J. (2014). Maximizing Tibial Coverage Is Detrimental to Proper Rotational Alignment. *Clinical Orthopaedics & Related Research*, *472*(1), 121–125.

Maruyama, S., Yoshiya, S., Matsui, N., Kuroda, R., & Kurosaka, M. (2004). Functional comparison of posterior cruciate-retaining versus posterior stabilized total knee arthroplasty. *The Journal of Arthroplasty*, *19*(3), 349–353.

Meftah, M., White, P. B., Ranawat, A. S., & Ranawat, C. S. (2016). Long-term results of total knee arthroplasty in young and active patients with posterior stabilized design. *The Knee*, *23*(2), 318–321.

Meneghini, R., Daluga, A., & Soliman, M. (2011). Mechanical Stability of Cementless Tibial Components in Normal and Osteoporotic Bone. *Journal of Knee Surgery*, *24*(03), 191–196.

Meneghini, R., & Hanssen, A. (2008). Cementless Fixation in Total Knee Arthroplasty – Past, Present, and Future. *Journal of Knee Surgery*, *21*(04), 307–314.

Milgrom, C. (2000). Do high impact exercises produce higher tibial strains than running? *British Journal of Sports Medicine*, *34*(3), 195–199.

Mirulla, A. I., Pinelli, S., Zaffagnini, S., Nigrelli, V., Ingrassia, T., Paolo, S. D., & Bragonzoni, L. (2021). Numerical simulations on periprosthetic bone remodeling: a systematic review. *Computer Methods and Programs in Biomedicine*, *204*, 106072.

Morgan, E. F., Bayraktar, H. H., & Keaveny, T. M. (2003). Trabecular bone modulus–density relationships depend on anatomic site. *Journal of Biomechanics*, *36*(7), 897–904.

Morris, B. A., D'Lima, D. D., Slamin, J., Kovacevic, N., Arms, S. W., Townsend, C. P., & Colwell, C. W. (2001). e-Knee: Evolution of the Electronic Knee Prosthesis. *The Journal of Bone and Joint Surgery-American Volume*, *83*, 62–66.

Moskal, J. T., & Capps, S. G. (2014). Rotating-platform TKA No Different from Fixed-bearing TKA Regarding Survivorship or Performance: A Meta-analysis. *Clinical Orthopaedics & Related Research*, *472*(7), 2185–2193.

Mueller, J. K., Bischoff, J., Siggelkow, E., Parduhn, C., Roach, B., Drury, N., & Bandi, M. (2020). Micromotion of cruciate-retaining and posterior-stabilized cementless total knee arthroplasty designs during two activities: an experimental chapter. *Orthopaedic Proceedings*, 102-B: SUPP_2, 20

Munro, J. T., Pandit, S., Walker, C. G., Clatworthy, M., & Pitto, R. P. (2010). Loss of Tibial Bone Density in Patients with Rotating- or Fixed-platform TKA. *Clinical Orthopaedics & Related Research*, *468*(3), 775–781.

Nakamura, S., Tian, Y., Tanaka, Y., Kuriyama, S., Ito, H., Furu, M., & Matsuda, S. (2017). The effects of kinematically aligned total knee arthroplasty on stress at the medial tibia. *Bone & Joint Research*, *6*(1), 43–51.

Naudie, D. D., Ammeen, D. J., Engh, G. A., & Rorabeck, C. H. (2007). Wear and Osteolysis Around Total Knee Arthroplasty. *Journal of the American Academy of Orthopaedic Surgeons*, *15*(1), 53–64.

Navacchia, A., Clary, C. W., Wilson, H. L., Behnam, Y. A., & Rullkoetter, P. J. (2018). Validation of model-predicted tibial tray-synthetic bone relative motion in cementless total knee replacement during activities of daily living. *Journal of Biomechanics*, *77*, 115–123.

Navacchia, A., Sintini, I., Clary, C. W., & Rullkoetter, P. J. (2018, October). *Effects of TKR alignment, implant design and patient pre-operative alignment on post-operative proximal tibia strain* [Podium presentation]. ISTA, London, UK.

Newman, J. M., Sodhi, N., Dekis, J. C., Khlopas, A., Piuzzi, N. S., Sultan, A. A., Levin, J. M., & Mont, M. A. (2019). Survivorship and Functional Outcomes of Cementless versus Cemented Total Knee Arthroplasty: A Meta-Analysis. *The Journal of Knee Surgery*, *33*(03), 270–278.

Newman, J. M., Sodhi, N., Khlopas, A., Sultan, A. A., Chughtai, M., Abraham, R., Oh, J., Molloy, R. M., Harwin, S. F., & Mont, M. A. (2018). Cementless Total Knee Arthroplasty: A Comprehensive Review of the Literature. *Orthopedics*, *41*(5), 263–273.

Niki, Y., Nagura, T., Nagai, K., Kobayashi, S., & Harato, K. (2017). Kinematically aligned total knee arthroplasty reduces knee adduction moment more than mechanically aligned total knee arthroplasty. *Knee Surgery, Sports Traumatology, Arthroscopy*, *26*(6), 1629–1635.

Nilsson, K. G., Henricson, A., Norgren, B., & Dal??N, T. (2006). Uncemented HA-coated Implant is the Optimum Fixation for TKA in the Young Patient. *Clinical Orthopaedics and Related Research*, *448*, 129–139.

Noble, P., Gold, J., Patel, R., Lenherr, C., Jones, H., Ismaily, S., & Alexander, J. (2017). Which activities generate the greatest tibial interface micromotion in cementless TKA? *Orthopaedic Proceedings*, 99-B: SUPP_5, 57

Norman, T. L., Ackerman, E. S., Smith, T. S., Gruen, T. A., Yates, A. J., Blaha, J. D., & Kish, V. L. (2005). Cortical Bone Viscoelasticity and Fixation Strength of Press-Fit Femoral Stems: An In-Vitro Model. *Journal of Biomechanical Engineering*, *128*(1), 13–17.

Nyman, J. S., Rodrigo, J. J., Hazelwood, S. J., Yeh, O. C., & Martin, R. B. (2006). Predictions on Preserving Bone Mass in Knee Arthroplasty With Bisphosphonates. *The Journal of Arthroplasty*, *21*(1), 106–113.

Olson, S. A., Marsh, J. L., Anderson, D. D., & Latta, PE, L. L. (2012). Designing a Biomechanics Investigation. *Journal of Orthopaedic Trauma*, *26*(12), 672–677.

Pal, S., Haider, H., Laz, P. J., Knight, L. A., & Rullkoetter, P. J. (2008). Probabilistic computational modeling of total knee replacement wear. *Wear*, *264*(7–8), 701–707.

Paulo Davim, J. (2012). *Computational Methods for Optimizing Manufacturing Technology: Models and Techniques* (1st ed.). IGI Global.

Perillo-Marcone, A., & Taylor, M. (2006). Effect of Varus/Valgus Malalignment on Bone Strains in the Proximal Tibia After TKR: An Explicit Finite Element Study. *Journal of Biomechanical Engineering*, *129*(1), 1–11.

Pettersen, S. H., Wik, T. S., & Skallerud, B. (2009). Subject specific finite element analysis of implant stability for a cementless femoral stem. *Clinical Biomechanics*, *24*(6), 480–487.

Pfitzner, T., Moewis, P., Stein, P., Boeth, H., Trepczynski, A., von Roth, P., & Duda, G. N. (2017). Modifications of femoral component design in multi-radius total knee arthroplasty lead to higher lateral posterior femoro-tibial translation. *Knee Surgery, Sports Traumatology, Arthroscopy*, *26*(6), 1645–1655.

Pietrzyk, M., Madej, L., Rauch, L., & Szeliga, D. (2016). *Computational Materials Engineering: Achieving High Accuracy and Efficiency in Metals Processing Simulations*. Butterworth-Heinemann.

Pilliar, R. M., Lee, J. M., & Maniatopoulos, C. (1986). Observations on the Effect of Movement on Bone Ingrowth into Porous-Surfaced Implants. *Clinical Orthopaedics and Related Research, NA;*(208), 108???113.

Pitta, M., Esposito, C. I., Li, Z., Lee, Y. Y., Wright, T. M., & Padgett, D. E. (2018). Failure After Modern Total Knee Arthroplasty: A Prospective Study of 18,065 Knees. *The Journal of Arthroplasty*, *33*(2), 407–414.

Plaskos, C., Hodgson, A. J., Inkpen, K., & McGraw, R. W. (2002). Bone cutting errors in total knee arthroplasty. *The Journal of Arthroplasty*, *17*(6), 698–705.

Pour, A. E., Parvizi, J., Slenker, N., Purtill, J. J., & Sharkey, P. F. (2007). Rotating Hinged Total Knee Replacement. *The Journal of Bone & Joint Surgery*, *89*(8), 1735–1741.

Prendergast, P. (1997). Finite element models in tissue mechanics and orthopaedic implant design. *Clinical Biomechanics*, *12*(6), 343–366.

Quilez, M. P., Seral, B., & Pérez, M. A. (2017). Biomechanical evaluation of tibial bone adaptation after revision total knee arthroplasty: A comparison of different implant systems. *PLOS ONE*, *12*(9), e0184361.

Rahimizadeh, A., Nourmohammadi, Z., Arabnejad, S., Tanzer, M., & Pasini, D. (2018). Porous architected biomaterial for a tibial-knee implant with minimum bone resorption and bone-implant interface micromotion. *Journal of the Mechanical Behavior of Biomedical Materials*, *78*, 465–479.

Rankin, K. E., Dickinson, A. S., Briscoe, A., & Browne, M. (2016). Does a PEEK Femoral TKA Implant Preserve Intact Femoral Surface Strains Compared With CoCr? A Preliminary Laboratory Study. *Clinical Orthopaedics & Related Research*, *474*(11), 2405–2413.

Rawlinson, J. J., Peters, L. E., Campbell, D. A., Windsor, R., Wright, T. M., & Bartel, D. L. (2005). Cancellous Bone Strains Indicate Efficacy of Stem Augmentation in Constrained Condylar Knees. *Clinical Orthopaedics and Related Research*, *440*(NA;), 107–116.

Reggiani, B., Cristofolini, L., Varini, E., & Viceconti, M. (2007). Predicting the subject-specific primary stability of cementless implants during pre-operative planning: Preliminary validation of subject-specific finite-element models. *Journal of Biomechanics*, *40*(11), 2552–2558.

Research, I. (2018, July 18). *Total Knee Replacement Statistics 2017: Younger Patients Driving Growth*. IData Research.

Rho, J., Hobatho, M., & Ashman, R. (1995). Relations of mechanical properties to density and CT numbers in human bone. *Medical Engineering & Physics*, *17*(5), 347–355.

Riddle, D. L., Jiranek, W. A., & McGlynn, F. J. (2008). Yearly Incidence of Unicompartmental Knee Arthroplasty in the United States. *The Journal of Arthroplasty*, *23*(3), 408–412.

Ruimerman, R., van Rietbergen, B., Hilbers, P., & Huiskes, R. (2005). The Effects of Trabecular-Bone Loading Variables on the Surface Signaling Potential for Bone Remodeling and Adaptation. *Annals of Biomedical Engineering*, *33*(1), 71–78.

Rullkoetter, P. J., Fitzpatrick, C. K., & Clary, C. W. (2017). How Can We Use Computational Modeling to Improve Total Knee Arthroplasty? Modeling Stability and Mobility in the Implanted Knee. *Journal of the American Academy of Orthopaedic Surgeons*, *25*, S33–S39.

Sabokbar, A., Pandey, R., & Athanasou, N. A. (2003). The effect of particle size and electrical charge on macrophage-osteoclast differentiation and bone resorption. *Journal of Materials Science: Materials in Medicine*, *14*(9), 731–738.

Samui, P., Chakraborty, S., & Kim, D. (2016). *Modeling and Simulation Techniques in Structural Engineering (Advances in Civil and Industrial Engineering)* (1st ed.). IGI Global.

Sappey-Marinier, E., Pauvert, A., Batailler, C., Swan, J., Cheze, L., Servien, E., & Lustig, S. (2020a). Kinematic versus mechanical alignment for primary total knee arthroplasty with minimum 2 years follow-up: a systematic review. *SICOT-J*, *6*, 18.

Sappey-Marinier, E., Pauvert, A., Batailler, C., Swan, J., Cheze, L., Servien, E., & Lustig, S. (2020b). Kinematic versus mechanical alignment for primary total knee arthroplasty with minimum 2 years follow-up: a systematic review. *SICOT-J*, *6*, 18.

Schai, P. A., Thornhill, T. S., & Scott, R. D. (1998). Total knee arthroplasty with the PFC system. *The Journal of Bone and Joint Surgery. British Volume*, *80-B*(5), 850–858.

Schroer, W. C., Berend, K. R., Lombardi, A. V., Barnes, C. L., Bolognesi, M. P., Berend, M. E., Ritter, M. A., & Nunley, R. M. (2013). Why Are Total Knees Failing Today? Etiology of Total Knee Revision in 2010 and 2011. *The Journal of Arthroplasty*, *28*(8), 116–119.

Scott, C. E. H., & Biant, L. C. (2012). The role of the design of tibial components and stems in knee replacement. *The Journal of Bone and Joint Surgery. British Volume*, *94-B*(8), 1009–1015.

Scott, C. E. H., Eaton, M. J., Nutton, R. W., Wade, F. A., Pankaj, P., & Evans, S. L. (2013). Proximal tibial strain in medial unicompartmental knee replacements. *The Bone & Joint Journal*, *95-B*(10), 1339–1347.

Shanbhag, A., Jacobs, J., Glant, T., Gilbert, J., Black, J., & Galante, J. (1994). Composition and morphology of wear debris in failed uncemented total hip replacement. *The Journal of Bone and Joint Surgery. British Volume*, *76-B*(1), 60–67.

Shanbhag, A. S., Bailey, H. O., Hwang, D. S., Cha, C. W., Eror, N. G., & Rubash, H. E. (2000). Quantitative analysis of ultrahigh molecular weight polyethylene (UHMWPE) wear debris associated with total knee replacements. *Journal of Biomedical Materials Research*, *53*(1), 100–110.

Sharkey, P. F., Hozack, W. J., Rothman, R. H., Shastri, S., & Jacoby, S. M. (2002). Why Are Total Knee Arthroplasties Failing Today? *Clinical Orthopaedics and Related Research*, *404*, 7–13.

Sharkey, P. F., Lichstein, P. M., Shen, C., Tokarski, A. T., & Parvizi, J. (2014). Why Are Total Knee Arthroplasties Failing Today—Has Anything Changed After 10 Years? *The Journal of Arthroplasty*, *29*(9), 1774–1778.

Shifani, S., Nanammal, V., Bhavani, R., & Nishidha, A. A. (2017). A Review on Strain Measurement in Bone Mechanics Using Various Techniques. *2017 IEEE International Conference on Computational Intelligence and Computing Research (ICCIC)*. Published.

Shirazi-Adl, A., Dammak, M., & Zukor, D. (1994). Fixation pull-out response measurement of bone screws and porous-surfaced posts. *Journal of Biomechanics*, *27*(10), 1249–1258.

Shultz, T. R., Blaha, J. D., Gruen, T. A., & Norman, T. L. (2005). Cortical Bone Viscoelasticity and Fixation Strength of Press-Fit Femoral Stems: A Finite Element Model. *Journal of Biomechanical Engineering*, *128*(1), 7–12.

Simpson, D., Price, A., Gulati, A., Murray, D., & Gill, H. (2009). Elevated proximal tibial strains following unicompartmental knee replacement—A possible cause of pain. *Medical Engineering & Physics*, *31*(7), 752–757.

Sloan, M., Premkumar, A., & Sheth, N. P. (2018). Projected Volume of Primary Total Joint Arthroplasty in the U.S., 2014 to 2030. *Journal of Bone and Joint Surgery*, *100*(17), 1455–1460.

Small, S. R., Berend, M. E., Ritter, M. A., & Buckley, C. A. (2010). A Comparison in Proximal Tibial Strain Between Metal-Backed and All-Polyethylene Anatomic Graduated Component Total Knee Arthroplasty Tibial Components. *The Journal of Arthroplasty*, *25*(5), 820–825.

Small, S. R., Rogge, R. D., Malinzak, R. A., Reyes, E. M., Cook, P. L., Farley, K. A., & Ritter, M. A. (2016). Micromotion at the tibial plateau in primary and revision total knee arthroplasty: fixed versus rotating platform designs. *Bone & Joint Research*, *5*(4), 122–129.

Small, S. R., Rogge, R. D., Reyes, E. M., Seale, R. B., Elliott, J. B., & Malinzak, R. A. (2019). Primary Stability in Cementless Rotating Platform Total Knee Arthroplasty. *The Journal of Knee Surgery*, *34*(02), 192–199.

Smith, C. R., Vignos, M. F., Lenhart, R. L., Kaiser, J., & Thelen, D. G. (2016). The Influence of Component Alignment and Ligament Properties on Tibiofemoral

Contact Forces in Total Knee Replacement. *Journal of Biomechanical Engineering*, *138*(2).

Smoger, L. M., Shelburne, K. B., Cyr, A. J., Rullkoetter, P. J., & Laz, P. J. (2017). Statistical shape modeling predicts patellar bone geometry to enable stereo-radiographic kinematic tracking. *Journal of Biomechanics*, *58*, 187–194.

Snyder, S. M., & Schneider, E. (1991). Estimation of mechanical properties of cortical bone by computed tomography. *Journal of Orthopaedic Research*, *9*(3), 422–431.

Soininvaara, T. A., Miettinen, H. J., Jurvelin, J. S., Suomalainen, O. T., Alhava, E. M., & Kröger, H. P. (2004). Periprosthetic femoral bone loss after total knee arthroplasty: 1-year follow-up study of 69 patients. *The Knee*, *11*(4), 297–302.

Sopher, R. S., Amis, A. A., Calder, J. D., & Jeffers, J. R. (2017). Total ankle replacement design and positioning affect implant-bone micromotion and bone strains. *Medical Engineering & Physics*, *42*, 80–90.

Srinivasan, P., Miller, M. A., Verdonschot, N., Mann, K. A., & Janssen, D. (2016). Experimental and computational micromechanics at the tibial cement-trabeculae interface. *Journal of Biomechanics*, *49*(9), 1641–1648.

Srinivasan, P., Miller, M. A., Verdonschot, N., Mann, K. A., & Janssen, D. (2017). Strain shielding in trabecular bone at the tibial cement-bone interface. *Journal of the Mechanical Behavior of Biomedical Materials*, *66*, 181–186.

Sukjamsri, C., Geraldes, D. M., Gregory, T., Ahmed, F., Hollis, D., Schenk, S., Amis, A., Emery, R., & Hansen, U. (2015). Digital volume correlation and micro-CT: An in-vitro technique for measuring full-field interface micromotion around polyethylene implants. *Journal of Biomechanics*, *48*(12), 3447–3454.

Sundfeldt, M., V Carlsson, L., B Johansson, C., Thomsen, P., & Gretzer, C. (2006). Aseptic loosening, not only a question of wear: A review of different theories. *Acta Orthopaedica*, *77*(2), 177–197.

Taylor, M., Barrett, D. S., & Deffenbaugh, D. (2012). Influence of loading and activity on the primary stability of cementless tibial trays. *Journal of Orthopaedic Research*, *30*(9), 1362–1368.

Taylor, M., & Prendergast, P. J. (2015). Four decades of finite element analysis of orthopaedic devices: Where are we now and what are the opportunities? *Journal of Biomechanics*, *48*(5), 767–778.

Taylor, S., Walker, P., Perry, J., Cannon, S., & Woledge, R. (1998). The forces in the distal femur and the knee during walking and other activities measured by telemetry. *The Journal of Arthroplasty*, *13*(4), 428–437.

Thiele, K., Perka, C., Matziolis, G., Mayr, H. O., Sostheim, M., & Hube, R. (2015). Current Failure Mechanisms After Knee Arthroplasty Have Changed: Polyethylene Wear Is Less Common in Revision Surgery. *The Journal of Bone and Joint Surgery-American Volume*, *97*(9), 715–720.

Thompson, B.F. (2020). *Effects on Initial Fixation of Cementless Tibial Trays in Total* Knee Arthroplasty (Master's thesis, University of Denver). Retrieved from: https://digitalcommons.du.edu/etd/1857

Tissakht, M., Eskandari, H., & Ahmed, A. (1995). Micromotion analysis of the fixation of total knee tibial component. *Computers & Structures*, *56*(2–3), 365–375.

Totoribe, K., Chosa, E., Yamako, G., Hamada, H., Ouchi, K., Yamashita, S., & Deng, G. (2018). Finite element analysis of the tibial bone graft in cementless total knee arthroplasty. *Journal of Orthopaedic Surgery and Research*, *13*(1).

Ulrich, D., Hildebrand, T., van Rietbergen, B., Müller, R., & Rüegsegger, P. (1997). The quality of trabecular bone evaluated with micro-computed tomography, FEA and mechanical testing. *Studies in Health Technology and Informatics*, *40*, 97–112.

Uvehammer, J. (2001). Knee joint kinematics, fixation and function related to joint area design in total knee arthroplasty. *Acta Orthopaedica Scandinavica*, *72*(2), 1–52.

Väänänen, S. P., Amin Yavari, S., Weinans, H., Zadpoor, A. A., Jurvelin, J. S., & Isaksson, H. (2013). Repeatability of digital image correlation for measurement of surface strains in composite long bones. *Journal of Biomechanics*, *46*(11), 1928–1932.

Varadarajan, K. M., Harry, R. E., Johnson, T., & Li, G. (2009). Can in vitro systems capture the characteristic differences between the flexion–extension kinematics of the healthy and TKA knee? *Medical Engineering & Physics*, *31*(8), 899–906.

Verdonschot, N., & Huiskes, R. (1996). Mechanical Effects of Stem Cement Interface Characteristics in Total Hip Replacement. *Clinical Orthopaedics & Related Research*, *329*, 326–336.

VIVO knee simulator. (n.d.). VIVO | AMTI. Retrieved October 1, 2021, from https://www.amti.biz/vivo.aspx?gclid=CjwKCAjw1JeJBhB9EiwAV612y9Yw70kMX697I3ZpevrsYOgRU1f9aj7U4qBve6J2uXsdFNB_yZ1-rRoCsmkQAvD_BwE

Waterson, H. B., Clement, N. D., Eyres, K. S., Mandalia, V. I., & Toms, A. D. (2016). The early outcome of kinematic versus mechanical alignment in total knee arthroplasty. *The Bone & Joint Journal*, *98-B*(10), 1360–1368.

Wernecke, G. C., Harris, I. A., Houang, M. T., Seeto, B. G., Chen, D. B., & MacDessi, S. J. (2012). Comparison of Tibial Bone Coverage of 6 Knee Prostheses: A Magnetic

Resonance Imaging Study with Controlled Rotation. *Journal of Orthopaedic Surgery*, *20*(2), 143–147.

White, P. B., Ranawat, C. S., & Ranawat, A. S. (2015). Fixed Bearings versus Rotating Platforms in Total Knee Arthroplasty. *Journal of Knee Surgery*, *28*(05), 358–362.

Whiteside, L. A. (2001). Long-Term Followup of the Bone-Ingrowth Ortholoc Knee System Without a Metal-Backed Patella. *Clinical Orthopaedics and Related Research*, *388*, 77–84.

Wikipedia contributors. (2021a, June 2). *Wolff's law*. Wikipedia. https://en.wikipedia.org/wiki/Wolff%27s_law#cite_note-1

Wikipedia contributors. (2021b, June 6). *Stress shielding*. Wikipedia. https://en.wikipedia.org/w/index.php?title=Stress_shielding&oldid=1027150199

Wikipedia contributors. (2021c, July 18). *Linear variable differential transformer*. Wikipedia. https://en.wikipedia.org/wiki/Linear_variable_differential_transformer

Willert, H. G., & Semlitsch, M. (1977). Reactions of the articular capsule to wear products of artificial joint prostheses. *Journal of Biomedical Materials Research*, *11*(2), 157–164.

Wilson, H. (2018). *Cementless Tibial Base Micromotion During Activities of Daily Living* (Master's thesis, University of Denver). Retrieved from: https://digitalcommons.du.edu/etd/1471

Wolff, J. (1893). Das Gesetz der Transformation der Knochen. *DMW - Deutsche Medizinische Wochenschrift*, *19*(47), 1222–1224.

Yang, H., Bayoglu, R., Clary, C. W., & Rullkoetter, P. J. (2021). Impact of surgical alignment, tray material, PCL condition, and patient anatomy on tibial strains after TKA. *Medical Engineering & Physics*, *88*, 69–77.

Yang, H., Bayoglu, R., Renani, M. S., Behnam, Y., Navacchia, A., Clary, C. W., & Rullkoetter, P. J. (2020). Validation and sensitivity of model-predicted proximal tibial displacement and tray micromotion in cementless total knee arthroplasty under physiological loading conditions. *Journal of the Mechanical Behavior of Biomedical Materials*, *109*, 103793.

Yang, P. F., Brüggemann, G. P., & Rittweger, J. (2011). What do we currently know from in vivo bone strain measurements in humans? *Journal of Musculoskeletal & Neuronal Interactions*, *11*(1), 8–20.

Yildirim, G., Gopalakrishnan, A., Davignon, R. A., Parker, J. W., Chawla, H., & Pearle, A. D. (2016). Comparative Fixation and Subsidence Profiles of Cementless

Unicompartmental Knee Arthroplasty Implants. *The Journal of Arthroplasty*, *31*(9), 2019–2024.

Yoon, C., Chang, M. J., Chang, C. B., Song, M. K., Shin, J. H., & Kang, S. B. (2018). Medial Tibial Periprosthetic Bone Resorption and Its Effect on Clinical Outcomes After Total Knee Arthroplasty: Cobalt-Chromium vs Titanium Implants. *The Journal of Arthroplasty*, *33*(9), 2835–2842.

Yoshii, I., Whiteside, L. A., Milliano, M. T., & White, S. E. (1992). The effect of central stem and stem length on micromovement of the tibial tray. *The Journal of Arthroplasty*, *7*, 433–438.

Zannoni, C., Mantovani, R., & Viceconti, M. (1999). Material properties assignment to finite element models of bone structures: a new method. *Medical Engineering & Physics*, *20*(10), 735–740.

Zhang, Q. H., Cossey, A., & Tong, J. (2016a). Stress shielding in bone of a bone-cement interface. *Medical Engineering & Physics*, *38*(4), 423–426.

Zhang, Q. H., Cossey, A., & Tong, J. (2016b). Stress shielding in periprosthetic bone following a total knee replacement: Effects of implant material, design and alignment. *Medical Engineering & Physics*, *38*(12), 1481–1488.

APPENDICES

Yang, H., Bayoglu, R., Renani, M. S., Behnam, Y., Navacchia, A., Clary, C. W., & Rullkoetter, P. J. (2020). Validation and sensitivity of model-predicted proximal tibial displacement and tray micromotion in cementless total knee arthroplasty under physiological loading conditions. *Journal of the Mechanical Behavior of Biomedical Materials*, *109*, 103793.

Yang, H., Bayoglu, R., Clary, C. W., & Rullkoetter, P. J. (2021). Impact of surgical alignment, tray material, PCL condition, and patient anatomy on tibial strains after TKA. *Medical Engineering & Physics*, *88*, 69–77.

Yang, H., Bayoglu, R., Clary, C. W., & Rullkoetter, P. J. Impact of patient, surgical, and implant design factors on predicted tray-bone interface micromotions in cementless total knee arthroplasty. *Journal of Orthopaedic Research.* (Submitted November 2021)

Yang, H., Bayoglu, R., Renani, M. S., Behnam, Y., Navacchia, A., Clary, C. W., & Rullkoetter, P. J. (2019). Validation of model-predicted proximal tibial displacement and tray micromotion in cementless TKA. *32nd Annual Congress of International Society for Technology in Arthroplasty*. Toronto, Canada. 2019. *Accepted for podium presentation.*

Yang, H., Bayoglu, R., Clary, C. W., & Rullkoetter, P. J. (2019). Impact of Surgical Alignment, tray material, PCL condition, and patient anatomy on proximal tibial strains after TKA. *32nd Annual Congress of International Society for Technology in Arthroplasty*. Toronto, Canada. 2019. *Accepted for podium presentation.*

Han, X., Yang, H., Navacchia, A., Rullkoetter, P. J., & Clary, C. W. (2019). Validation of model-predicted cementless patella displacements during lunge. *32nd Annual Congress of International Society for Technology in Arthroplasty*. Toronto, Canada. 2019. *Accepted for podium presentation.*

Yang, H., Bayoglu, R., Clary, C. W., & Rullkoetter, P. J. (2020). Impact of alignment variation and activity on tray-bone interface micromotions in cementless TKA. *66th Annual Meeting of the Orthopaedic Research Society*. Phoenix, AZ, 2020. *Accepted for podium presentation.*

COPYRIGHT PERMISSION

Figure 1.4 was reprinted with permission from "The Effects of Trabecular-Bone Loading Variables on the Surface Signaling Potential for Bone Remodeling and Adaptation" by Ruimerman et al., 2005, *Annals of Biomedical Engineering, 33*(1), 71–78. Copyright 2005 by Elsevier.

Figure 2.2a was reprinted with permission from "Biomechanical evaluation of proximal tibia behaviour with the use of femoral stems in revision TKA: An in vitro and finite element analysis" by Completo et al., 2010, *Clinical Biomechanics, 25*(2), 159–165. Copyright 2010 by Elsevier.

Figure 2.2b was reprinted with permission from "Proximal tibial strain in medial unicompartmental knee replacements" by Scott et al., 2013, *The Bone & Joint Journal, 95-B*(10), 1339–1347. Copyright 2013 by British Editorial Society of Bone & Joint Surgery.

Figure 2.2b was reprinted with permission from "The Effect of Rotating Platform TKA on Strain Distribution and Torque Transmission on the Proximal Tibia" by Malinzak et al., 2014, *The Journal of Arthroplasty, 29*(3), 541–547. Copyright 2014 by Elsevier.

Figure 2.2c was reprinted with permission from "A Comparison in Proximal Tibial Strain Between Metal-Backed and All-Polyethylene Anatomic Graduated Component Total Knee Arthroplasty Tibial Components" by Small et al., 2010, *The Journal of Arthroplasty, 25*(5), 820–825. Copyright 2010 by Elsevier.

Figure 2.2d was reprinted with permission from "Glenoid bone strain after anatomical total shoulder arthroplasty: In vitro measurements with micro-CT and digital volume correlation" by Boulanaache et al., 2020, *Medical Engineering & Physics, 85*, 48–54. Copyright 2020 by Elsevier.

Figure 2.3a was reprinted with permission from "Micromotion of Cementless Tibial Baseplates: Keels with Adjuvant Pegs Offer More Stability Than Pegs Alone" by Bhimji & Meneghini, 2014, *The Journal of Arthroplasty, 29*(7), 1503–1506. Copyright 2014 by Elsevier.